Coherent optical spectroscopy of InGaAs/GaAs quantum dots doped with a single Mn atom

Jovana Filipovic

To cite this version:

Jovana Filipovic. Coherent optical spectroscopy of InGaAs/GaAs quantum dots doped with a single Mn atom. Quantum Physics [quant-ph]. Université Paris-Saclay, 2023. English. NNT : 2023UPASP194 . tel-04763446

HAL Id: tel-04763446
https://theses.hal.science/tel-04763446v1

Submitted on 2 Nov 2024

Coherent optical spectroscopy of InGaAs/GaAs quantum dots doped with a single Mn atom

Spectroscopie optique cohérente de boîtes quantiques InGaAs/GaAs dopées avec un unique atome Mn

Thèse de doctorat de l'université Paris-Saclay

École doctorale n° 572, ondes et matière (EDOM)
Spécialité de doctorat: Physique
Graduate School : Physique
Référent : Faculté des sciences d'Orsay

Thèse préparée dans l'unité de recherche **Centre de Nanosciences et de Nanotechnologies (Université Paris-Saclay, CNRS)**,
sous la direction d'**Olivier KREBS**, directeur de recherche

Thèse soutenue à Paris-Saclay, le 21 décembre 2023, par

Jovana FILIPOVIC

Composition du jury

Membres du jury avec voix délibérative

Jean-Sébastien LAURET Professeur, ENS Paris-Saclay Laboratoire LuMIn	Président
Maria VLADIMIROVA Directrice de recherche, CNRS Université de Montpellier Laboratoire Charles Coulomb	Rapporteuse & Examinatrice
Lucien BESOMBES Directeur de recherche, CNRS Université Grenoble Alpes Institut Néel	Rapporteur & Examinateur
Shilpi GUPTA Maîtresse de conférences Indian Institute of Technology Kanpur	Examinatrice

THESE DE DOCTORAT

NNT : 2023UPASP194

université PARIS-SACLAY

ÉCOLE DOCTORALE
Ondes et matière
(EDOM)

Titre: Spectroscopie optique cohérente de boîtes quantiques InGaAs/GaAs dopées avec un unique atome Mn

Mots clés: boîte quantique, spin, interaction lumière-matière, photoluminescence

Résumé: Depuis plus d'une décennie, on sait faire croître des boîtes quantiques InGaAs/GaAs (BQs) dopées avec un seul atome magnétique tel que Mn. Cette avancée a permis d'étudier l'interaction d'échange sp-d à l'échelle microscopique. Dans le contexte des technologies quantiques, ces BQs dopées au Mn présentent une structure de niveaux et des règles de sélection optique d'un grand intérêt pour la mise en œuvre de protocoles quantiques basés sur l'intrication spin-photon. La réalisation d'une spectroscopie optique cohérente de ces QDs est la première étape vers leur application possible dans ce domaine.

Jusque-là, les BQs InGaAs dopées au Mn dans un état de charge bien défini n'avaient été étudiées que sous excitation non résonnante par micro-photoluminescence (µPL). Pour exciter ces BQs de manière résonante, nous avons d'abord mis au point un microscope confocal à champ sombre basé sur le rejet du laser résonant réfléchi dans une configuration à polarisation croisée. Bien que nous ayons obtenu une extinction proche de l'état de l'art, la réalisation d'une véritable expérience de fluorescence par résonance s'est avérée difficile. En raison de diffusion spectrale élevée dans notre échantillon, le signal PL s'est avéré bien trop faible par rapport bruit de grenaille du laser réfléchi. Pour contourner ce problème, nous avons mis en œuvre une expérience de diffusion Raman résonante basée sur des transitions spécifiques de type Λ, ce qui nous a permis d'enregistrer le signal PL à une longueur d'onde différente de celle du laser résonnant, tout en donnant accès à l'étude de la cohérence des états de spin excités.

Nous avons d'abord appliqué cette technique pour étudier le cas d'un dopant Mn passivé par un atome d'hydrogène H. Dans les matériaux III-V, le Mn agit comme un accepteur peu profond. La passivation à l'hydrogène vise à empêcher la formation de cet état accepteur en liant l'un des atomes d'As voisins du Mn à un atome d'H. La signature optique résultante observée dans le spectre PL standard a révélé des motifs complexes notamment en champ magnétique. Pour interpréter ces résultats, nous avons développé un modèle théorique traitant le dopant Mn compensé comme un système de spin 5/2 sous forte contrainte uni-axiale, donnant lieu à une structure de niveaux qui a pu être confirmée par nos mesures de spectroscopie résonante. Incidemment, l'accord de notre modèle avec les résultats expérimentaux a nécessité de considérer une interaction d'échange ferromagnétique trou-Mn, contrairement à l'échange anti-ferromagnétique typique dans les BQs II-VI et III-V.

Nous nous sommes ensuite concentrés sur la spectroscopie de cohérence de BQs InGaAs dopées avec un Mn non passivé, afin d'étudier la cohérence entre différents états de spin. Nous avons d'abord utilisé un seul laser accordable pour scanner de manière résonnante les transitions d'un système en V, tout en mesurant la fluorescence due à la diffusion Raman résonnante vers un état spectateur. Les doublets d'Autler-Townes ont été résolues avec succès à puissance laser élevée, malgré l'élargissement inhomogène considérable des transitions optiques, ce qui a permis de mesurer les dipôles optiques. Pour décrire ce système, nous avons utilisé un modèle théorique basé sur les équations de Bloch optiques, qui a montré un excellent accord avec les résultats expérimentaux. Il nous a également permis d'estimer le temps de relaxation du spin entre les états fondamentaux ferromagnétique et antiferromagnétique.

Par la suite, nous avons réalisé une expérience à deux lasers, l'un fixé sur l'une des transitions du système V tandis que l'autre balaie la transition restante. L'utilisation de deux lasers a permis de créer une cohérence entre les états de spin excités, ce qui détermine le contraste du doublet Autler-Townes mesuré par cette méthode. En modélisant ces résultats, nous avons pu démontrer que le temps de cohérence du spin des états excités est principalement déterminé par leur durée de vie radiative.

université PARIS-SACLAY
ÉCOLE DOCTORALE
Ondes et matière
(EDOM)

Title: Coherent optical spectroscopy of InGaAs/GaAs quantum dots doped with a single Mn atom

Key words: quantum dot, spin, light-matter interaction, photoluminescence

Abstract: For over a decade, it has been possible to grow InGaAs/GaAs quantum dots (QDs) doped with a single magnetic atom such as manganese (Mn). This advancement enabled the investigation, at the single spin level, of the sp-d exchange interaction between the 3d5 electrons of Mn and individual carriers (electrons or holes). Additionally, in the context of quantum technologies, these Mn-doped QDs present a structure of levels and optical selection rules of potential high interest to implement quantum protocols based on spin-photon entanglement. Performing optical coherent spectroscopy of such QDs is the first step towards their possible application in this field.

Before this work, Mn-doped InGaAs QDs in a well-defined charge state have been studied only under non-resonant excitation with micro-photoluminescence (µPL) setup. To resonantly excite these QDs, we first developed a dark-field confocal microscope setup based on the rejection of the reflected resonant laser in a cross-polarized configuration. Although we achieved near state-of-the-art extinction of the stray light from the laser, performing a true resonance fluorescence experiment proved challenging. Indeed, due to the absence of optical cavity in our sample and to the presence of spectral diffusion, the PL signal turned out to be still a few orders of magnitude lower than the reflected laser shot noise, requiring a too long acquisition time to be extracted. To circumvent this issue, we implemented a resonance Raman scattering experiment based on specific Λ-like transitions found in these QDs, enabling us to record PL signal at a different wavelength than the resonant laser, and still giving us access to the study of excited spin state coherence.

We actually first applied this technique to study the case of an H-passivated Mn dopant in a QD. In III-V materials, Mn acts as a shallow acceptor with a magnetic center and localized hole. Hydrogen passivation aimed to prevent the formation of this acceptor state by bonding of one of the neighboring As atoms of Mn to an H atom. The resulting optical signature observed in standard PL spectrum revealed intricate line patterns with unique magnetic field behavior. To interpret these results, we developed a theoretical model treating the compensated Mn dopant as a 5/2 spin system in a highly strained configuration, giving rise to a structure of levels that could be confirmed via our resonant optical excitation setup. Remarkably, achieving agreement with experimental results required considering a ferromagnetic h-Mn exchange interaction, in contrast to the typical antiferromagnetic p-d exchange in Mn-doped II-VI and III-V QDs.

We then focused on conducting coherence spectroscopy of non-passivated Mn-doped InGaAs QDs to study the coherence between different spin states. We first used a single scanning laser to resonantly excite one of the two transitions of a V-type system and measured the fluorescence due to resonant Raman scattering towards a spectator state. Autler-Townes splittings were successfully resolved under conditions of high laser power, despite the considerable inhomogeneous broadening of the optical transitions, providing a measurement of the optical dipoles. To describe this system, we used a theoretical model based on the optical Bloch equations, which demonstrated excellent agreement with the experimental results. It also enabled us to estimate the spin relaxation time between the ferromagnetic and antiferromagnetic ground states.

Subsequently, we conducted a two-laser experiment, with one laser fixed on one of the V-system transitions while the other scanned the remaining transition. The use of two lasers was instrumental in creating coherence between the excited spin states, which notably determined the contrast of the measured Autler-Townes doublet. By modelling these results, we could evidence that the spin coherence time of the excited states is mostly determined by their radiative lifetime.

We know little, but that we must trust in
what is difficult is a certainty that will never abandon us;
it is good to be solitary, for solitude is difficult;
that something is difficult must be one more reason for us to do it.

RAINER MARIA RILKE

Contents

Acknowledgements

I extend my deepest gratitude to my supervisor, Olivier Krebs, for his unwavering support throughout my PhD journey. His guidance not only shaped my research but also enriched my understanding of physics. I am truly grateful for his mentorship, availability, insightful discussions, and the invaluable feedback during both my experimental work and writing of this manuscript. All of this have enabled me to bring this research to a successful conclusion. I am honoured to have carried out my research under his supervision.

I would like to express my sincere appreciation to the members of the jury: Jean-Sébastien Lauret, Maria Vladimirova, Lucien Besombes and Shilpi Gupta for generously dedicating their time and providing constructive comments.

Special thanks go to Aristide Lemaître for his crucial role in creating the samples used in this thesis. His expertise in sample fabrication, done prior to this thesis, has been indispensable to the success of my research. I also appreciate his assistance with wire bonding, which further contributed to my experimental work. I am thankful for his valuable contribution.

I greatly appreciate the insightful discussions with Shilpi Gupta and Neelesh Kumar Vij about the theoretical models presented in the last part of this work. Their thoughtful insights and collaborative engagement added a layer of depth to the exploration of these models. I am genuinely grateful for their valuable contributions, which have enhanced the overall quality of this research endeavor.

I extend my appreciation to the entire research group GOSS, encompassing both permanent members and students, for fostering a collaborative and intellectually stimulating environment. The exchange of ideas and experiences within this group has been exceptionally enriching and has contributed significantly to the depth of my research.

I am grateful to the C2N lab, where I conducted my PhD research. The facilities, resources, and the collaborative spirit of the lab were instrumental in the successful completion of this work.

Particularly, I want to express my sincere thanks to my family for always being there with unconditional support. Their love and encouragement kept me going, and I appreciate their constant belief in me.

This research would not have been possible without the collective support, encouragement, and expertise of these individuals and institutions. I am sincerely thankful for their contributions to my academic and research journey.

Introduction

Over the last two decades, extensive research has been dedicated to exploring semiconductor quantum dots (QDs) doped with a single magnetic impurity, characterized by a localized electronic spin. One part of these studies has been focused on the investigation of the exchange interaction between the spin of a confined electron or hole in the few-spin regime, as evidenced by extensive research [1–9]. Beyond this fundamental exploration, there exists a growing interest in potential utilization of these systems as solid-state quantum bits for applications like spin-based quantum memory coupled to flying qubits [10–19], such as photons. The latter is particularly relevant with III-V QDs embedded in an optical cavity, representing advanced sources of indistinguishable single photons [20–22] and potential generators of multi-entangled photons in a cluster state.

While the Lindner-Rudolph (LR) protocol [23] for generating such light states has been successfully implemented with undoped InGaAs/GaAs QDs [24–26], scaling it towards highly entangled photonic cluster states faces challenges due to imperfections in the spin-photon interface [27]. A new exploration avenue emerges with InGaAs/GaAs QDs doped with a single Mn atom [13], showcasing optical selection rules which resemble to those observed in a protocol proposed for generating cluster states with a single hole spin in a QD molecule [28]. Both systems, under certain conditions, demonstrate Λ-like transitions for spin manipulation and cycling transitions for photon emission.

Pursuing this challenging objective, our present work takes a step forward by investigating continuous wave (cw) coherent spectroscopy. This approach is applied to a self-assembled InGaAs/GaAs QD doped with a single Mn atom, with the specific aim of assessing the coherence between different spin states associated with this magnetic dopant.

The manuscript is organized as follows:

- In **Chapter 1**, we introduce the fundamentals of InGaAs/GaAs quantum dots (QDs) - their growth, level discretization due to confinement and control of charge in the QD. Following that, we describe the spectral characteristics of InGaAs/GaAs QDs doped with a single Mn atom. These QDs exhibit a distinct spectrum in zero magnetic field, and their optical signature in a longitudinal magnetic field is presented as well. A theoretical model previously reported in [6] is outlined here as it will be utilized as a starting point in Chapter 3.

- In **Chapter 2**, we describe a dark-field confocal microscope setup that will be employed to resonantly excite these Mn-doped InGaAs QDs. We first present the principle of this setup based on the rejection of the reflected resonant laser in a cross-polarized configuration and the results of laser extinction reported in literature [29]. Following that, we detail the different steps in the process of building this setup, as well as its stability and performance. Finally, this setup is implemented for the resonant excitation of a single Mn-doped InGaAs QD in a sample with Schottky contacts.

- In **Chapter 3**, we applied previously developed setup to study H-passivated Mn dopant in InGaAs QD. This sample was studied in order to examine the large spectral diffusion observed previously in Schottky diode sample. In this case, we observe different spectral characteristics than for non-passivated Mn. To describe these QDs, we develop a theoretical model that treats the compensated Mn dopant as a 5/2 spin system in a highly strained configuration. The structure of levels predicted by the model is then confirmed by resonant optical excitation. Finally, this sample is annealed and optical characteristics of non-passivated Mn-doped QDs are restored.

- In **Chapter 4**, we perform coherence spectroscopy of non-passivated Mn-doped InGaAs QDs to study the coherence between different spin states. We first introduce the concept of dressed states and Autler-Townes effect observed as a result of that. We then use a single scanning laser to excite one of the transitions of a V-type system resonantly and we measure the fluorescence as a result of transition towards a spectator state. A theoretical model based on optical Bloch equations is developed to describe the experimental results. The Autler-Townes effect is resolved at high laser powers, and the dependence of AT splitting on laser power is examined. In the second part of this chapter, a two-laser experiment is conducted, where one laser is fixed on one of the V-type system transitions, while the other laser scans the other transition. The use of two lasers results in coherence between the excited spin states. The observed Autler-Townes effect and electromagnetically induced transparency-like effect are described.

Chapter 1

Fundamentals of Mn-doped InGaAs/GaAs quantum dots

1.1 InGaAs/GaAs quantum dots

1.1.1 Growth of self-assembled quantum dots

A semiconductor quantum dot (QD) is a nanostructure of lower bandgap material embedded in a higher bandgap material. InGaAs/GaAs QDs studied in this thesis are fabricated using the Stranski-Krastanov method [30, 31]. InAs is grown on a GaAs substrate by molecular beam epitaxy (MBE). MBE is commonly used to grow semiconductor structures with atomic monolayer precision. These two materials have slightly different lattice constants ($a_{InAs} = 6.06$ Å and $a_{GaAs} = 5.65$ Å). Because of this lattice mismatch, epitaxial growth of InAs happens in two stages. First, a monolayer of InAs undergoes two-dimensional (2D) growth adapting to the lattice of GaAs, leading to an accumulation of strain in the InAs layer. Then, after the specific critical thickness, about 1.7 monolayers, growth becomes three-dimensional (3D) which enables the relaxation of strain. This results in the formation of islands on the initial monolayer of InAs, called the wetting layer. These islands are randomly distributed over the wetting layer (Fig. 1.1a). Their surface density depends on the growth conditions (substrate temperature, deposition rate) and typically varies from $\sim 10^7$ to $\sim 10^{12}$ cm^{-2}.

These islands become QDs, notably with good optical properties, once fully embedded in the higher gap material, namely by the epitaxial deposition of the capping layer of GaAs. The typical shape of such QDs resembles a lens, with a lateral dimension of about 20-30 nm and a height of 3-5 nm (Fig. 1.1b). After the deposition of this GaAs layer, the composition of QDs is modified. Due to the interdiffusion of Ga, the actual composition of QD is not uniform and amounts to an alloy $\text{In}_{1-x}\text{Ga}_x\text{As}$ with x of the order of 0.3 [32]. For this reason, in the rest of this manuscript we denote them as InGaAs QDs.

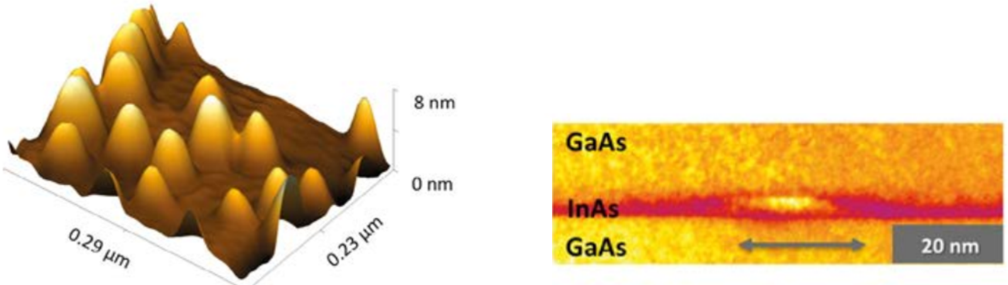

(a) (b)

Figure 1.1: (a) Atomic-force microscope image of the surface of the InAs layer. (b) Transmission electron microscope image of a single quantum dot. *Images are taken from Ref. [33]*

1.1.2 Level discretization due to confinement

Since InAs is a lower bandgap material than GaAs, this creates a three-dimensional confinement for carriers. This results in discrete energy levels which can be occupied by electrons and/or holes respecting the Pauli exclusion principle as it is the case in atoms. Due to this remarkable similarity, QDs are often called *artificial atoms* [34].

Over the years, comprehensive models were developed to describe carriers' energy levels, taking into account the realistic shape of QDs and strain [35–38]. In this thesis, we present a very simplified model to give a general description of the quantized levels in QD. For an electron or hole trapped in a three-dimensional rectangular quantum well with infinite barriers and using the effective mass approximation [39], solving the stationary Schrödinger equation provides the following energy quantization:

$$E_{e,h} = \frac{\hbar^2}{2m^*_{e,h}} \left(\frac{n_x^2 \pi^2}{L_x^2} + \frac{n_y^2 \pi^2}{L_y^2} + \frac{n_z^2 \pi^2}{L_z^2} \right) + E_{gap} \tag{1.1}$$

where L_x, L_y, L_z are the QD dimension and $m^*_{e,h}$ the effective mass of an electron (e) or hole (h). This formula can be used to estimate the energy gap for carriers between the lowest energy state ($n_x = n_y = n_z = 1$) and the first excited state ($(n_x, n_y) = (1,2)$ or $(2,1)$ and $n_z = 1$). If we consider now the x-direction ($L_x = 20$ nm) and if we take the values for the effective transverse mass of an electron and heavy hole as in Ref. [40], $m^*_e = 0.067 m_0$ and $m^*_{hh} = -0.11 m_0$ respectively, we obtain the energy gaps between two first states for electrons and heavy holes:

$$\Delta E_{s,p} = \frac{3\pi^2\hbar^2}{2m^*_e L_x^2} \approx 42\,\mathrm{meV} \tag{1.2}$$

$$\Delta E_{s,p} = \frac{3\pi^2\hbar^2}{2m^*_{hh} L_x^2} \approx -25\,\mathrm{meV} \tag{1.3}$$

Even though this is a very simplified model, it still gives the correct order of magnitude for the separation of energy levels of electrons and holes in a QD. If we now do a similar calculation as in Eq. 1.2 for z-direction ($L_z = 4$ nm), the energy gap is $E_z \approx 350$ meV. Thus, due to the shape of QDs, only one electronic state is confined in the growth direction, and at least two electronic states are present in the x and y directions. The growth direction is, therefore, the main axis of quantization.

Since the dimensions of self-assembled InGaAs QDs vary significantly in an ensemble, as seen in Fig. 1.1a, the confinement energies of the QD ground state is inhomogeneously broadened. Indeed, a fluctuation of the height of the order of ±1 monolayer (±2.8Å) leads to a typical fluctuation of energy $\approx \pm 50$ meV (for an electron and $L_z = 4$ nm). This shows that even a highly optimized growth process is likely to result in a substantial energy fluctuation, leading to the inhomogeneous distribution of QD optical transition energies. This is one of the major differences with respect to real atoms.

Depending on the energy of optical excitation, carriers can be created in bulk GaAs, in WL InAs (non-resonant excitation) or directly in the QD (resonant or phonon assisted excitation). When the carriers are generated with non-resonant excitation, they first relax non-radiatively towards the electron or hole ground states, in a typical time range of 30-50 ps [41, 42]. The electron-hole pair created in an epitaxial InGaAs QD (with no defects such as pending bonds) then undergoes radiative recombination via spontaneous emission of a single photon within a typical lifetime of ~ 1 ns. This gives rise to a photoluminescence signal of prominent importance for many research works or applications.

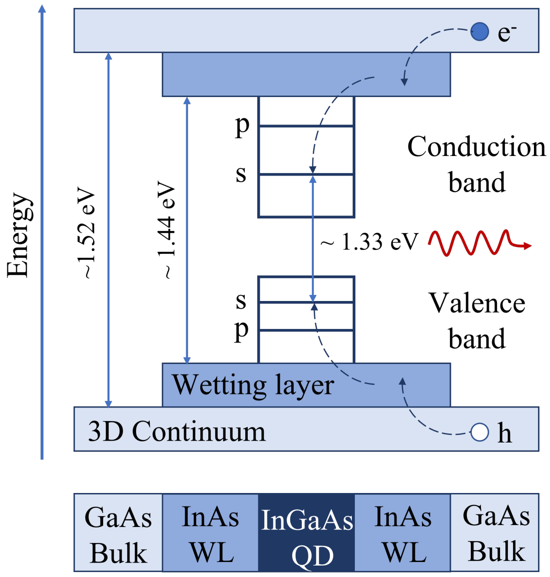

Figure 1.2: Schematic of QD structure. Discrete energy levels for holes and electrons are indicated (s and p shells). The process of creation of charges in QD with non-resonant excitation is also indicated. Optically pumped carriers in the environment of QD can relax into the dot and fill the corresponding energy levels.

1.1.3 QD excitons, biexcitons and trions

When a QD is excited by a non-resonant laser of moderate intensity at the wetting layer energy, the QD emission usually can come from four different electronic state occupations due to the relaxation process explained in the previous section. These four states have different emission energies (as seen in Fig. 1.3b) since the effect of Coulomb interaction depends on the combination of trapped charges [43, 44].

The first possible state is when an electron-hole pair is present in the QD. This state is called *exciton* (denoted X). While in the systems with less confinement, an electron-hole pair is bound by Coulomb interaction, it should be noted that in the case of QD, the predominant effect for the formation of an exciton is the quantization of the kinetic energy due to the strong confinement [45]. Upon the recombination of this electron-hole pair, a photon is emitted at the wavelength λ_X. If two electron-hole pairs are present simultaneously in the QD, this state is called *biexciton* (XX). The recombination process of biexciton consists of two steps (as shown in Fig. 1.3a). Firstly, one electron-hole pair recombines, and the emitted photon has the wavelength λ_{XX}, which is different from the wavelength of the exciton. This difference in wavelength comes from the difference in Coulomb interaction when two electron-hole pairs are trapped in the QD [45]. After the recombination of the first electron-hole pair, the recombination of excitonic state and emission of the photon at λ_X occurs. The other possible occupancy states happen when an additional charge is present in the QD together with an electron-hole pair. These states are called *charged exciton* (CX) or *trion* [46]. If an electron is already present in the conduction band and the QD is then non-resonantly excited, the created state is called *negative trion*, and its emission wavelength is typically 5 nm above λ_X. The other possibility is to have a hole in the valence band. Then the excited state is called a *positive trion*, and it emits a photon at the wavelength is at typically ±2nm from λ_X, depending on the QD size. The typical photoluminescence (PL) spectrum of a QD is shown in Fig. 1.3b. Different techniques should be used in order to identify these lines. Exciton and biexciton lines can be distinguished by their different properties during a saturation measurement. With the non-resonant laser power increase, the biexciton line follows a quadratic dependence [47, 48], while the exciton shows a linear dependence. The charged excitons can be distinguished from the neutral by the lack of polarized fine structure splitting and by their specific Zeeman splitting in a magnetic field perpendicular to the optical/growth axis (Voigt configuration) [49].

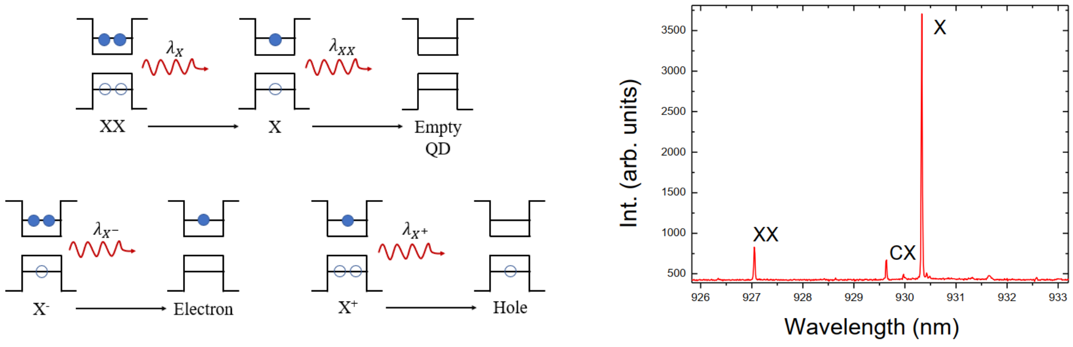

(a) (b)

Figure 1.3: (a) Schematic of electronic occupancy states of a QD. (b) Photoluminescence spectrum of an InAs QD in a planar cavity under non-resonant excitation. *Image taken from Ref. [50]*

1.1.4 Control of charge in the quantum dots

In order to control the charge in a quantum dot, it is possible to use a Schottky diode structure. This type of structure is presented in Fig. 1.4a. Here, it consists of a 200 nm thick strongly n-doped GaAs contact layer followed by a non-intentionally doped (nid) 25 nm GaAs layer, then the QD layer. The latter is capped with 30 nm nid GaAs, 100 nm thick nid $Ga_{0.7}Al_{0.3}As$ blocking barrier and finally 20 nm thick nid GaAs cap. After that, a back ohmic contact is established on the n-doped GaAs layer by interdiffusing a Ni/Au/Ge alloy and a thin layer of NiCr (5 nm, to remain semitransparent for optical studies) is evaporated on the top of the sample to form the Schottky contact.

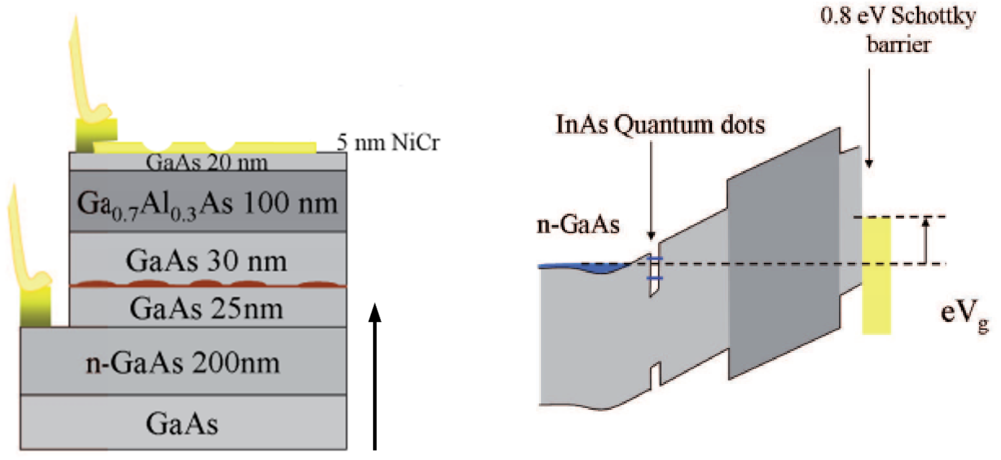

(a) (b)

Figure 1.4: (a) Sample after all the fabrication steps. The arrow indicates the growth direction (bottom-up). (b) A band structure of n-i-Schottky diode that allows the control of charge in the quantum dot. *Images are taken from Ref. [51]*

By applying the voltage between the top and back contact, it is possible to adjust the QD chemical potential so that the electrons can tunnel from n contact into the QD (Fig. 1.4b) [52, 53]. Thus, we can control the number of electrons in the QD with this kind of structure. The formation of positive trions X^+ is possible thanks to a quasi-resonant optical excitation which enables the creation of an electron-hole pair in the QD. The photo-created electron tunnels out of the QD while the hole stays trapped long enough to form X^+ with a second electron-hole pair [54]. It has been shown in previous study of such samples [51] that, compared to the n-i-Schottky diodes, the p-i-Schottky diodes are not as good in controlling the charge in QD. Thus, the possibility to trap a hole in QD by optical excitation is preferentially used to study hole spin in ground state or electron spin in X^- state.

Figure 1.5 shows an example of charge control for a single QD. By changing the gate voltage, the spectral lines of different states (neutral excitons and trions) are observed and they are slightly tilted due to the electrical Stark effect. Identifying these lines and corresponding QD charge state ($n_e = -1 \rightarrow n_e = 2$) relies on several observations. First, a single spectral line is observed for the gate voltage (V_g) between

0 and ~ 0.15 V. This line corresponds to the neutral exciton state X^0, which is proven by its fine structure observed in the linear polarisation [55]. For $V_g > 0.15$ eV, a red-shifted negative trion X^- appears, indicating the charging of the QD with one electron. At this point, the lines of X^0 and X^- exist simultaneously because under the quasi-resonant optical excitation (at 1.31 eV), a photocreated hole can be captured, resulting in optical recombination with the resident electron. For $V_g > 0.35$ eV, the X^0 line disappears, which means the number of stable electrons in the QD is $n_e = 2$. Note that a X^{2-} would be possible only at higher voltage enabling stabilization of an electron in the QD p-level. For negative V_g, the X^0 line disappears due to the electron tunnelling out of the QD and a blue-shifted X^+ line appears.

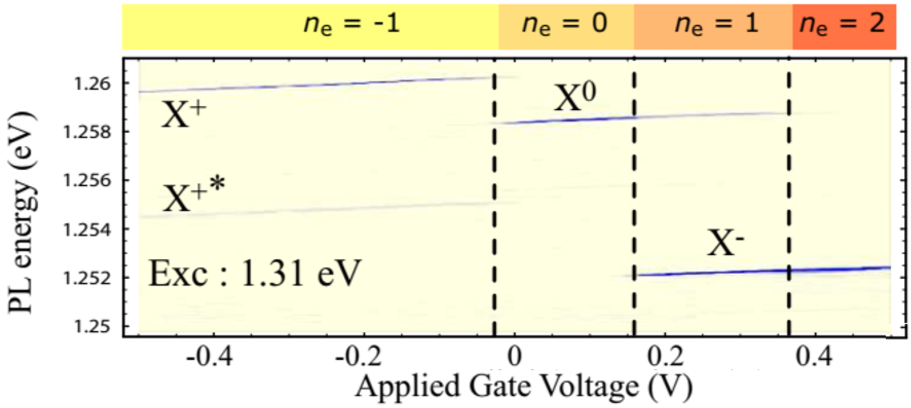

Figure 1.5: Color-scale µPL spectra for a single InGaAs QD as a function of the detection energy and applied gate voltage for an optical excitation at 1.31 eV. *Image is taken from Ref. [56]*

1.1.5 Spin-orbit interaction, heavy and light hole sub-bands

In order to get a better understanding of the levels that electrons and holes fill in a quantum dot, we should first introduce the general band structure of III-V materials used for the fabrication of these QDs. Both GaAs and InAs belong to a group of semiconductor compounds with a zinc-blende structure. As illustrated in Fig. 1.6a, the electronic bands of these materials are parabolic close to the extrema, which are located at the Γ point ($k = 0$) [57]. The absence of an inversion symmetry affects the degeneracy of these bands [58, 59]. However, the spin splitting induced due to this asymmetry is much smaller than the energy splitting due to the confinement in quantum dot, and it will be neglected in the description.

For understanding the structure of bands, it is essential to introduce the spin-orbit interaction. This is a relativistic effect of an electron that moves in an external electric field and experiences an effective magnetic field that couples to its spin. When this spin-orbit interaction is taken into account, it gives rise to valence band splitting (see Fig. 1.6b). The valence thus consists of electronic states with total angular momentum $j = 3/2$ and $j = 1/2$. These valence band states are split by the spin-orbit interaction energy Δ_{so}. This splitting is $\Delta_{so} = 340$ meV for GaAs and $\Delta_{so} = 380$ meV for

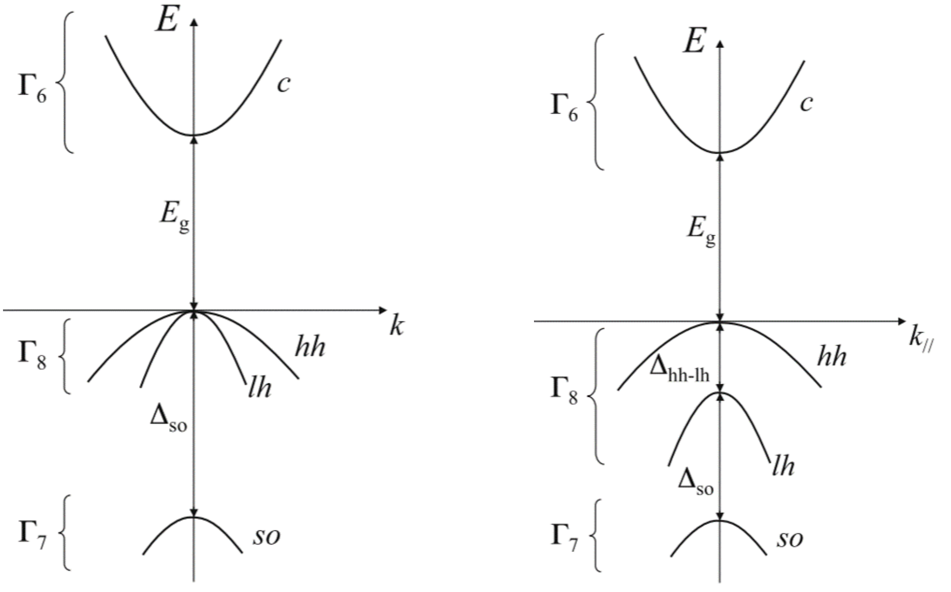

(a) (b)

Figure 1.6: Scheme of the electronic band structure of crystals with zinc-blende structure near the Γ point (a) without strain and (b) with uniaxial strain as it is the case in confined quantum dot states. Here (c) denotes the conduction band, (hh) the heavy-hole band, (lh) the light-hole band and (so) the split-off band. Eg is the bandgap energy, Δ_{so} is the spin-orbit splitting and Δ_{hh-lh} is the splitting between the (hh) and the (lh) bands. *Images are taken from Ref. [57]*

InAs [60]. The states with $j = 1/2$ are referred to as the spin-orbit split-off (so) sub-band with the corresponding spinor representation Γ_7, while the states with $j = 3/2$ have representation Γ_8, and consist of two sub-bands called the heavy-hole (hh) and the light-hole (lh) sub-band. At the Γ point, the hh and lh sub-bands are degenerate, and for finite wave vectors k, they split into two branches. The angular momentum projections at $k = 0$ for hh and lh sub-bands are $J_z = \pm 3\hbar/2$ and $J_z = \pm\hbar/2$, respectively. The difference in curvatures of these branches induces their different effective masses. This is the reason why they are called heavy and light holes. In addition, in the presence of strain (notably in self-assembled QDs), the degeneracy of the valance band is further lifted [61]. This results in a large splitting Δ_{hh-lh} between the hh and lh bands at $k = 0$, which adds to the splitting due to different effective mass in QDs.

The valence band eigenstates at Γ point are formed by combining three electronic states $|X\rangle$, $|Y\rangle$, $|Z\rangle$ and spin states $|\Uparrow\rangle$ and $|\Downarrow\rangle$ (Table 1.1). These eigenstates are such that the total angular momentum $\hat{J} = \hat{L} + \hat{S}$ and its projection along z-axis J_z are diagonal in this new basis [60, 62].

1.1.6 Bright and dark excitons

As explained in the previous section, due to the strain and shape in self-assembled InGaAs QDs, the (hh and lh sub-bands are split in energy by several tens of meV,

Band	$\vert J, J_z\rangle$	**Expression**
Γ_8^{hh}	$\left\vert\frac{3}{2},\frac{3}{2}\right\rangle$	$-\frac{X+\mathrm{iY}}{\sqrt{2}}\Uparrow$
	$\left\vert\frac{3}{2},-\frac{3}{2}\right\rangle$	$-\frac{X-\mathrm{iY}}{\sqrt{2}}\Downarrow$
Γ_8^{lh}	$\left\vert\frac{3}{2},\frac{1}{2}\right\rangle$	$\sqrt{\frac{2}{3}}Z\Uparrow-\frac{X+\mathrm{iY}}{\sqrt{6}}\Downarrow$
	$\left\vert\frac{3}{2},-\frac{1}{2}\right\rangle$	$\sqrt{\frac{2}{3}}Z\Downarrow+\frac{X-\mathrm{iY}}{\sqrt{6}}\Uparrow$
Γ_7	$\left\vert\frac{1}{2},\frac{1}{2}\right\rangle$	$\frac{1}{\sqrt{3}}[Z\Uparrow+(X+\mathrm{iY})\Downarrow]$
	$\left\vert\frac{1}{2},-\frac{1}{2}\right\rangle$	$\frac{1}{\sqrt{3}}[-Z\Downarrow+(X-\mathrm{iY})\Uparrow]$

Table 1.1: Eigenstates of the valence sub-bands

which enables us to neglect *lh* states. The ground state exciton is then made of a heavy hole and an electron. For the heavy hole, the spin can be written as $|\Uparrow\rangle$ or $|\Downarrow\rangle$ and its angular momentum projection along the growth direction (z axis) is $J_{h,z}=\pm 3/2$. Similarly, the electron spin can be written as $|\uparrow\rangle$ or $|\downarrow\rangle$ and its angular momentum projection is $S_{e,z}=\pm 1/2$. This gives rise to four possible exciton spin states with the total exciton spin $M=J_{h,z}+S_{e,z}$ that is defined as follows:

$$\begin{aligned}
|+1\rangle &\equiv |\Uparrow,\downarrow\rangle = \left|+\frac{3}{2},-\frac{1}{2}\right\rangle\\
|-1\rangle &\equiv |\Downarrow,\uparrow\rangle = \left|-\frac{3}{2},+\frac{1}{2}\right\rangle\\
|+2\rangle &\equiv |\Uparrow,\uparrow\rangle = \left|+\frac{3}{2},+\frac{1}{2}\right\rangle\\
|-2\rangle &\equiv |\Downarrow,\downarrow\rangle = \left|-\frac{3}{2},-\frac{1}{2}\right\rangle
\end{aligned}\tag{1.4}$$

According to the optical selection rules, only the states with $|M|=1$ can couple to the light field and are hence optically active (*bright* excitons), while the states with $|M|=2$ are optically inactive (*dark* excitons). In the exciton state basis ($|+1\rangle$,$|-1\rangle$,$|+2\rangle$,$|-2\rangle$) there is in addition a non-zero electron-hole exchange interaction which can be described by the following effective Hamiltonian $H_{exchange}$:

$$H_{exchange}=\frac{1}{2}\begin{pmatrix}+\delta_0 & \delta_1 & 0 & 0\\ \delta_1 & +\delta_0 & 0 & 0\\ 0 & 0 & -\delta_0 & \delta_2\\ 0 & 0 & \delta_2 & -\delta_0\end{pmatrix}\tag{1.5}$$

This matrix has a block diagonal form. Thus, the bright and dark excitons do not mix and they are split by the energy $\delta_0\sim 0.3$ meV which is given by diagonal terms of the matrix. The off-diagonal matrix elements define the hybridization within the exciton states $|M|=1$ and $|M|=2$. Independent of the QD symmetry, the states with $|M|=2$ are always hybridized and split by the energy δ_2 which yet remains very small, only a few µeV. The off-diagonal terms δ_1 is non-zero when the QD has no rotational symmetry around the z axis, which is most often the case with values of typically 20 µeV in as-grown InGaAs QDs. This gives rise to the splitting δ_1 of the bright excitons, the so-called fine structure splitting, with new eigenstates $(|+1\rangle \pm |-1\rangle)/\sqrt{2}$ which are now linearly polarized along two orthogonal axes.

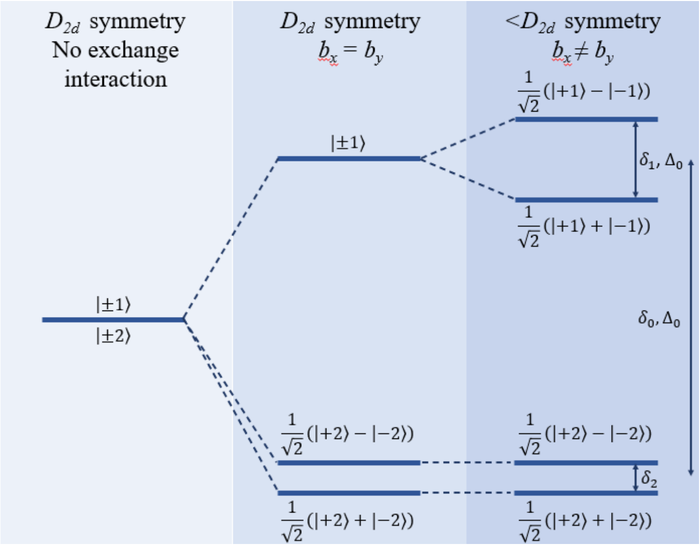

Figure 1.7: Schematic of the evolution of the exciton fine structure. The left column shows the exciton manifold when the exchange interaction is neglected. The central and right columns consider the exchange interaction for QDs with D_2d and with reduced symmetry, respectively.

1.2 InGaAs/GaAs quantum dots doped with a single Mn atom

Semiconductor structures, like the ones discussed in previous sections, utilize the charge of electrons or holes to process the information. In addition to semiconductors, many electronic and optical devices use magnetic materials. These materials use the spin of magnetic ions for information processing. For a long time, combining both properties in the same material has been sought for potential spintronic applications. This was done by incorporating magnetic atoms into a semiconductor crystal and thus creating diluted magnetic semiconductors (DMSs). Some examples of DMSs that have been extensively studied are II-VI and III-V-based semiconductors doped with low concentrations of Mn impurity [63–65]. In such materials, the strong $sp-d$ exchange interaction between the charge carriers (electron and hole) and $3d^5$ electrons associated with the Mn impurity results in a giant Zeeman effect, a large Faraday rotation and the formation of magnetic polarons. These effects are even more pronounced in the case of QDs and Mn impurity due to the confinement [66]. A single magnetic spin, embedded in a QD, also gives an attractive possible alternative to the electron spin for defining a quantum bit. Another interest for studying these QDs is the possibility to probe the exchange interaction between an electron (hole) and a single Mn atom. For such applications, it is necessary to be able to probe and manipulate this system with high sensitivity. One of the techniques employed in previous studies to address a single or few coupled spins is confocal optical microscopy [67]. By correlating the spectral characteristics with the spatial position on the sample, it is possible to scan a large number of QDs and find the ones doped with a single Mn atom. In this work, we will use a confocal dark field microscopy setup, which we implemented for carrying out resonance fluorescence (see Chapter 2) in order to infer new insights on the coherence properties of the spin states in Mn-doped InGaAs QDs. In the present section, we first present the main properties of this type of magnetic QDs as they were previously established at the beginning of this thesis.

1.2.1 Optical signature of a magnetic impurity in zero magnetic field

The properties of self-assembled quantum dot doped with a single Mn atom have been first investigated by the team of L. Besombes for the system of CdTe/ZnTe QDs [1–3, 68]. The Mn impurity in this system is an isoelectric center in a $3d^5$ configuration with spin $S = 5/2$. The large exchange interaction is present between the spin of carriers photo-created or trapped in the QD and the Mn magnetic moment. This notably results in the zero-field splitting of the exciton line into six bright components ($2S + 1 = 6$), which provides direct evidence of the exciton-Mn spin coupling.

In the case of GaAs and InAs materials, the situation is different because Mn, a transition metal, is missing one valence electron as compared to elements of column III (Ga or In) to form bonds with four surrounding atoms. For this reason, the substitutional Mn impurity captures an additional electron from the valence band to form tetrahedral bonds with its As neighbors, and thus acquires an excess negative charge. Therefore it manifests as an acceptor center, which can be found either in a state A^0 or A^- [69–72]. In low doped GaAs (density below 10^{19} cm^{-2}), the neutral acceptor state A^0 is dominant and consists of a negatively charged center A^- along with a bound hole h ($3d^5 + h$). This hole state is rather shallow with a typical 1 nm Bohr radius. The established binding energy is 112.4 meV for GaAs and would be 28 meV for InAs [71], but this value is not very well documented. The spectral signature of this neutral acceptor in InGaAs QDs is quite specific as was first reported by A. Kudelski et al. [5].

The sample of InGaAs QDs used in Ref. [5] was grown by MBE, see section 1.1.1. The temperature of the substrate was set to 500°C during the growth of the structure, which is a trade-off between optical quality of the dots and limitation of Mn segregation. The Mn cell shutter was opened in order to perform the doping at the very moment of InAs deposition. However, due to the remaining segregation of Mn atoms at such growth temperatures, it is difficult to determine precisely the Mn atom density really achieved in the QD layers. From Hall effect measurements in thick and uniformly Mn-doped GaAs layers grown at this temperature, the density would be approximatively $1 - 2 \cdot 10^{11}$ Mn atoms per cm^2, which gives a probability of $1/3 - 2/3$ Mn per dot. However, for the actual samples studied in µPL measurements, only rare QDs turn out to be doped with a single Mn atom ($< 0.1\%$). For samples grown at higher Mn cell temperature, the probability of finding Mn-doped QDs can however be much higher ($\sim 1\%$) [5]. The Mn-doped QD layer can also be embedded in between an electron reservoir and a Schottky gate (section 1.1.4), which allows us to study different charge states of a QD.

The µPL spectroscopy of a single QD doped with a single Mn atom shows a very specific signature. As shown in Fig. 1.8, a characteristic spectrum consists of two doublets separated by the energy Δ of a few 100 µeV. A weaker central line O is often observed between these two doublets. Noticeably, the splitting δ, of the order of a few tens of µeV, is exactly the same for both doublets. Contrary to the case of II-VI QDs [3], the characteristic spectrum is also practically the same for different occupancy states (X^0, X^-, X^+). Moreover, the relative energy position of X^- and $2X^0$ with respect to X^0 is the same as in the case of non-magnetic QDs [55]. This means that Mn doping is eventually a small perturbation to the electronic states of a QD.

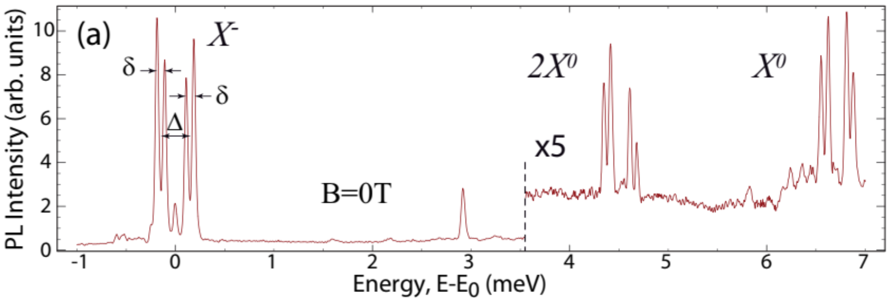

Figure 1.8: µPL spectrum of an individual InGaAs quantum dot doped with a single Mn atom in zero magnetic field at $T = 2$ K. The spectrum shows three different states (X^0, $2X^0$ and X^-) depending on the charge/occupancy of a QD. A common feature for the spectrum of these states is the present of two dominant symmetrical doublets. *Spectrum is taken from Ref. [56]*

These spectral characteristics can be interpreted by assuming that the Mn impurity in the QD has the A^0 configuration, along with an antiferromagnetic (AFM) $p-d$ exchange interaction between Mn spin $S = 5/2$ and the bound hole spin $J_h = 3/2$ (Fig. 1.9a). The strong AFM exchange interaction takes the form of a Heisenberg Hamiltonian $\varepsilon\hat{\boldsymbol{S}}\cdot\hat{\boldsymbol{J}}_h$m, where $\varepsilon \approx 5$ meV [70]. This creates a splitting of A^0 eigenstates as a function of the total angular momentum J. As a consequence, the triplet ground state $J = 1$ ($J_z = 0, \pm1$) is well separated from higher levels $J = 2, 3, 4$ by at least $2\varepsilon \sim 10$ meV. Thus, at low temperature ($k_\mathrm{B}T \ll 2\varepsilon$), these higher levels are not occupied and the A^0 acceptor exists only in its ground state $J = 1$. However, the A^0 ground state is not perfectly degenerate because the hole component of A^0 is sensitive to local variations of strain and composition in the vicinity of the impurity Mn center [69, 73]. This effect is illustrated in Fig. 1.9b. The lens shape of self-assembled QDs introduces a perturbation to the bulk potential, notably along the growth direction z. This shifts the level $|J_z = 0\rangle$ by an energy Δ_0 above the levels $|J_z = \pm1\rangle$. In addition, since the Mn atom is most often not positioned in the center of the QD, this introduces an in-plane anisotropy that couples the states $|J_z = \pm1\rangle$ resulting in a splitting by an energy δ of the mixed states. We can now consider the presence of an electron-hole pair (neutral exciton X^0) in the QD. We focus only on the exciton bright states $J_z^{exc} = \pm1$. The initial states $A^0 - X^0$ of the excitonic transition can be described in the basis $|\Uparrow\downarrow \text{ or } \Downarrow\uparrow, J_z\rangle$. The exchange interaction of Ising type between A^0 and X^0 (because of the heavy-hole character of the exciton hole) partially restores cylindrical symmetry around the z-axis, resulting in two levels separated by energy Δ (where $\Delta \gg \delta$). These two levels are labeled as $|\Uparrow\downarrow \text{ or } \Downarrow\uparrow, \pm 1\rangle$ and $|\Uparrow\downarrow \text{ or } \Downarrow\uparrow, \mp 1\rangle$, and correspond to a ferromagnetic (FM) and antiferromagnetic (AFM) spin configuration, respectively. Above these two levels, a third level $|\Uparrow\downarrow \text{ or } \Downarrow\uparrow, 0\rangle$ corresponding to an orthogonal (O) spin configuration is present (Fig. 1.9b). Thus, the optical recombination of excitons from FM and AFM states is possible toward the two A^0 ground states $(|+1\rangle \pm |-1\rangle)/\sqrt{2}$. This results in two doublets observed in zero magnetic field (Fig. 1.8). The central peak, positioned between these two doublets, corresponds to the transition from level O ($J_z = 0$), still with a lower intensity due to the thermal relaxation to the $J_z = \pm 1$ levels.

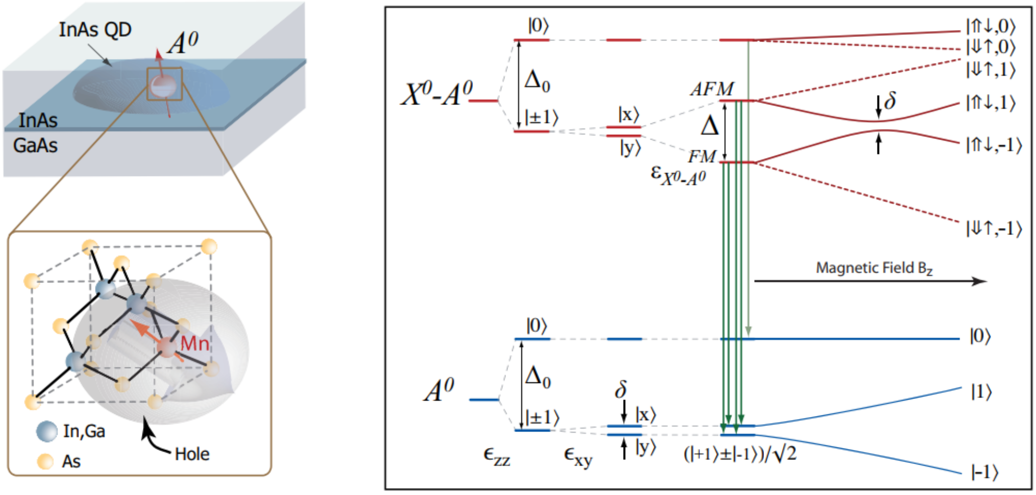

(a) (b)

Figure 1.9: (a) Schematics of an InGaAs QD doped with a single Mn atom. This impurity takes the form of neutral acceptor A^0 consisting of a negative A^- center and a bound hole h. b) Diagram of energy levels involved in the transitions from $X^0 - A^0$ to A^0 while considering the local potential anisotropy and the Zeeman effect due to a longitudinal magnetic field. Solid (dashed) lines correspond to the $|\Uparrow\downarrow\rangle$ ($|\Downarrow\uparrow\rangle$) exciton levels of σ^+ (σ^-) polarization. *Images are taken from Ref. [56]*

1.2.2 Optical signature of a magnetic impurity in longitudinal magnetic field

These InGaAs QDs with a single Mn atom can be described in more detail by studying their properties in a longitudinal magnetic field. As seen in Fig. 1.9b, the Zeeman effect splits the σ^+ (σ^-) polarized transitions. This gives rise to a very specific spectral signature, as shown in Fig. 1.10, for the three excitonic states of the QD in Fig. 1.8. These “magneto-PL” images consist of a series of µPL spectra recorded over a 6 meV energy range by varying the magnetic field from -3 T to 3 T with a step of 50 mT, with a detection in σ^+ polarization. The µPL intensity is plotted with a color scale against magnetic field and energy detection, using an interpolating function for a better graphical rendering.

With the increase of the magnetic field, the levels of $X^0 - A^0$ $|\Uparrow\downarrow, +1\rangle$ and $|\Uparrow\downarrow, -1\rangle$ are approaching each other (Fig. 1.9b). They are brought into coincidence at the magnetic field $B_z = \Delta/2g_{A^0}\mu_B$, where g_{A^0} is the effective g-factor of A^0 spin ($g_{A^0} \sim 2.8$ in bulk) [69] and μ_B is the Bohr magneton. Since these states are formed with the same exciton spin ($|\Uparrow\downarrow\rangle$), the anisotropic coupling between $|+1\rangle$ and $|-1\rangle$ is again present, resulting in the same splitting δ as in the zero-field for A^0. This effect can be seen in Fig. 1.10. The zero-field doublets evolve in the magnetic field to another pair of doublets at $B_z \approx 0.75$ T for this QD. Between these two anticrossings, a peculiar X pattern is observed. The origin of these crossing lines is the normally forbidden transitions $|\Uparrow\downarrow, \pm1\rangle \leftrightarrow |\mp 1\rangle$ involving A^0 spin flip, which become partially allowed due to the anisotropic coupling in the final (at $B_z = 0$) or initial (at $B_z \approx 0.75$ T) state. Focusing on the X^0 and X^- patterns, it can be seen that there is a strong evolution with the magnetic field of the intensity ratio between the FM and AFM lines. This reveals due to the thermalization of the A^0 population on one of the $|\pm 1\rangle$ levels depending on the field direction at high field strength. For $B_z > 0$, the population $|\Uparrow\downarrow, -1\rangle$ ($|\Uparrow\downarrow, +1\rangle$) increases (decreases), enabling their identification. Their relative position confirms the ferromagnetic character of the exchange interaction between X^0 and A^0.

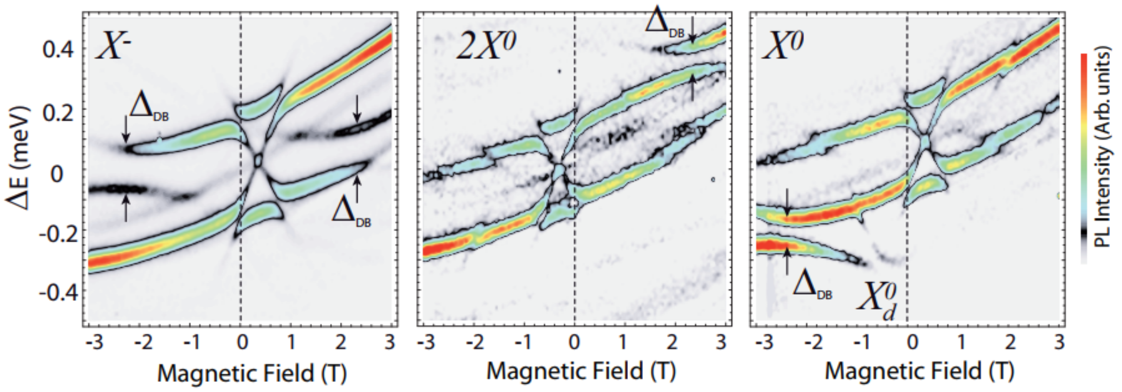

Figure 1.10: µPL intensity map of a single InGaAs QD doped with a single Mn atom as a function of longitudinal magnetic field B_z and detection energy $E - E_0$ ($E_0 = 1.2536 eV$) measured for σ^+ polarization. The three plots correspond to the X^-, $2X^0$ and X^0 states observed in the same µPL spectrum 1.8. *Images are taken from Ref. [56]*

Finally, we can discuss the crosslike pattern for the X^- state in Fig. 1.10. Considering that the crosslike pattern appears at the same positive field as for the X^0 state, the X^- transitions can be described by the same diagram as in Fig. 1.9b with the difference that the final state is electron-A^0. Therefore, one can conclude that the exchange interaction $e - A^0$ is negligible compared to δ. Comparing the X^0 and X^- spectra at $B_z = 0$ provides the precise value of this exchange ($\Delta_e \approx 20$ µeV here). If we compare the crosslike pattern for the X^- state with the one observed for the X^+ state (for another QD) in Fig. 1.11b, an interesting difference can be noted. For X^+, the cross shows up for the negative magnetic field (i.e. in σ^- polarization), while for X^-, it was detected for the positive fields. This is a similar kind of symmetry as the one observed between an exciton and a biexciton. In this case, the symmetry between X^+ and X^- corresponds to the fact that both states have the same spin configurations either in the final or initial state of the optical recombination with orthogonal selection rules due to the Pauli principle (for X^+ $|\Uparrow\Downarrow\uparrow\rangle \xrightarrow{\sigma^-} |\Uparrow\rangle$ while for X^- $|\uparrow\downarrow\Uparrow\rangle \xrightarrow{\sigma^+} |\uparrow\rangle$) [6]. The work presented in the following chapters of this thesis will focus on positive trion X^+ state. From the position of anticrossing δ for X^+ at the magnetic field $B_z = \Delta_h/2g_{A^0}\mu_B$, the value of the hole-$A^0$ exchange is determined to be $|\Delta_h| \sim 1$ meV for this QD [56]. Both electron-A^0 and hole-A^0 exchange interactions contribute to the total exchange splitting of X^+ visible transitions because: i) they have opposite signs and ii) optically active e-h pairs have opposite spins. The values of $|\Delta_h|$ and $|\Delta_e|$ depend on the Mn atom's position in QD, therefore they vary for different QDs.

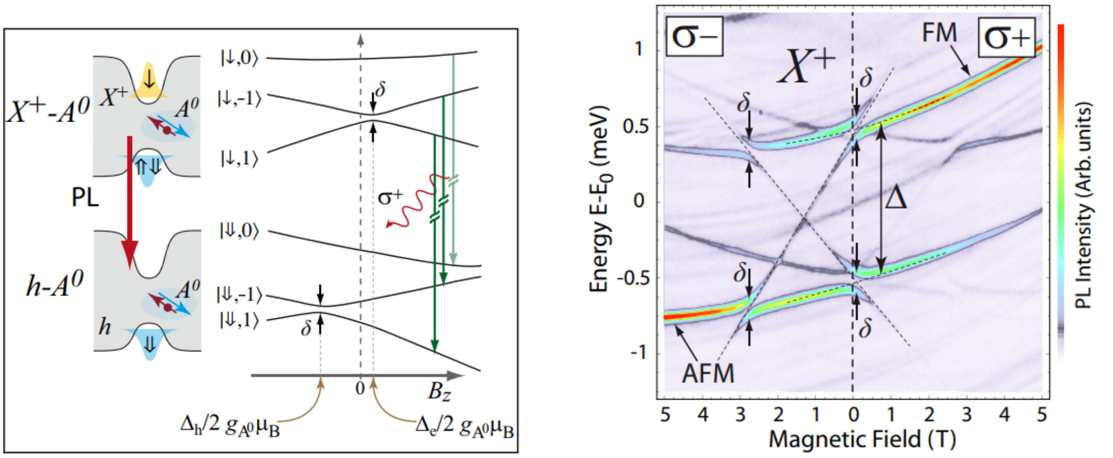

(a) (b)

Figure 1.11: (a) Diagram of energy levels involved in the transition from $X^+ - A^0$ to hole$-A^0$ state. Compared to the diagram for the X^0 state, it can be noted that, for zero magnetic field, the anticrossing δ is observed in the initial $X^+ - A^0$ state. (b) µPL spectra as a function of longitudinal magnetic field B_z and detection energy $E - E_0$ ($E_0 = 1.355$ eV) measured in σ^- and σ^+ circular polarizations, as indicated. *Images are taken from Ref. [56]*

The measurements in Fig. 1.10 show other anticrossings denoted Δ_{DB}. They result from a coupling between the heavy-holes $\Uparrow$ and $\Downarrow$ which is produced by the anisotropy related to the impurity position in the QD combined with the spatial texture of heavy-hole to light-hole mixing due to confinement [6]. For the neutral exciton, this effect results in the mixing of bright excitons $J_z^{X^0} = \pm 1$ with dark excitons $J_z^{X^0} = \mp 2$. This kind of mixing of bright and dark excitons is also observed for II-VI QDs doped with Mn [2, 74]. In fact, the pure heavy-hole approximation adopted in section 1.1.6 breaks down due to the confinement and off-center position of A^0, as discussed in the spin Hamiltonian presented in next section.

1.2.3 Theoretical model of spin Hamiltonian

A theoretical model has been constructed to understand better and describe the experimental results shown in the previous subsection [6]. This model is based on the Hamiltonian of different involved particles reduced to the spin degree of freedom. Thus, the neutral acceptor A^0 is described by two spins: the spin $S_{Mn} = 5/2$ for $3d^5$ Mn electron and spin $J_{h_1} = 3/2$ for the acceptor-bound hole h_1 . The Mn atom is located at a certain distance from the QD center, as seen in Fig. 1.12. Electronic states of QD are described by the spin $S_e = 1/2$ for conduction band electron e and spin $J_{h_2} = 3/2$ for valence band hole h_2. Depending on the occupancy of the QD (empty, neutral exciton, charged trions), the exchange interaction is introduced for each pair of present particles.

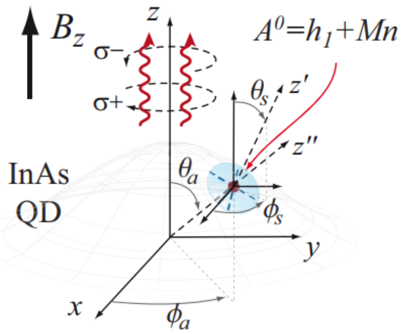

Figure 1.12: Schematics of an InGaAs QD doped with a single Mn atom that forms a neutral acceptor A^0 together with a localized hole. The Mn site lies at a certain distance from the QD center. Its position is defined by the angles θ_a and ϕ_a, while the angles θ_s and ϕ_s describe the compressive strain. *Images are taken from Ref. [6]*

The Hamiltonians of these four particles are defined as:

$$\begin{aligned}\hat{H}_{Mn} &= g_{Mn}\mu_B \hat{\boldsymbol{S}}_{Mn} \cdot \boldsymbol{B} \\ \hat{H}_{h_1} &= g_{h_1}\mu_B \hat{\boldsymbol{J}}_{h_1} \cdot \boldsymbol{B} + \hat{H}_s \\ \hat{H}_{h_2} &= g_{h_2}\mu_B \hat{\boldsymbol{J}}_{h_2} \cdot \boldsymbol{B} + \hat{H}_{HL} \\ \hat{H}_e &= g_e\mu_B \hat{\boldsymbol{S}}_e \cdot \boldsymbol{B}\end{aligned} \tag{1.6}$$

where μ_B is the Bohr magneton and g_α is the Landé factor of the particle α, which is taken to the first order as a scalar for Mn, e, h_1 and h_2.

The potential anisotropy $\hat{H}_s$ experienced by h_1 can be described by an effective strain tensor with three main axes generally different from the crystallographic axes. Thus, we introduce as the dominant term a compressive strain $\epsilon_{||}$ along the z' direction, which is defined by the angles θ_s and ϕ_s (Fig. 1.12), and an in-plane shear strain $\epsilon_\perp$ with x' and y' main axes defined by an angle ψ_s in the plane perpendicular to z'. This Hamiltonian reads as:

$$\hat{H}_s = -\frac{\epsilon_{||}}{3}\left[\hat{J}^2_{h_1,z'} - \frac{1}{2}(\hat{J}^2_{h_1,x'} + \hat{J}^2_{h_1,y'})\right] + \frac{\epsilon_\perp}{2}(\hat{J}^2_{h_1,x'} - \hat{J}^2_{h_1,y'}) \tag{1.7}$$

where the $\hat{J}_{h_1,\alpha'}$ is obtained from the operators $\hat{J}_{h_1,\alpha}$ with three successive rotations to transform z to z' (by using the matrix $e^{-i\psi_s \hat{J}_{h_1,z}} e^{-i\theta_s \hat{J}_{h_1,y}} e^{-i\phi_s \hat{J}_{h_1,z}}$).

A similar description is used for the h_2 hole confined in the QD, with $\Delta_{HL} \sim$ 30 meV the splitting between the heavy-holes and light-holes produced by the strong confinement along the z-axis. The corresponding Hamiltonian is written as:

$$\hat{H}_{HL} = -\frac{\Delta_{HL}}{3}\left[\hat{J}^2_{h_2,z} - \frac{1}{2}(\hat{J}^2_{h_2,x} + \hat{J}^2_{h_2,y})\right] \tag{1.8}$$

Here it is assumed that the exchange interactions between different particles have the form of Heisenberg Hamiltonians [70, 72], with a specific anisotropic part $\hat{H}_a$ for the $p-d$ exchange between the off-center Mn and h_2. Considering that the $e-A^0$ exchange interaction is negligible for these specific QDs, we can consider only the exchange interactions between Mn, h_1 and h_2. The exchange Hamiltonian reads as:

$$\hat{H}_X = I_{h_1-Mn}\hat{\boldsymbol{S}}_{Mn} \cdot \hat{\boldsymbol{J}}_{h_1} + I_{h_2-Mn}\hat{\boldsymbol{S}}_{Mn} \cdot \hat{\boldsymbol{J}}_{h_2} + I_{h_1-h_2}\hat{\boldsymbol{J}}_{h_1} \cdot \hat{\boldsymbol{J}}_{h_2} + \hat{H}_a \tag{1.9}$$

where $I_{\alpha-\alpha'}$ are the two-spin exchange energies considered as fitting parameters in this model. The anisotropic term $\hat{H}_a$ has been derived in [75] for a spherical QD. This Hamiltonian depends linearly on a parameter ρ which depends on the Mn position and vanishes when Mn is in the center of the QD. Even though the QDs studied in this thesis are lens-shaped without a well-defined center, the same expression for $\hat{H}_a$ was used:

$$\hat{H}_a = \rho I_{h_2-Mn}(\hat{J}^2_{h_2,z''}\hat{\boldsymbol{S}}_{Mn} \cdot \hat{\boldsymbol{J}}_{h_2} + \hat{\boldsymbol{S}}_{Mn} \cdot \hat{\boldsymbol{J}}_{h_2}\hat{J}^2_{h_2,z''}) \tag{1.10}$$

where $\hat{J}_{h_2,z''}$ is the angular momentum operator along the direction z'' defined by the angles θ_a and ϕ_a.

To generate the theoretical PL spectra, the Hamiltonians of the initial and final states are first diagonalized. The PL intensity emitted for the transitions from the initial to the final state is then calculated by considering the optical selection rules and including thermal relaxation of the A^0 population.

This model allows us to reproduce the magneto-PL measurements performed for the Faraday configuration accurately. Here we show two examples for a positive trion X^+ in two different QDs: i) standard QD ii) anisotropic QD with no really privileged axis. The experimental and corresponding theoretical simulations for these QDs are shown in Fig. 1.13 and 1.14. The parameters used to reproduce these spectra are provided in Ref. [6].

The QD (Fig. 1.13) has a characteristic X pattern already described in detail in the previous section 1.2.2. On the other hand, the second QD is an interesting example where a strong uniaxial strain $\epsilon_{||}$ along z' no longer dominates the strain anisotropy experienced by h_1. Consequently, the spectrum in the zero-magnetic field of the QD (Fig. 1.15) strongly deviates from the standard ones. Instead of doublet structures, 9 lines are observed corresponding to all 3×3 possible transitions from $e-A^0$ to h_2-A^0 as indicated by $i \blacktriangleright j$ labels (i,j=1,2,3) in the figure. The magneto-PL image of the QD (Fig. 1.14) shows many anticrossings confirming that these lines originate from the same Mn-doped QD even though no X pattern is clearly visible. The above theoretical model still reproduces the main features of this QD [6].

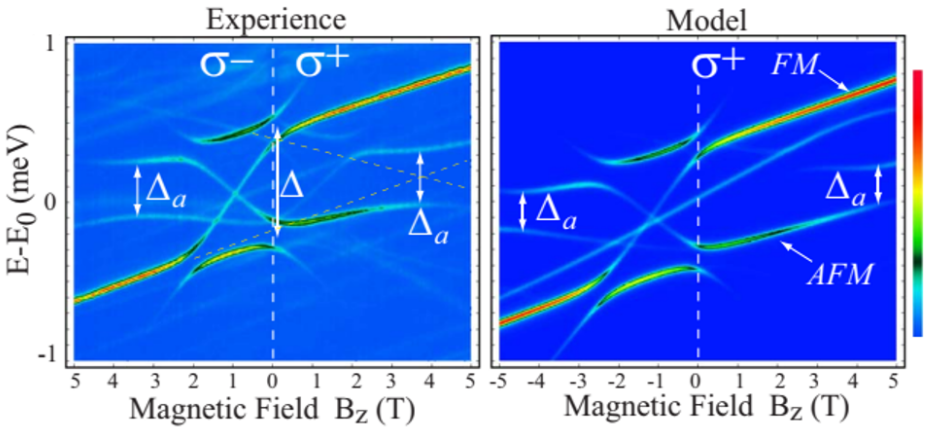

Figure 1.13: µPL spectra of a charged exciton X^+ of QD as a function of longitudinal magnetic field B_z and detection energy $E - E_0$ ($E_0 = 1.355$ eV) measured in σ^- and σ^+ polarizations (left) and theoretical simulation (right). *Images are taken from Ref. [6]*

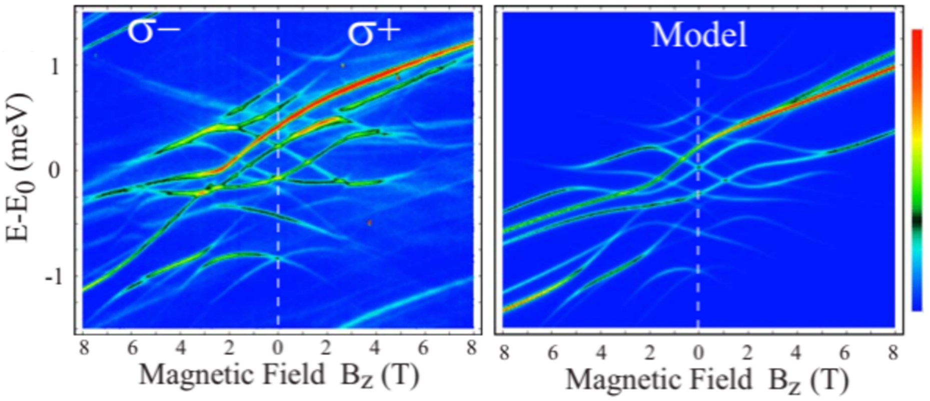

Figure 1.14: µPL spectra plot of a charged exciton X^+ of QD as a function of longitudinal magnetic field B_z and detection energy $E - E_0$ ($E_0 = 1.3525$ eV) measured in σ^- and σ^+ polarizations (left) and theoretical simulation (right). *Images are taken from Ref. [6]*

These experimental results and numerical simulations show that the studied QDs likely have a strongly uncentered Mn atom. This is in agreement with the theoretical study [71] that predicts a singlet configuration for the $h_1 - h_2$ ground state for the on-center Mn atom. Instead, in the above model, two holes occupy distinct orbitals at different positions and a finite overlap between them gives rise to the AFM coupling [6].

1.2.4 Motivations for resonant spectroscopy of Mn-doped QDs

Previous experiments and theoretical simulations of these QDs in C2N [5, 6, 18, 56] have given interesting insights into the spin interactions between the carriers and Mn impurity in InGaAs QDs. These QDs doped with a single magnetic impurity can offer an interesting alternative for the coherent manipulation of a spin qubit in the context of quantum technologies. Such an isolated magnetic spin is possibly better isolated from the influence of the environment than is the case of valence or conduction

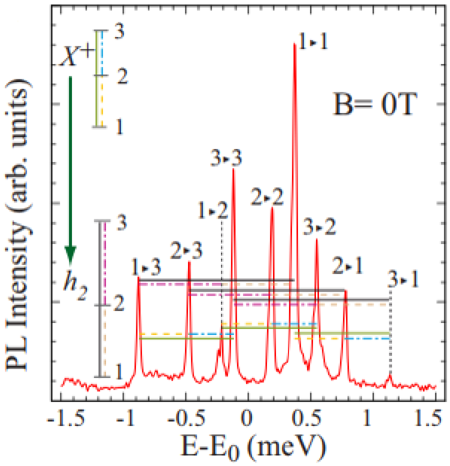

Figure 1.15: µPL spectrum for QD of X^+ at $B_z = 0$ T centred at $E_0 = 1.3525eV$. Inset shows the 3 × 3 level scheme responsible for the transitions observed in the spectrum. *Spectrum is taken from Ref. [6]*

electrons. Thanks to the $sp-d$ exchange resulting in spin-dependent levels, selective addressing of transitions by optical methods is achievable. Thus, the QD doped with a single Mn atom could present an exciting system for realizing spin-based qubits coupled to single photons, in analogy to what has been quite recently proposed for QD molecules [76]. In Ref. [13], the optical pumping and nondestructive spin readout for a singly Mn-doped QD were achieved using a specific resonant excitation scheme, limiting the fidelity to about 70%. In this thesis, the leading idea was to study Mn-doped QDs under resonant excitation, in order both to improve the fidelity of spin manipulation and to further explore the spin coherence properties of A^0 and of the FM complex hole-A^0. Initially, the thesis project was in particular to investigate the coherent population trapping of A^0 spin states $|\pm 1\rangle$ in the magnetic field where the transitions of a neutral exciton form a W-like system as discussed in Ref. [13]. Such an experiment would provide direct access to the spin coherence time $T_2^\star$. In order to realize such an experiment, it was first needed to build an efficient dark-field confocal microscope setup. The different steps for realizing such a setup are explained in detail in the next chapter.

Chapter 2

Dark-field confocal microscope setup

Self-assembled InGaAs quantum dots presented in Chapter 1 have attracted the interest of researchers because of their potential applications as single photon sources and spin qubits. To utilize these quantum dots effectively for such purposes, a deeper understanding of their intrinsic optical and spin properties is essential. Since the non-resonant excitation introduces noise resulting in additional dephasing of the interband optical dipoles or spin [77], it is crucial to use resonant optical excitation. The first method used in the QD community that enabled resonant excitation of QDs was differential transmission spectroscopy [78]. However, this method does not give access to the photons scattered or emitted by the QD. In contrast, detection of the resonance fluorescence signal is important for implementing sources of single photons with high indistinguishability which is essential for application in quantum communication. Observing resonance fluorescence (without the use of cavity effect enabling Purcell factor exceeding one) is challenging, but has already been achieved to study InGaAs quantum dots [79–82]. The optical setup used in these studies is based on a confocal microscopy setup that operates in the so-called dark-field mode, where the excitation laser is strongly rejected from the fluorescence signal on the detection path. In practice, the reflected laser light is most frequently filtered out by using crossed linear polarizations for the excitation and detection branches of a confocal setup, even though other experimental configurations are possible.

In this chapter, we will describe the development of such a dark-field confocal microscope setup and its implementation for the study of our Mn-doped InGaAs quantum dot sample. Prior to this work, these QDs had been only studied with non-resonant µ-photoluminescence spectroscopy [5, 6, 13, 18]. Developing a state-of-the-art dark-field microscope was a significant first step for both the experiments conducted during this thesis and those anticipated in the future. Despite the exceptional performance of such setup, measuring resonance fluorescence for Mn-doped QDs in samples with no cavity structure to enhance the light-matter interaction proved challenging. In principle, with a rejection of the reflected laser light better than 10^{-6}, the PL signal from a single InGaAs QD resonantly excited can be estimated to be at least one order of magnitude higher than the reflected laser light for incident powers below the saturation regime. However, as discussed below, we did not succeed in observing resonance fluorescence with our samples. Instead, thanks to the specific system of transitions of Mn-doped QDs we were still able to resonantly excite with the constructed confocal setup, one branch of a Λ-like system and detect at a slightly different wavelength the PL associated to the other branch of the Λ. The proof of principle of these experiments was first achieved with Mn-doped QDs in a Schottky diode structure. It was then employed as a new tool to better understand the properties of hydrogenated Mn-doped QDs (Chapter 3), before being extensively used to perform the resonant spectroscopy of natural Mn-doped QDs in the saturation regime (Chapter 4).

In the future, it would be beneficial to fabricate improved samples with an anti-reflection coating or an optical micro-cavity. This could enhance the light-matter interaction and the extraction of photons from the high-refractive-index semiconductor material. Utilizing such samples in combination with the dark-field microscope setup will enable the measurement of resonant fluorescence for the Mn-doped QDs. In such conditions, it would be possible to exploit the Λ-like transitions formed in the magnetic field for these QDs [13], allowing for the realization of coherent population trapping experiments as mentioned in section 1.2.4. This would provide access to the coherence time of the A^0 spin and enable the initialization, coherent manipulation, and read-out of the magnetic spin state.

The realization of the experimental method and important parameters for obtaining state-to-the-art results [29] will be explained in the section 2.1. In the section 2.2, different important steps in creating the setup are described. We analyze the importance of specific parameters such as laser extinction and stability in order to improve the setup and reach state-of-the-art results. Simulations done with the commercial software *VirtualLab Fusion* will also be discussed here. In the third section 2.3, the first measurements done with on a Mn-doped QD in a Schottky diode structure under typical experimental conditions of excitation will be presented.

2.1 Principle of the method

When a non-resonant laser excites a quantum dot, it is easy to distinguish the light emitted by the dot from the reflected laser light because the wavelengths are vastly different. However, when using resonant excitation, filtering out the reflected laser light of the same wavelength as the quantum dot signal becomes challenging. To solve this issue, the property of light, such as polarization, can be utilized. This is achieved by defining the polarization in the excitation and detection arms as orthogonal. The reflected laser light usually maintains its polarization and is therefore rejected from entering the detection arm. This dark-field method has been used in studies of InGaAs quantum dots with various degrees of success in laser rejection [79–82]. One of the most successful results in laser rejection and stability was achieved in the work of A. V. Kuhlmann et al. [29]. This work served as a starting point for building the setup used in this thesis. Thus, in this section, I will explain the principles of such dark-field microscopy and the significant findings from [29] that will help to comprehend the building process outlined in section 2.2.

The setup used in [29] is presented in Fig. 2.1a. In this setup, there are three main arms: the lower horizontal arm, which provides the excitation, the vertical arm used for light detection and the upper horizontal arm for imaging the sample surface. The

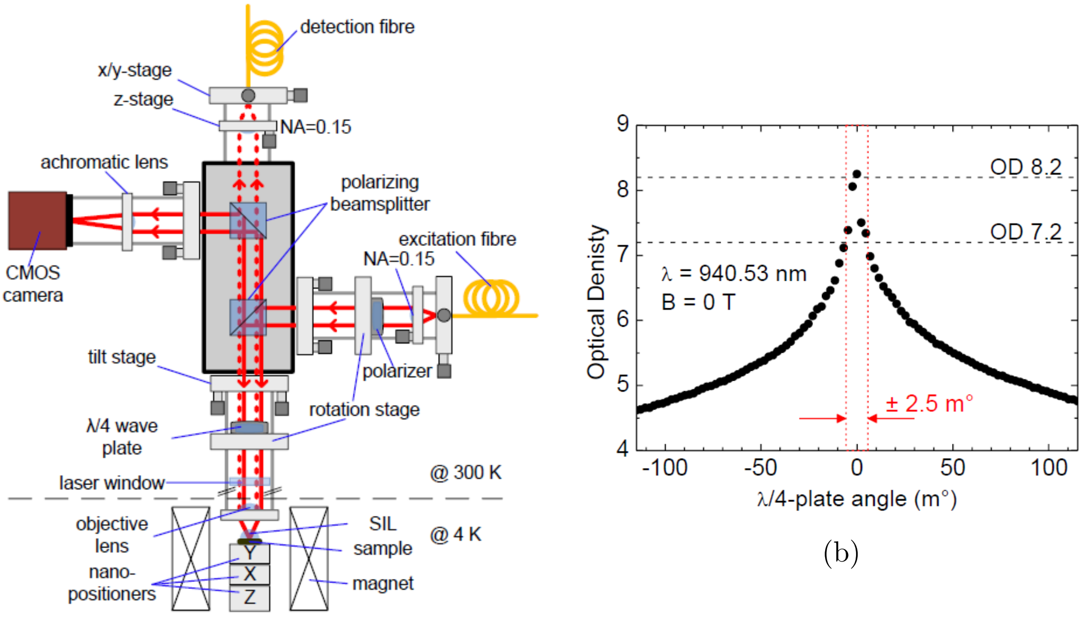

(a)

(b)

Figure 2.1: (a) Microscope setup for resonance fluorescence experiments. The InGaAs quantum dot sample (with a hemispherical solid immersion lens (SIL) in Ref. [29]) and the objective lens are inside a bath cryostat at low temperature. The rest of the setup is at room temperature. It consists of three main modules: the lower horizontal arm, which is used for the excitation, the vertical arm used for the detection, and the upper horizontal arm used for the imaging of the sample surface. (b) Sensitivity of the laser suppression to the QWP angle. The reflected laser light is recorded by a photodiode as a function of the quarter-wave plate angle, and the corresponding optical density is calculated. At the angle of optimum laser rejection (OD > 8), a very small change in the QWP angle causes the decrease of OD by one order of magnitude. *Images are taken from [29]*

crossed polarizations in the excitation and detection arms are defined with one linear polarizer, two polarizing beam splitters (PBS) and a quarter-wave plate (QWP).

The single mode (SM) fiber is used to connect the excitation laser and the excitation arm of the microscope. The output is a well-collimated beam of coherent laser light whose polarization is precisely defined by the linear polarizer. In this work, *p*-polarization is defined as the electric field direction of the laser beam parallel to the plane of incidence of the PBS, while *s*-polarization is defined as the electric field direction orthogonal to this plane. For excitation, *s*-polarized light is used. The polarizer is mounted on a piezoelectric stepping stage, allowing precise control of the polarization axis and rotation with a step as small as 1 millidegree (m°). The *s*-polarized light is then reflected by the PBS towards the QWP. The latter has a crucial role in controlling polarization because it compensates for a possible small ellipticity of the polarization. The QWP is also mounted on a piezo rotary stage, enabling very precise control and outstanding long-term stability. It should also be noted that the QWP behaves as a half-wave plate (HWP) for the reflected laser light because this light passes through it twice. The sample studied in Ref. [29] has a solid immersion lens mounted on top of it in order to enhance the collection efficiency. Together with an objective lens of high numerical aperture (NA = 0.68, f = 3.1 mm), it is situated in the cryostat at a low temperature.

In the vertical detection arm, the two PBSs reflect s-polarization. This means that the s-polarized reflected laser light is highly suppressed in the transmission, while the p-polarized component of the QD emission is transmitted in the detection arm. The light is then efficiently collected by the SM fiber and recorded by a single photon detector. The same type of optical and mechanical components are used as for the collimation of light in the excitation arm. Coupling into a SM fiber not only allows the detection of QD emission but also helps eliminate any residual reflected laser light. In addition to the well-defined crossed polarizations for excitation and detection, the use of an SM fiber in the detection arm is crucial for an efficient dark-field microscope. The significance of this becomes evident when considering that the maximal nominal extinction of a single PBS is only 10^3. The incorporation of two PBSs in the detection arm has the potential to enhance this extinction up to 10^5. However, both the two PBSs and the Glan-Thompson polarizers, that we will use, have laser extinction limitations of approximately $10^5 - 10^6$. Therefore, given the PBS limitations, achieving laser extinction exceeding 10^7 in such a setup is a remarkable result, made possible solely by employing the SM fiber in the detection arm. The SM fiber serves not only as a spatial filter but also as a modal filter. The detailed explanation of this result will be discussed in the subsequent sections.

The upper horizontal arm has a relatively simple design, consisting of just one lens that focuses the additional light source onto the camera. This configuration allows for the imaging of the magnified sample surface.

For high suppression of reflected laser light, the positions of the linear polarizer and quarter-wave plate must be adjusted with great precision. The authors have reported that the best way to do this is through iterative fine-tuning of these two components. Piezo rotary stages play an essential role in this process because they enable fine remote adjustment and excellent long-term stability. Once the best positions are found, the piezos are grounded and resonant fluorescence measurements on the QD can be performed over a long time. In order to obtain more information about the setup's performance, the authors have then studied the laser rejection by rotating the QWP angle. This makes it possible to switch between cross-polarization mode (when laser rejection is maximal) and parallel polarization mode (when there is no laser rejection). It is observed that laser rejection depends periodically on the QWP angle with a period of $\pi/4$. The maximal laser suppression is 10^8, which corresponds to an optical density (OD) of 8. The optical density is defined as:

$$OD_{exp} = -\log\left(\frac{I_{exp}}{I_0}\right) \tag{2.1}$$

where I_{exp} is the reflected laser light transmitted in the detection in cross-polarized configuration and I_0 is the intensity of reflected laser light in parallel configuration. The measurement of optical density for different QWP angles is recorded (Fig. 2.1b). A change of just a few m° can worsen laser suppression by one order of magnitude, revealing extreme sensitivity and underlining the necessity of using piezo rotary stage for QWP. Therefore, such an automated rotation stage of high precision for QWP is a crucial point that we should also implement in our setup.

Although in [29], the experimental results in Fig. 2.1b are not fitted with a theoretical curve for OD, we can note that OD would be defined as a function of QWP angle as:

$$OD_{th}(\alpha) = -\log\big(\sin^2(2\alpha) + 10^{-OD_{th}(0)}\big) \tag{2.2}$$

where α is the QWP angle. Here, we consider that since the laser beam passes twice through the QWP, it acts as a HWP, and when set to α, it induces a rotation of 2α. For two crossed polarizers, the dependence is $\sin^2(2\alpha)$. In theory, when α is zero, this would mean the total cancellation of reflected light. However, this cannot be experimentally observed due to the imperfections of the PBS and polarizers. Therefore, we introduce a small constant of $10^{-OD_{th}(0)}$, which enables us to fit the experimental curves. In the next section, we will use Eq. 2.1 and 2.2 to fit our experimental results and determine the value of the maximal OD.

Regarding stability, it has been shown that the setup of Ref. [29] can operate in set-and-forget mode. An optical density of about 7 persists over more than 30 hours, exceeding typical measurement time. However, the laser rejection is very sensitive to the change in excitation wavelength and magnetic field. Typically a change of 1 nm in wavelength requires adjustment of the QWP angle of a few m°. For an increase of the magnetic field, a significant change in the angles of the polarizer and QWP is needed, probably due to a Faraday effect of the objective lens, solid immersion lens, or sample.

These are some important parameters that need to be considered in the creation of our setup as well. The stability over time is crucial in order to perform extensive studies on the QD. We may also need to use different wavelengths for the resonant excitation of four transitions of Mn-doped InGaAs QD (Fig. 1.8). Thus, verifying that a good laser rejection is preserved over this range of wavelengths will be necessary. For eventually performing coherent population trapping experiment on Mn-doped QDs, we would need to operate at a specific magnetic field (~ 1 T) in order to access the W-like transitions. Therefore, it would be crucial to obtain a good laser suppression under this fixed magnetic field. In the next section, we will go over the most important steps in building our setup and explore the influence of these parameters on its performance.

2.2 Dark-field microscope

2.2.1 The influence of focusing lens on optical density

As discussed in the previous section, in order to build a dark-field microscope, we must have well-defined orthogonal polarizations in the excitation and detection arm. Therefore, we began building a simple setup with two Glan-Thompson polarizers (Fig. 2.2a). Initially, we use just a He-Ne laser as a light source. First Glan-Thompson polarizer (P1) is situated in the excitation arm and defines the excitation beam polarization as vertically polarized (V). Instead of using two polarizing beam splitters as in [29], we use one beam splitter (BS), which helps us separate excitation and detection arms, and a second Glan-Thompson polarizer (analyzer) in the detection arm (P2). The orientation of P2 is such that it only transmits horizontally polarized (H) light.

This means the reflected laser light, which is polarized vertically will be suppressed by P2. We also use a quarter-wave plate (QWP) mounted on a motorized rotatory stage, and its effect on OD is examined here. At first, we study the extinction of the laser reflected from a simple reflective surface such as a silver mirror (M2). We also place a second beam splitter (BS2) in the detection arm, which reflects one part of light in such a way that we can monitor the profile of the beam in the detection arm. The transmitted part of the light after BS2 is focused on the Jobin Yvon spectrometer equipped with a Ni-cooled CCD camera for detection of the dispersed light.

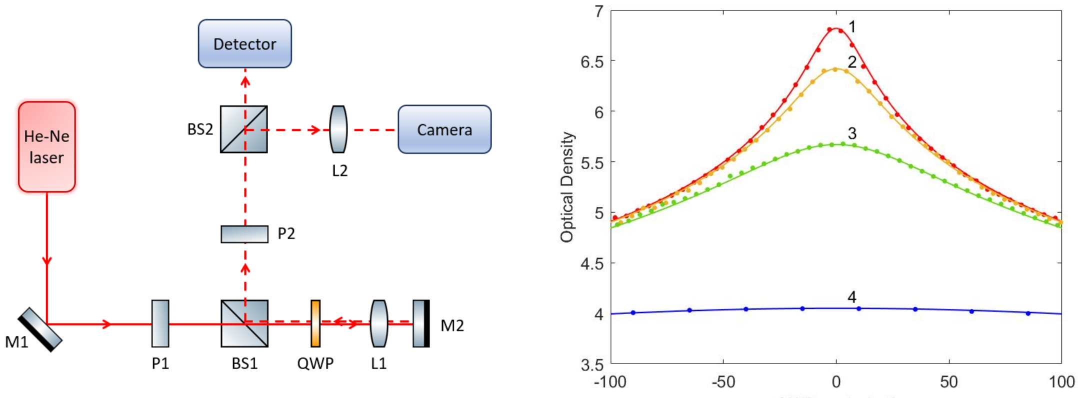

(a)

(b)

Figure 2.2: (a) Schematic view of the setup used to investigate the effect of different focusing lenses on laser rejection. He-Ne laser light is vertically polarized by polarizer (P1). It passes through beam splitter (BS1) and quarter-wave plate (QWP) and it is focused on the mirror (M2) by lens (L1) for which lenses with different focal lengths are used. The reflected signal is then going in the detection arm where it passes through the cross-polarized polarizer (P2) before being detected by the CCD camera. (b) The optical density measured as a function of QWP angle in four different cases: 1) with no lens L1 or with the lens L1 of focal length 2) $f = 50$ mm, 3) $f = 20$ mm and 4) $f = 4.5$ mm.

In Ref. [29], a lens of high numerical aperture (NA = 0.68) was used as an objective lens to focus the laser light on the surface of the sample. In this section, we examine the influence of the focal length of the focusing lens (L1) on the efficiency of laser rejection. Therefore, we measure the dependence of optical density as a function of QWP angle (as shown in Fig. 2.1b) for different lenses (L1). As it is shown in Fig. 2.2b, we repeated this experiment with no lens (or infinite focal length) and with L1 lenses of focal length $f = 50$ mm, $f = 20$ mm and $f = 4.5$ mm. In the case where no lens is used, the maximal measured OD is 6.8 (curve 1 in Fig. 2.2b). This maximal OD value exceeds the laser extinction of Glan-Thompson polarizers provided by the manufacturer, which is limited to 10^5, i.e. OD = 5. As seen in Fig. 2.2b, OD above 6 is achieved for a very narrow range of QWP angles. A change in QWP angle of only 100 m° results in drop of OD below 5. When a lens L1 is introduced for focusing on mirror M2, the laser extinctions is diminished. The optical density decreases with the decrease of focal length of lens L1. For lens with $f = 4.5$ mm, OD is around 4 (curve

4 in Fig. 2.2b).

The improvement in laser extinction beyond the limits imposed by the polarizers for some of the curves in Fig. 2.2b can be attributed to the presence of the QWP in the path between the two polarizers. As mentioned in Ref. [29], the role of this plate is to compensate for any introduced polarization ellipticities. These ellipticities, or possibly just the rotations of the main polarization axis, could be introduced by elements of the setup, such as the PBS used in Ref. [29] and later in our setup. Moreover, another important function of the QWP is the additional degree of freedom it provides. With precise adjustment of the QWP angle using the motorized rotatory stage, it is possible to optimize laser extinction more effectively. This precise control allows us to record the dependence of OD on the angle α, as shown in Fig. 2.1b, and thus to quantitatively determine with Eq. 2.2 the achieved optical density.

As mentioned above when deriving Eq. 2.2, since the laser beam passes twice through the QWP, its function is essentially the same as an HWP in this setup. Therefore, one could consider replacing the QWP with an HWP placed in the detection arm before P2. This change could still enable fine angle control and compensation of any ellipticities or polarization rotations. Although this has not been experimentally tested in our setup, the theoretical model developed in Section 2.2.7 yields exactly the same results in both cases.

2.2.2 Clover-leaf pattern: origin and simulation

To investigate the impact of lens on the laser extinction, we check the image of the reflected beam recorded with a camera placed in the reflected path after BS2. When QWP angle is $\alpha = 0°$, i.e. cross-polarization regime, we observe that the reflected beam forms a specific 4-leaf clover pattern as seen in Fig. 2.3a. As we increase the QWP angle, a single circular spot starts to appear (Fig. 2.3b) and becomes the strongest for $\alpha = 45°$, i.e. parallel polarization. The center of this spot is at the same position as the center of the 4-leaf clover pattern.

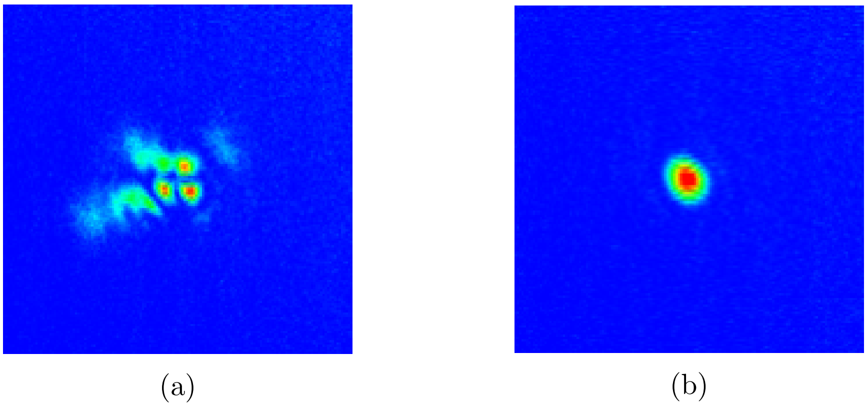
(a) (b)

Figure 2.3: Images of reflected beam in case of (a) crossed polarizations ($\alpha = 0°$) and (b) parallel polarizations ($\alpha = 45°$) of incident and reflected beams. The images are recorded by focusing the reflected beam with lens L2 on the CCD camera, and plotted here with a color scale in arbitrary units. The intensity of the laser was significantly reduced for the parallel configuration to avoid camera saturation.

The same kind of pattern can be observed in the simulations created by the software *VirtualLab Fusion 2023*. A virtual optical setup containing main elements of our experimental setup (Fig. 2.2a) was generated according to the scheme presented in Fig. 2.4a. As the source of light, a Gaussian wave with a waist radius set to 2 mm and linearly polarized along x direction is chosen. The wavelength is 930 nm which corresponds to the typical wavelength of the laser used to resonantly excite the InGaAs QDs. To simulate a lens of high numerical aperture (NA), we use an ideal lens of focal length $f = 2.4$ mm. For the considered Gaussian beam, this corresponds to NA$= 0.64$, the same as for the actual experimental setup used in the rest of this thesis. To simulate the sample, we use a GaAs slab of thickness 300 µm at room temperature. The light is then reflected from the GaAs slab (red line in Fig. 2.4a), and it passes again through the same ideal lens ($f = 2.4$ mm). After that, the light passes through the polarizer and it is detected by a "universal detector" which evaluates the vectorial components of the electromagnetic field of an incoming light. Depending on direction chosen for the polarizer, along x or y direction, the detector measures here the squared amplitudes of the E_x (Fig. 2.4b) or E_y (Fig. 2.4c) components of light, respectively. Clearly, this simulation provides the same patterns as those experimentally observed for parallel and cross-polarized reflected light as in Fig. 2.3.

The clover-leaf pattern for the reflected beam in orthogonal polarization was already observed and described in literature for similar experimental setups [83]. When a lens of large numerical aperture is used to focus a linearly polarized Gaussian laser beam (in TEM_{00} mode), parts of the reflected light are coupled to a different mode (TEM_{11}-like) of orthogonal polarization resulting in the characteristic 4-leaf clover pattern. The reasons for this coupling to a TEM_{11}-like mode of orthogonal polarization comes from the difference of Fresnel coefficient for reflection under a non-zero angle of incidence for the s- and p-plane of polarizations. Indeed, only the rays in the incident beam which are focused with their polarization direction (after the lens) purely in a s- or p-plane do not undergo polarization conversion, resulting in the dark cross in Fig. 2.4c with axes parallel and orthogonal to the direction of the incident beam polarization. However, for rays with polarization decomposing equally in the s- and p-planes, the conversion is maximum and increases with the angle of incidence, explaining the observed 4-leaf clover. Clearly, the higher the numerical aperture (NA), the larger the spread of incident angles after the focusing lens, and consequently, the amount of light reflected with orthogonal polarization increases.

The quantitative influence of the focusing lens numerical aperture on the clover-leaf pattern and the OD can also be investigated through simulations with an ideal lens. We can estimate the optical density for this simulation using the formula from Eq. 2.1, where I_{exp} (I_0) corresponds to the total intensity of the y-component (x-component) of the reflected light, respectively. These total intensities are calculated in *VirtualLab Fusion* as the sum of the values of squared amplitudes in Fig. 2.4b and Fig. 2.4b and they are equal to $I_x = 2490(\mathrm{V/m})^2$ and $I_y = 12.5(\mathrm{V/m})^2$. Therefore, the resulting OD amounts to only 2.3 in the case of the ideal lens of $f = 2.4$ mm and NA$= 0.64$. If we replace this lens in the setup in Fig. 2.4a, with a lens of longer focal length (resulting in smaller NA), we obtain $OD = 3.2$ for 4.5 mm focal length (NA=0.4) and $OD = 5.7$ for 20 mm focal length (NA=0.1). These simulations show a similar dependence of the optical density on the focusing lens NA as we observed experimentally when focusing

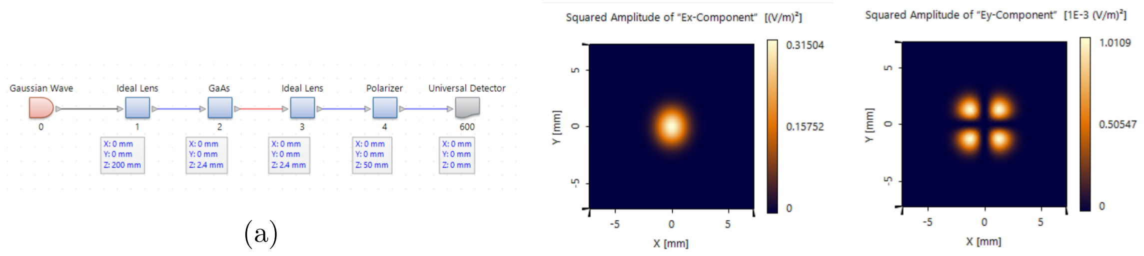

(a) (b) (c)

Figure 2.4: (a) Schematic of the setup used for simulations in *VirtualLab Fusion* program. The position of the element of optical setup is indicated below it, as the distance from the previous one. The blue lines between the elements mean the light is transmitted through them, while the red line indicates the path of reflected light. The "universal detector" records then the images of squared amplitude of E_x component (parallel configuration) (b) and squared amplitude of E_y component of reflected light (cross configuration) (c).

on a silver mirror (instead of a GaAs slab) with different lenses in Fig. 2.2b. Thus, the observed clover-leaf pattern in the cross configuration is clearly responsible for the degradation of laser rejection when the numerical aperture of the effective focusing increases.

Consequently, to improve laser extinction in a confocal setup that utilizes a high-NA lens for collecting photoluminescence from a single emitter, it is crucial to select only the central part of clover-leaf pattern, where the intensity of laser light is minimal, and filter out the rest. This can be done using a pinhole or a single mode fiber. In the following section, these two methods will be explained, compared, and the one demonstrating better performance will be selected and implemented in the final setup.

2.2.3 Filtering the central part of clover

When focusing lens with high NA is used, one of the ways to improve the optical density is to insert a spatial filtering system in the detection part of the setup. Spatial filtering is commonly used to modify or filter some plane wave components of a beam. It is usually done by using a first lens to Fourier transform the beam. In the focal plane a pinhole or mask is placed, and lastly, a second lens is used to transform back the beam [84]. This technique is widely used for cleaning up beams, removing artifacts and producing a spatially uniform Gaussian beam.

The realized experimental setup using the spatial filtering technique is depicted in Fig. 2.5. With respect to the previously used setup a few changes are introduced. Firstly, instead of He-Ne laser, a laser (Toptica DL pro) with appropriate range of wavelengths ($905 - 985$ nm) for QD excitation is employed. After the QWP, instead of focusing on a mirror, a real QD sample is glued to a sample holder which is then fixed behind the aspheric lens ($f = 2.75$ mm, NA=0.64). This objective lens is mounted on an Attocube piezo stage consisting of three piezo-electric stepping motors that allow very precise control of the position of this lens. All these elements are mounted together on the cryostat cold finger. The cold finger system is then placed in the superconducting split-coil magnetic cryostat (Oxford Instruments). The cryostat is installed on an optical table positioned about 2 m away from the main optical table, which contains the rest of the optical setup. Initially, we measure the optical density of laser rejection for the sample inside the cryostat at room temperature. After that, the sample is cooled down to about 2 K. The superconducting coils in this cryostat can be used to apply either longitudinal magnetic field (Faraday configuration) or transverse magnetic field (Voigt configuration). Spatial filtering system is placed in the detection arm after the second polarizer (P2). Its first element is an aspheric lens (L1) of focal length $f = 150$ mm. At the focal distance from it, a metallic plate with different pinholes is placed. This plate is fixed on a manual linear translation stage which allows precise control of the pinhole position in all three directions. Lastly, a second collimating lens (L2) with $f = 150$ mm is placed behind the pinhole. After these spatial filtering elements, the second beam splitter (BS2) is introduced, which allows us to record with camera the image of the beam after spatial filtering. In this way, we can monitor which part of the clover-leaf pattern is filtered.

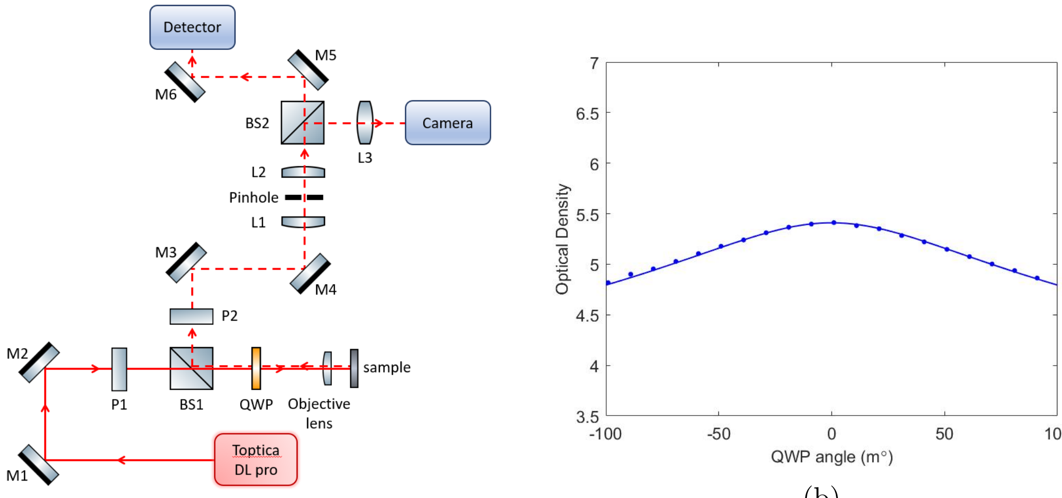

(a)

(b)

Figure 2.5: (a) Schematic view of the setup used for pinhole spatial filtering of clover-leaf pattern. Spatial filtering system consists of two lenses L1 and L2 and a pinhole at a focal plane between them. The sample is mounted together with large NA lens and placed outside the cryostat on the same optical table with the rest of the setup. (b) The optical density measured as a function of QWP angle for filtering using a pinhole with a diameter of 50 µm.

When pinholes with diameters above 80 µm are used, most of the clover-leaf pattern passes through the pinhole and leaves are still recovered on the image recorded by the camera after spatial filtering. The pinhole of 60 µm filters out some of the light of the clover-leaf pattern, but not sufficiently to significantly improve the laser extinction. The best performance is observed for a pinhole of 50 µm diameter which efficiently filters out the clover leaves with moderate attenuation of the beam transmitted in parallel configuration. A measurement of the optical density as a function of the QWP angle (Fig. 2.5b) shows an improvement of the laser extinction (OD = 5.4 at maximum) as compared to the results obtained with the shortest focal length lens

(f = 4.5 mm) in previous section (OD = 4, see Fig. 2.2b). However, this level of laser extinction is still not sufficient to perform resonance fluorescence on a single QD. Ideally, we want to achieve near state-of-the-art laser extinction (at least OD $>$ 7). Therefore, using spatial filtering with a 50 µm pinhole does not enable us to reach such performance. This simple solution was thus found to be inadequate, leading us to employ the method of modal filtering with a single mode (SM) fiber, similar to what is actually done in Ref. [29, 80].

The modified setup employing a SM fiber for filtering out the clover-leaf pattern is shown in Fig. 2.6. The beam splitter BS2 and the visualisation camera are placed between the polarizer P2 and the single mode fiber. BS2 can be rotated to image either the sample or the input face of the SM fiber. The part of the collected light that is transmitted through BS2 is then orientated by mirror M4 toward an aspheric lens (f = 25 mm) which focuses the light into the core of a SM fiber (designed for 780 nm and polarization-maintaining). This lens is mounted in an x/y-translation stage while the SM fiber is mounted in a z-translation stage which allows precise control of coupling. The other end of the fiber is mounted together with a collimator in an x/y-translation stage. The collimated beam is then sent toward the spectrometer and CCD for detection. On this path, a flipping beam splitter (BS3) is placed in order to couple back into the fiber a near-infrared broadband light from a light-emitting diode (LED). This light, represented with orange lines in Fig. 2.6, serves to illuminate the core of the fiber. In this way, we can image the clover-leaf pattern which is reflected on the input surface of the fiber (Fig. 2.7a) with respect to the fiber core (Fig. 2.7b). This is a precious aid in the initial rough alignment of the fiber core with the center of the clover.

After this, a fine adjustment of the fiber position is made by looking at the signal measured on the spectrometer CCD. When a minimum is found, this means that only the central part of the clover is coupled into the fiber and the rest is successfully filtered out. The filtering can then be further improved by fine adjustments to the polarizer P2 or QWP angle. If we then move the fiber vertically (horizontally), we should observe two maxima - one up (left) and one down (right) with respect to the minimum previously found. These maxima correspond to the case when the leaves of the clover are coupled into the fiber. Therefore, laser extinction is very sensitive to the position of the fiber. This emphasizes the importance of using the translation or piezo stage for fine-tuning of elements such as fiber, polarizers and QWP, as suggested in Ref. [29].

When the measurement of OD as a function of QWP angle is repeated as before, the achieved maximal OD is significantly improved reaching values above 7, as seen in Fig. 2.6b. The reason for such a high laser extinction lies in the fact that the collection by a SM fiber acts as a modal filter which prevents propagation of a TEM$_{11}$ mode even if the fiber core is not significantly smaller than the extension of this mode. Since the clover-leaf patterns corresponds to a TEM$_{11}$-like mode (inherently generated by the confocal setup in orthogonal polarization as discussed above), it also cannot couple to the TEM$_{00}$ mode of the fiber for symmetry reasons [85]. Namely, the electric field amplitudes in the different clover leaves are dephased by π from each other, and therefore cancel out in the overlap integral with the symmetric TEM$_{00}$ mode of the fiber. Thus, to ensure the best modal filtering, the actual clover-leaf pattern should be

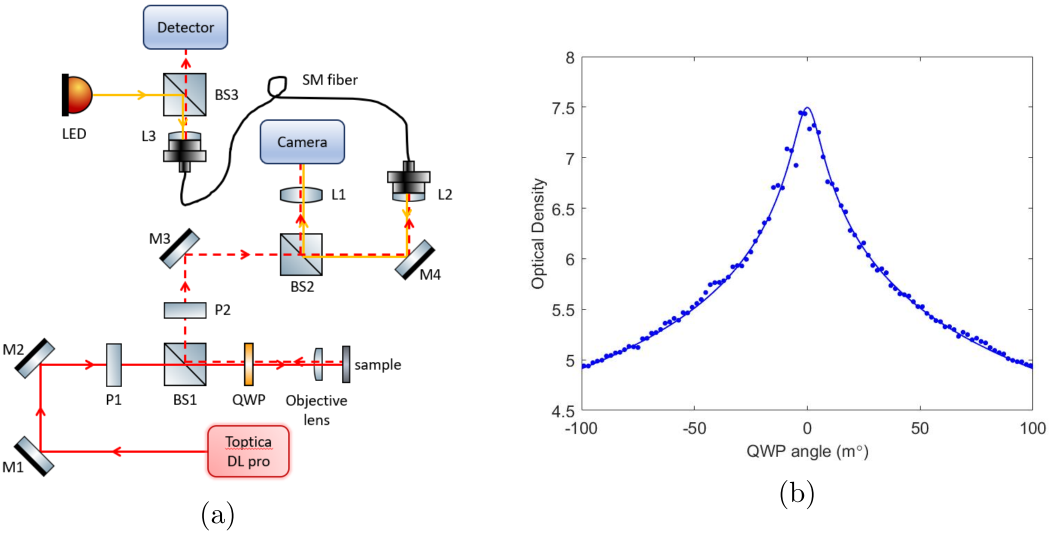

(a) (b)

Figure 2.6: (a) Schematic view of the setup used for filtering the central part of the clover-leaf pattern with a single mode (SM) fiber. The beam splitter BS2 can be rotated to image either the fiber input or the sample. The beam splitter BS3 and the LED are used to illuminate the fiber core observed on the fiber input, to precisely position the fiber with respect to the clover-leaf pattern. The sample and objective lens are placed inside the cryostat, but the measurements are first done at room temperature. (b) Optical density measured as a function of QWP angle with SM fiber-based filtering.

perfectly symmetrical and perfectly centered on the fiber input. This notably requires that the sample surface is perfectly parallel to the plane of the aspheric focusing lens, and that both of them are orthogonal to the incident beam. If some asymmetry is observed in the image of the clover, we then proceed by slightly rotating the sample holder, which generally resolves the issue and effectively improves laser extinction.

Therefore, these preliminary measurements show that the dark-field confocal microscope, which uses a collection fiber as shown in Fig. 2.6, provides so far the best laser extinction by exploiting both the polarization and spatial properties of the reflected light. However, the setup in Fig. 2.6a showed some fluctuations and decay of OD over time, which could be due to the distance between the main optical table with most of the optical elements and the optical table where the cryostat containing the sample is installed. For that reason, we eventually decided to transfer most of the optical elements to the same optical table as the sample and to use also a SM fiber for the excitation. This process involves coupling four lasers on the main optical table into a SM fiber (excitation fiber), building a setup similar to the one in Fig. 2.6 in front of the cryostat/sample on the separate optical table, and sending back the light from the collection fiber to be detected by the spectrometer CCD on the main table. These steps are detailed in the following sections.

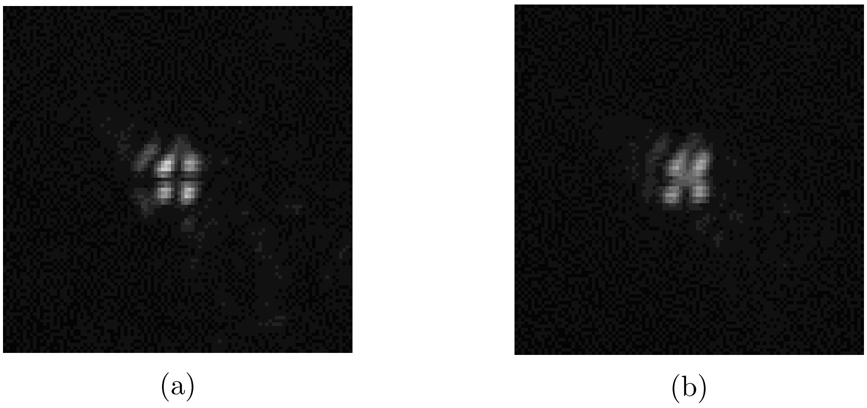

(a) (b)

Figure 2.7: (a) Image of the beam partially reflected from the input surface of the fiber recorded by the camera after BS2. The characteristic clover-leaf pattern is observed. (b) In addition to this reflected beam, we see the white light that is coupled into the fiber when the LED is switched on. This allows for the easy alignment of the fiber core with respect to the center of the clover.

2.2.4 Coupling of lasers

To build an optical setup on the same table as the sample, we need to first couple all the excitation lasers into the same fiber on the first table and mount the other end to the z-translation stage in the excitation arm. We have four different lasers that will be used for the measurements presented in this thesis. A He-Ne laser (λ=632.8 nm) and a Ti:Sapphire laser (λ=700-1000 nm) will be used for non-resonant excitation. Exciting at higher energies than the energy of QDs produces a spectrum similar to Fig. 1.8, enabling us to find the potential Mn-doped QDs by spatially scanning the sample. We will also use two Toptica lasers: a Toptica DL pro with tunable wavelengths in the range of 905-985 nm and a Toptica DLC pro with a wavelength range of 910-980 nm. These two narrow-band cw lasers will be used for resonant excitation of Mn-doped QDs.

To couple these four lasers, we start by coupling the two Toptica lasers into a 2×2 polarization-maintaining fibered coupler. One of the coupler outputs is mounted together with a collimator in an x/y-translation stage, after which these lasers are on a free path. Using two beam splitters all four lasers are aligned along the same optical path. An aspheric lens with a focal length of $f = 20$ mm, mounted in an x/y-translation stage, focuses these lasers into the core of the SM fiber (Thorlabs 780 nm polarization-maintaining single mode patch cable), which is in turn mounted in a z-translation stage. Given that the Toptica lasers, Ti:Sapphire and He-Ne lasers operate in different wavelength ranges, achieving the same fiber coupling with a simple aspheric lens for all of them is unfeasible. Therefore, the z-translation stage is adjusted to optimize fiber coupling specifically for the Toptica lasers (around 900 nm) used in resonant excitation.

Another important aspect of this part of setup involves the possibility to adjust separately the power of each laser. The power output of the Ti:Sapphire and He-Ne lasers is regulated using neutral density filters before they combine into the shared optical path. However, since two Toptica lasers are introduced into the fiber coupler, the introduction of neutral density filters after the collimator affects the power of both lasers. An additional means of controlling the power of the Toptica DLC laser is implemented through software control.

2.2.5 Building a compact setup

Excitation and detection arms

To build a more compact setup at the same table as the cryostat with sample, we use the same principle as shown in Fig. 2.6a. The schematic view of the final setup is shown in Fig. 2.8a together with the picture of actual setup as seen in Fig. 2.8b. The excitation fiber into which four lasers are coupled is mounted in a z-translation stage. The aspheric lens (L1) with $f = 18$ mm mounted in an x/y-translation stage is focused on the fiber end and collimates the laser light into a Gaussian beam. Similar as in the previous experiments, we introduce the first polarizer (P1) in the excitation arm. This polarizer defines the polarization of the excitation beam, and in our case, the polarization transmitted through it is set to be horizontal. To separate the excitation and detection arms, the beam splitter is used in the same way as before. In the first version of this setup, we started with standard non-polarizing beam splitter, but to collect all photons emitted by a QD in the orthogonal polarization, we actually install a polarizing beam splitter (PBS1) similarly as in Ref. [29]. This PBS1 transmits the horizontally polarized excitation beam which then passes through QWP and cryostat window to be finally focused by the objective lens ($f = 2.75$ mm, NA$= 0.64$) on the sample surface. The portion of the reflected laser beam for which the horizontal polarization is preserved will be transmitted by the PBS1 with 90% efficiency. Conversely, the vertically polarized part of reflected light will be reflected by PBS1 into the detection arm with an efficiency of 95%. In Ref. [29], two such PBS are used instead of the second polarizer in the detection arm to reject the reflected laser light. However, we still keep the second polarizer (P2) in the detection arm, which is set to allow only vertically polarized light to pass through. By using a standard non-polarizing BS and P2 (Fig. 2.6a) together with the SM collection fiber, we were already able to reach near state-of-the-art extinction of laser light (OD>7). By replacing the BS with PBS, we are able to collect more efficiently the QD signal. However, this does not improve significantly the laser extinction. We are still able to obtain OD>7, as it will be shown later. After the polarizer P2, the extinction of reflected laser light is performed by using the single mode fiber as described in the section 2.2.3. The aspheric lens and single mode fiber are the same as in the excitation arm and mounted with the same type of translation stages for precise alignment. The other end of fiber is brought back to the main optical table where it is mounted in a standard kinematic mount. An aspheric lens ($f = 20$ mm) is used to collimate the light from the fiber, which is then refocused on the entrance slit of the double spectrometer (Jobin-Yvon HRD600).

Imaging arms

In Fig. 2.8a, it can be observed that there are two side arms introduced by beam splitters in the excitation and detection arms. These side arms help in the imaging of the reflected beam and the sample surface. After the excitation fiber and aspheric

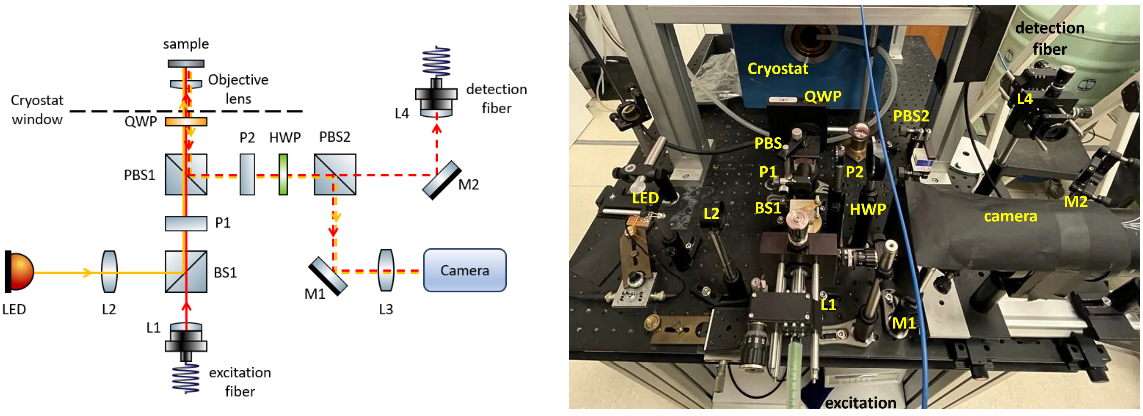

(a) (b)

Figure 2.8: (a) Schematic view of the dark-field microscope setup that will be used for resonant excitation of InGaAs QDs. The sample and objective lens are placed inside the cryostat and the measurements are done at low temperature (T= 2 K). (b) Picture of this setup in the laboratory.

lens L1, the beam splitter (BS1) is positioned. In the reflection path of BS1, we have installed a LED ($\lambda = 900$ nm) and a lens (L2) that helps focus the diode light. This light is then reflected by BS1 and travels through the excitation arm up to the sample. The image of the sample surface illuminated by this diode light is captured by a camera equipped with a 200 mm lens (L3), placed in the reflection path of PBS2. In this way, we can either image the surface of the sample by shining the LED light on it, or we can image the reflected beam in order to observe the clover-leaf pattern, as depicted in Fig. 2.3.

Between P2 and PBS2, a half-wave plate (HWP) is placed. This HWP enables us to easily switch between imaging and detection working modes without moving PBS2. When the HWP is set at a 45° angle, it transforms a small portion of horizontally polarized reflected laser light that has passed through PBS1 and P2 into vertically polarized light, which can then be reflected by PBS2 and imaged by the camera. When we do not want to use the imaging arm, but we want to send the signal through the detection fiber to the CCD, the HWP is adjusted to a 0° angle. In this configuration, the HWP effectively enables a seamless transition between the two modes (image/measure) without introducing any beam deviation, which could negatively impact the coupling to the fiber.

Alignment procedure

Alignment of the elements presented in Fig. 2.8a plays a crucial role in achieving the good laser coupling (in parallel polarization) and extinction (in cross polarization). First, the components of the excitation arm are installed and roughly aligned. Then the imaging arms are introduced to help with the fine alignments of the excitation beam on the sample. We first look at the beam image when both polarizers are in the parallel position. The recorded image of a slightly defocused laser light reveals diffraction rings due to the finite aperture of the aspheric lens used to focus the beam on the sample surface. By adjusting the translation stages of L1 and excitation fiber, we try to obtain a symmetrical image of concentric diffraction rings, ensuring in this way that the laser beam is centered on the objective lens.

Next step is installation of the detection arm. The biggest challenges here are coupling of the light into the detection fiber and the adjustments of P1, QWP, P2 and detection fiber to achieve OD> 7. In order to adjust the position of the elements in the detection arm, we feed the other end of the detection fiber to another laser at the same wavelength as the laser used for excitation. In this way, we can send the laser light through the detection fiber back to PBS2 and PBS1 up to the sample. The reflected beams originating from both the excitation and detection fibers are then imaged by the camera. To obtain the good alignment and coupling, these two reflected beams should appear at the same spot in the image, and their diffraction rings should perfectly overlap with each other. This is achieved by adjusting the orientations of PBS1 and M2 with a beam walk technique.

After that, the coupling of light into the fiber is finely adjusted using the translation stages of L4 and the detection fiber to optimize reflected light collection by observing its spectrum when P1 and P2 are parallel. Once the coupling is adjusted, the positions of the crucial elements controlling polarization should be set, except for P2. The polarizer P1 is already fixed with its transmission axis in horizontal position and then the axis of P2 is set to the vertical position (cross-configuration). Fine optimisation of polarizer P2 is achieved by adjusting its position to minimize the collected signal. The QWP and HWP are both set at 0°. Finally, we perform the last adjustments of the translation stages of L4. As explained in the section 2.2.3, when we move lens L4 horizontally or vertically we should observe two maxima and a minimum between them in the spectrum. We fix the screws of translation stages of L4 at the positions for which we observe the minimum intensity of reflected laser. After this, the positions of P2 and QWP should be further adjusted. We move the screw of P2 mount and the motorized rotary stage of QWP in small steps until we obtain the minimal intensity. Then the position of L4 can be again slightly corrected. This process is repeated until the best extinction of reflected laser light is achieved. When close to the best extinction, the measured reflected laser signal is very sensitive to all three parameters (position of L4, P2 and QWP).

2.2.6 Stability and wavelength dependence

Once all the elements of setup are adjusted, we measure the optical density (OD) as a function of QWP angle, as shown in Fig. 2.9a. Similar as in the preliminary setup with detection fiber (Fig. 2.6b), the achieved OD is above 7 which should be sufficient for an efficient laser extinction in a resonance fluorescence experiment on a single QD. Comparing the Fig. 2.9a with the Fig. 2.6b for the setup on the other optical table, it can be noticed that the curve in Fig. 2.9a is smoother. Building a compact setup on the same optical table as the cryostat was beneficial in the reduction of fluctuations of signal and noise which was present in Fig. 2.6b due to the distance between the elements of the setup. This was further verified by performing the measurement of OD over a period of time to test the time stability of the laser extinction. As shown in Fig. 2.9b, the OD on average is above 7 and does not decrease significantly during one hour. This means that once the setup is adjusted and extinction maximized, we can perform long series of measurement without having to readjust it.

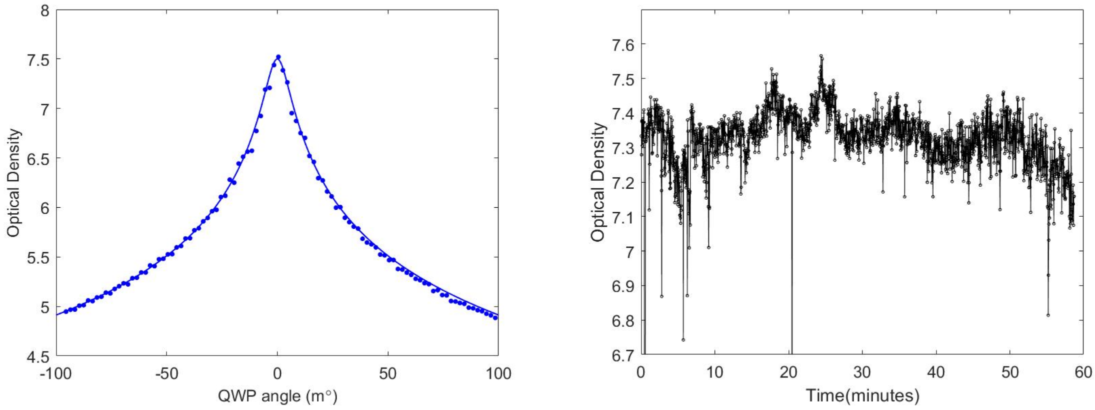

(a) (b)

Figure 2.9: (a) The optical density measured as a function of QWP angle at T= 2 K. (b) Measurement of optical density as a function of time for testing the long-term stability of the setup.

Except time stability, another important property of the dark-field microscope setup is the laser extinction dependence on the wavelength. Ideally, the setup should maintain sufficiently high extinction over the range of wavelengths that we will used when scanning through the QD transitions, which is typically of the order of 100 pm. To test this, we first adjust the setup as described previously to achieve OD > 7 for a reference laser wavelength of $\lambda_0 = 929.0843$ nm. For analyzing the influence of wavelength on OD, we do a scan for a range of 51 wavelengths around λ_0. For each wavelength, we repeat the same measurement of OD as a function of QWP angle, similar as in Fig. 2.9a. The data of these scans are collected and presented in the form of intensity map in Fig. 2.10a. The graduation of the x-axis in this figure is not linear due to the non-linear change of wavelength through the voltage control. The small jumps that can be noticed around 39 pm and 136 pm are the consequence of more pronounced laser mode hops. It can be seen that for most of the wavelengths below $\lambda_0 = 929.0843$ nm, the optical density has dropped below 6 and it is gradually decreasing as well for the wavelengths above λ_0. In addition, it can be observed that the maximal OD is obtained for different QWP angles once the wavelength is changed. This shows that the OD > 7 is very sensitive on the change of wavelength and that the QWP angle should be adjusted when OD drops significantly.

To investigate closely the reason for the decrease of OD when the wavelength is changed, we looked at the image of clover-leaf pattern. Starting from the quite symmetrical clover for λ_0 (Fig. 2.10b), when wavelength is changed we observe that the shape of clover is significantly changed (Fig. 2.10c and 2.10d) proving the importance of clover symmetry for reaching high laser extinction. After careful investigation of the possible origin of this issue, we concluded that this effect most likely comes from the interferences of light reflected from the back surface of sample and randomly polarized. This could be potentially eliminated by fabricating a sample with mirror-polished back side, but we did not explore further this solution with our Mn-doped

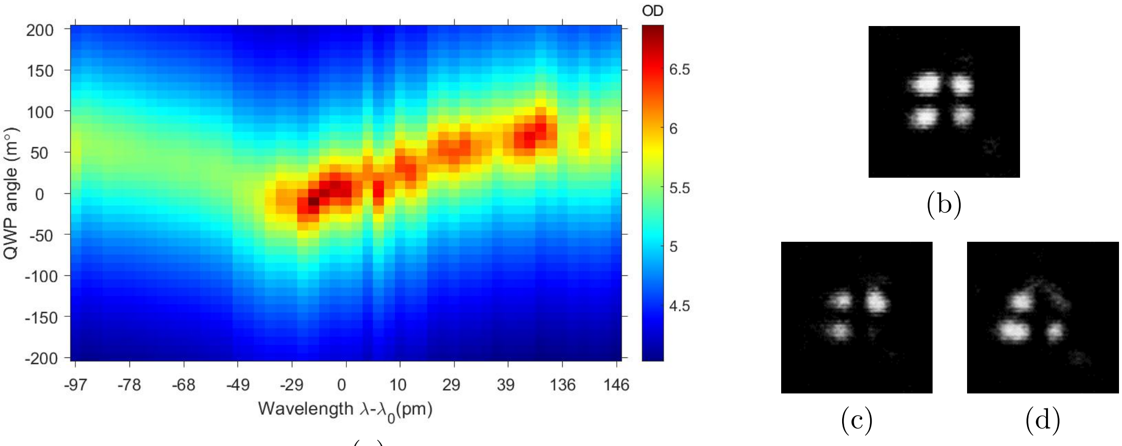

(a)

(b)

(c)

(d)

Figure 2.10: (a) Intensity map of optical density as the laser is tuned around the wavelength $\lambda_0 = 929.0843$ nm. (b) Image of the clover-leaf pattern when the setup is optimized for the rejection of laser at λ_0. (c) and (d) Images of the clover-leaf pattern when laser wavelength is changed while all the elements of the setup are fixed.

sample. We ultimately opted for measuring resonance Raman scattering rather than resonance fluorescence.

2.2.7 Theoretical model

To better understand and analyze the experimental setup and the observed laser extinction, we have developed a simple theoretical model based on the Jones-matrix formalism. We assume here that the excitation laser is initially horizontally polarized and that it can be described with a Jones vector $E_H = \begin{bmatrix} 1 \\ 0 \end{bmatrix}$. Each element of the optical setup in Fig. 2.8a can be described as well in this formalism by a 2×2 Jones matrix. Hence, ideal horizontal and vertical linear polarizers can be expressed by

$$P_H = \begin{bmatrix} 1 & 0 \\ 0 & 0 \end{bmatrix}, P_V = \begin{bmatrix} 0 & 0 \\ 0 & 1 \end{bmatrix} \tag{2.3}$$

The polarizing beam splitter needs to be represented with two separate matrices for the excitation and detection arms of setup. When the excitation laser passes through the PBS1 for the first time, the horizontally polarized light is transmitted through it. This is described by the matrix PBS_{H_0}, where $t = \sqrt{0.001}$ corresponds to the residual vertical polarization which is transmitted since the PBS does not offer perfect extinction. Similarly, after the reflection from sample the detection beam will be reflected on PBS1 and sent in the detection arm. In this case, PBS is represented by the matrix PBS_{V_0}, where $r = \sqrt{0.02}$ corresponds to the horizontal polarization in the reflected beam. The values of t and r coefficients are obtained from Thorlabs specifications for this PBS.

$$PBS_{H_0} = \begin{bmatrix} 1 & 0 \\ 0 & t \end{bmatrix}, PBS_{V_0} = \begin{bmatrix} r & 0 \\ 0 & 1 \end{bmatrix} \tag{2.4}$$

To model the additional imperfections of the PBS, we introduce a new matrix L. Similarly as in Ref. [85], this matrix describes the polarization imperfection and is represented by

$$L = \begin{bmatrix} \sqrt{1-\eta^2} & i\eta \\ i\eta & \sqrt{1-\eta^2} \end{bmatrix} \tag{2.5}$$

The elements of this matrix are selected to ensure that it is unitary. This matrix acts as a wave plate with a slight retardance denoted as η, and its eigenaxes are oriented 45° off from the polarizer axis. Consequently, it converts linear polarization into a slightly elliptical one. The PBS is then defined as $PBS_H = L \cdot PBS_{H_0}$ and $PBS_V = L \cdot PBS_{V_0}$.

The quarter-wave plate is defined in the polarization basis of its eigenaxes by the standard matrix for a phase retarder in Jones formalism:

$$QWP = \begin{bmatrix} e^{i\,ret\,\pi} & 0 \\ 0 & e^{-i\,ret\,\pi} \end{bmatrix} \tag{2.6}$$

where ret is the retardance of the plate. For a perfect QWP $ret = 0.25$. However, according to the specifications for the QWP used in our setup, this retardance is $ret = 0.26$. In our experiment, the QWP can also be rotated by the angle α, which can be written as $QWP'(\alpha) = R(-\alpha)QWPR(\alpha)$, where the rotation matrix $R(\varphi)$ is defined as:

$$R(\varphi) = \begin{bmatrix} \cos(\varphi) & \sin(\varphi) \\ -\sin(\varphi) & \cos(\varphi) \end{bmatrix} \tag{2.7}$$

Having defined all the relevant elements of the setup, we can now write the optical field amplitude after the analyzer (P2 in Fig. 2.8a) as

$$\boldsymbol{E} = P'_V(\theta)PBS_V QWP'(\alpha)QWP'(\alpha)PBS_H P_H E_H \tag{2.8}$$

The QWP' is used in this equation twice since the beam passes two times through this optical element. It should also be noted that it is assumed that the first polarizer is fixed at 0° angle, while the analyzer can be rotated by the angle θ to improve the laser extinction, as was the case in our experiment. Matrix for the rotated analyzer is defined as $P'_V(\theta) = R(-\theta)P_V R(\theta)$. The intensity of the collected light after the analyzer is proportional to $I = \boldsymbol{E}^\dagger \cdot \boldsymbol{E}$. The rotation angles of QWP and analyzer (α and θ, respectively) will be taken as two parameters to optimize in this calculation. The only other parameter that we should define is η in L matrix. This parameter depends on the properties of PBS. Based on the available experimental measurements, it is not possible to precisely determine the numerical value of this parameter. The value of η has been approximated to broadly replicate our observations, and for this purpose, we set η to 10^{-5}.

The intensity of the detected light calculated in this way is presented in Fig. 2.11a. The points in this intensity plot for which OD>4 form a very characteristic shape, while for the rest of the plot, optical density is very low (OD<2). When we zoom in on the central part of the graph (Fig. 2.11b), it becomes evident that the maximum optical density (OD>7) is achieved when both α and θ are close to zero. As the angles α and θ increase, the optical density gradually decreases. Assuming that the QWP is ideal and thus using a retardance value of $ret = 0.25$ in this calculation, we would not observe this decrease in OD. Along this curve, laser extinction would correspond to OD> 7. In other words, for any QWP angle it would be possible to find an analyzer angle for which OD would be maximal. However, this does not align with our experimental observations, which indeed confirms that the QWP in our optical setup is not ideal and for the retardance we should take the value 0.26 as per specifications.

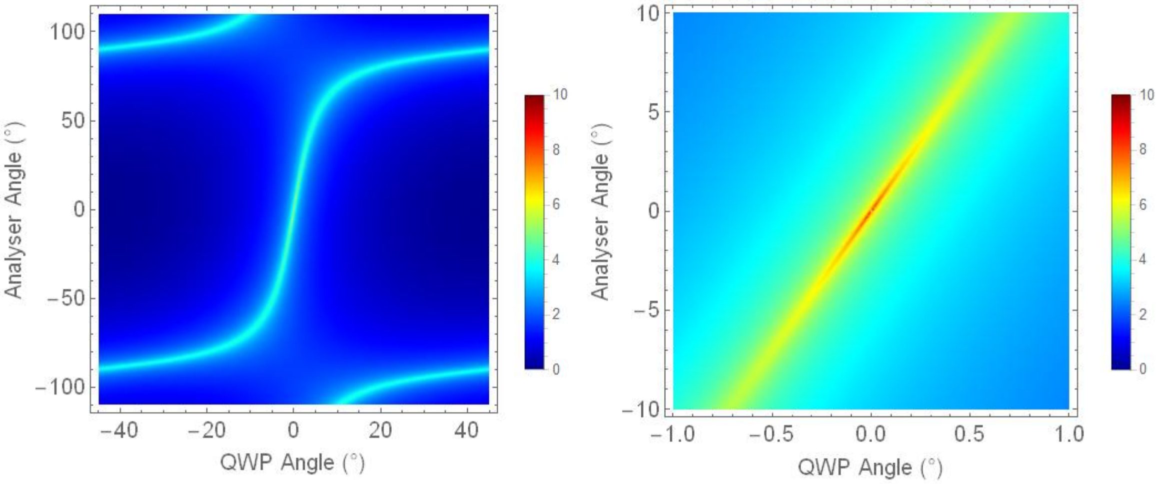

(a) (b)

Figure 2.11: (a) Intensity map of simulated optical density as a function of both QWP angle (α) and analyzer angle (θ). (b) Zooming in on the central part of this intensity map, it can be seen that OD> 7 is achieved near the origin and that OD quickly decreases with the increase of angles α and θ.

In Fig. 2.11b, it is also evident that, near the maximal optical density, the OD value is approximately ten times more sensitive to changes in the QWP angle compared to changes in the analyzer angle. To analyze this more closely, we generated plots of OD as a function of the analyzer angle for different fixed QWP angles (Fig. 2.12a). The QWP angles α range from $-0.14°$ to $0.14°$ in steps of $0.02°$. Notably, the optimal laser extinction (OD> 10) is achieved at a QWP angle of $\alpha = 0°$. A small change of only $0.02°$ in the α angle results in a two orders of magnitude reduction in OD. Similarly, for fixed analyzer angles, we plotted OD as a function of the QWP angle (Fig. 2.12b). The analyzer angles θ range from $-1.4°$ to $1.4°$ in steps of $0.2°$. The best laser extinction is achieved at an analyzer angle of $\theta = 0°$. A similar trend of OD decrease is once again observed, with a $0.2°$ change in the angle θ resulting in a roughly 1.5 orders of magnitude reduction in OD. This shows as well that OD is approximately ten times more sensitive to changes in the QWP angle. Therefore, a m° precision control is indeed necessary for the QWP. This aligns with our experimental observations and affirms the requirement for a motorized rotary stage for precise QWP control. Conversely, manual rotation of the analyzer was sufficient to achieve OD> 7.

We can now reevaluate the assumed value for the constant η in the matrix that defines polarization imperfections. This parameter influences the maximal OD and its position. When $\eta < 10^{-6}$, the optical density exceeding 12 is achieved at $\alpha = 0°$ and $\theta = 0°$. For the value used in these simulations ($\eta = 10^{-5}$), the maximum OD is 10.1 at $\alpha = 0°$ and $\theta = 0°$. As η increases ($\eta > 10^{-5}$), the position of maximum OD

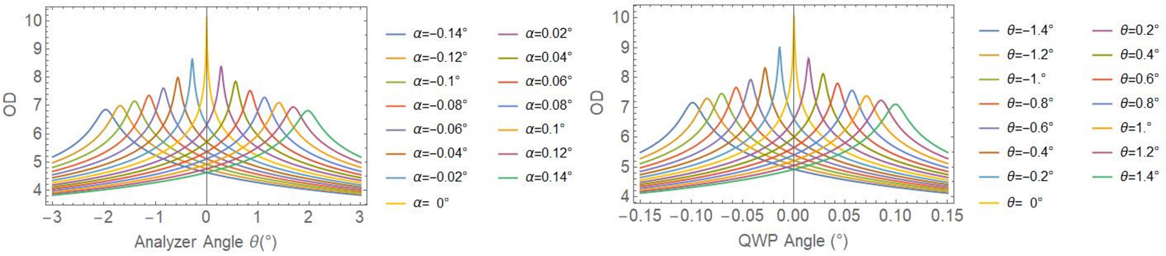

(a) (b)

Figure 2.12: Simulated optical density curves plot (a) as a function of analyzer angle for different fixed QWP angles α or (b) as a function of QWP angle for different fixed analyzer angles θ. The fixed angles α and θ are indicated in the legend of each graph.

shifts toward more negative α and θ angles. However, with increasing η, the OD value remains relatively constant, around OD$\approx$ 10. For larger η ($\eta > 10^{-2}$), OD remains approximately 10, but this maximum is observed at significant analyzer angles, such as $\theta = -41.2°$ for $\eta = 10^{-2}$. This does not align with our experimental observations, where we recorded the highest OD for QWP and P2 positions close to their optical axis. Therefore, the parameter η should be $\eta < 10^{-4}$. However, without additional experimental data, we can't precisely determine the value of η. Using $\eta = 10^{-5}$ allows us to perform this calculation and discuss the experimental results within the context of this model.

The maximum OD value in these calculations is OD$>$ 10, whereas the best OD we have experimentally recorded is OD$=$ 7.5 (Fig. 2.9a). This discrepancy may be attributed to several unaccounted-for factors in this model. Firstly, the matrix L is assumed to be unitary, which means that it does not represent something irreversible. Moreover, as seen in previous sections to achieve OD$>$ 4, eliminating the clover effect is essential. This can be challenging due to different factors such as vibrations, scattered light from the sample back, imperfect alignment that causes beam distortion. In addition to these effects, it can be seen from the calculation that a very precise control of angles α and θ is needed. In fact, it could be challenging to manually control with enough precision the analyzer angle, resulting in difficulty in finding the exact combination of α and θ angle, and thus maximal extinction. Nevertheless, this theoretical model, although very simple, gives a rough idea about the OD dependence on the QWP and analyzer angles, which is observed experimentally.

2.3 Resonant excitation of Mn-doped InGaAs QD transitions

2.3.1 Positive trion formation in Schottky diode sample

To test the constructed setup (Fig. 2.8a) in resonant excitation experiments, we first used a sample containing Mn-doped InGaAs quantum dots embedded in a n-i-Schottky diode. The QD charge state is controlled by applying the bias V_g between the Schottky and ohmic contact, as described in section 1.1.4. In this experiment, we focus on the positive trion X^+ charge state in the QD1. To create a positive trion X^+, we use a non-resonant laser at higher energy than QD transition (Ti:Sapphire laser at $E = 1.326eV$), which generates an electron-hole pair in the quantum dot (Fig. 2.13a). The strong electrical field causes the electron to tunnel out of the QD, whereas the hole remains in the QD due to its larger effective mass. The remaining hole combined with a second electron-hole pair forms the positive trion X^+ (Fig. 2.13b). This highlights the importance of intra-dot excitation since the applied gate voltage V_g alone cannot create a hole in the QD [51, 55].

We then studied the photoluminescence spectra of the Mn-doped InAs QD1 under intra-dot (p-shell) excitation as a function of applied gate voltage. The resulting data is presented in Fig. 2.13c. For $V_g > 70$ mV, we observe the lines corresponding to the neutral exciton X^0 state. When the gate voltage is below 0.7 V, we see a group of lines blue-shifted by 8 meV, corresponding to the positive trion state X^+ generated as explained above. In contrast to the single PL line observed for each trion state in undoped InGaAs QD shown in Fig. 1.5, a Mn-doped QD displays a distinctive spectral feature consisting of at least two equidistant PL doublets as explained in Chapter 1.

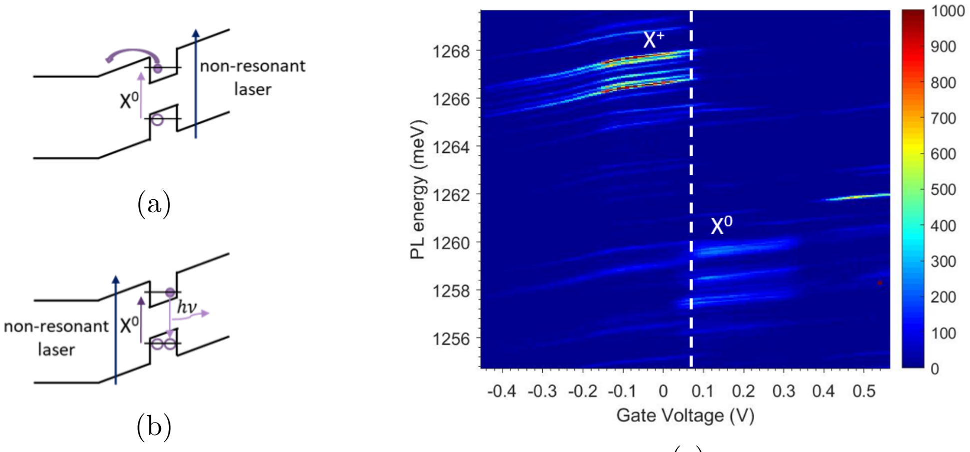

(c)

Figure 2.13: Formation of positive trion X^+ in the quantum dot. The process involves two steps: (a) intra-dot excitation leading to the creation of a hole, and (b) generation of the second electron-hole pair, which along with the hole, forms X^+ trion. (c) Photoluminescence spectra for the Mn-doped QD1 at T= 2 K as a function of applied gate voltage V_g for intra-dot excitation at 1.326 eV.

2.3.2 Resonant optical pumping experiment

We chose the Mn-doped quantum dot (QD1) shown in Figure 2.13c for our first resonant excitation measurements. The spectrum of X^+ for this quantum dot was taken under non-resonant excitation with Ti:Sapphire at $E = 1.326$ eV and V_g=50 mV, and the resulting data is presented in Fig. 2.14. The same kind of spectrum consisting of doublets is observed as in section 1.2.1. For this specific QD, the anti-ferromagnetic (AFM) and ferromagnetic (FM) doublets are separated by the energy $\Delta = 1.304$ meV. The splitting δ equal to 0.153 meV corresponds to the splitting of the two excited states of $X^+ - A^0$. The third doublet observed 1.207 meV below AFM doublet corresponds to the transitions from excited states $X^+ - A^0$ to the level O, as described in Chapter 1.

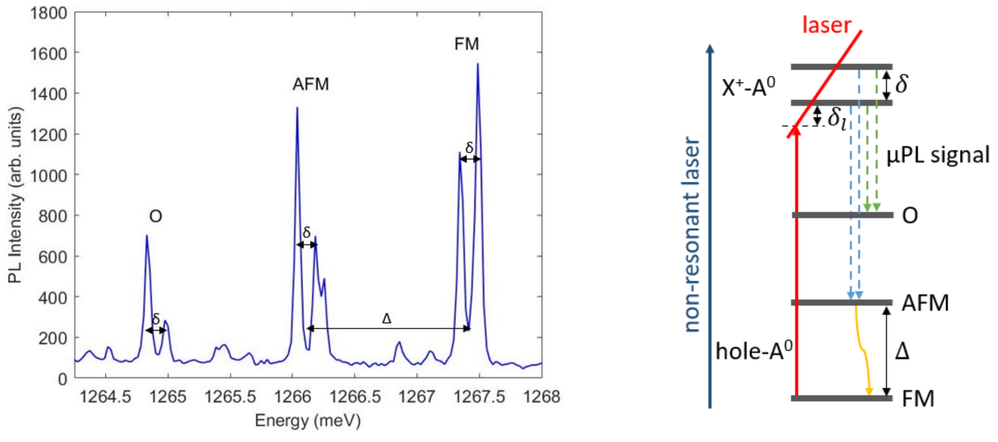

(a)

(b)

Figure 2.14: (a) PL spectrum of the positive trion X^+ state in a Mn-doped InGaAs QD (QD1) for non-resonant optical excitation at 1.326 eV and gate voltage $V_g = 50$ mV. (b) Schematic representation of the levels involved in the transitions from $X^+ - A^0$ to the hole$-A^0$ state. The non-resonant laser excitation (blue arrow) and the laser used for resonant excitation (red arrow) are indicated, as well as the emitted µPL signal (dashed arrows).

A diagram of the energy levels involved in the transitions resulting in these doublets is shown in Fig. 2.14b. In addition to the energy levels of the X^+ state, this schematic shows the non-resonant and resonant lasers, as well as the measured µPL signal. The non-resonant laser (Ti:Sapphire at $E = 1.326$ eV, power $P = 65$ µW) is used for the intra-dot excitation and the creation of a hole in QD, as explained above. In addition to this laser, a second laser (Toptica DLPro with power $P = 40$ µW) is positioned at the energy of X^0 trion state and contributes to the creation of a hole in the QD. A third laser (Toptica DLCpro) is used for resonant excitation of transitions from the FM level to two levels of the $X^+ - A^0$ excited state. This laser is scanning the range of energies around the FM doublet and its detuning from the lower energy transition of the FM doublet is defined as δ_l in Fig. 2.14b.

In spite of our attempts, we were not able to evidence strict resonance fluorescence. The collected PL signal was likely still significantly lower than the shot noise of the reflected laser intensity, despite achieving excellent cross-polarized extinction with our setup. To understand the reason for this, we can calculate the expected PL signal, considering the QD properties (such as 1 ns lifetime, oscillator strength shared by about four lines) and setup characteristics (percentage of collected PL signal in the first lens of 0.64 NA should amount to 1.5%). By additionally taking into account the polarization selection (0.5 factor), the fiber coupling efficiency (~0.5 factor), and a reduction of the PL signal at resonance due to significant inhomogeneous broadening by a factor of approximately 20, as will be detailed in Chapter 4, the estimated PL count rate collected by the SM fiber, for a QD1 line at saturation, should amount to $\approx 4 \cdot 10^4 \mathrm{s}^{-1}$. For shot noise estimation, we can assume a laser power of 1 µW (corresponding to the saturation power for these QDs, as it will be shown in Chapter 4) which is attenuated by the optical density of our setup. Taking OD=6, after considering the possible decrease in OD as the laser scans wavelengths around the QD transition, results in a shot noise value estimated to be $\approx 10^3$. Therefore, for an acquisition time of 1 s, the PL signal should have been about 40 times stronger than shot noise and therefore detectable. However, in our measurements, even with increased acquisition time, we were unable to extract a resonance fluorescence signal. This limitation could be attributed to QD blinking effect (as QD charge fluctuation), leading to a reduced effective number of fluorescence photons, or to instabilities of the setup extinction during a scan, leading to a much larger effective noise on the reflected laser signal. Solutions to reach the resonance regime could be to use a solid immersion lens, as demonstrated in Ref. [29], or to fabricate a QD sample with an optical cavity. Both approaches would enhance the light-matter interaction and aid in the more efficient extraction of photons from the high-refractive-index semiconductor, however they suffer from inherent difficulties in the case of Mn-doped QDs because of their rarety and broadband spectrum.

Nevertheless, we were able to overcome this issue in a different way, namely by using the unique transitions of these Mn-doped InGaAs QDs, allowing us to measure the signal of the AFM doublet when the FM doublet is resonantly excited thanks to the spectral shift of about 1.3 meV, as depicted in Fig. 2.14b. This different approach for carrying out coherent spectroscopy corresponds to the regime of resonance Raman scattering. Thus, photons emitted as a result of transitions from levels of $X^+ - A^0$ state to O and AFM final states can be detected without being blinded by the laser. A series of such µPL spectra is presented in the form of intensity map in Fig. 2.15. Our dark-field microscopy setup along with spectral resolution was thus able to sufficiently reject the reflected light from the resonant laser, allowing us to measure the PL signal for the AFM and O doublets. The remaining laser line is not visible in this intensity map because it is situated higher in energy than the plotted range.

When the laser is resonant with the transition from FM levels to the first ($\delta_l = 0$) or second level ($\delta_l = 153$ µeV) of $X^+ - A^0$ state, we observe an increase of the intensity for the transition from the resonantly addressed $X^+ - A^0$ level to the AFM and O levels. For the power of the resonant laser used in this measurement ($P = 80$ µW), the resonance linewidth is about 34 µeV. This linewidth is significantly broader than the expected natural linewidth of InAs QDs (~ 1.5 µeV). This effect cannot be solely attributed to power broadening, as will be demonstrated in a power dependence study conducted on a different sample presented in Chapter 4. It will be shown there that the reason for this line broadening is inhomogeneous broadening originating from spectral diffusion. Spectral diffusion in case of our QDs can be viewed as a rigid shift of two excited states with respect to FM and AFM levels, which is then reflected in the same shift in emission. In addition to this, we also observe diagonal lines between the peaks in the AFM and O doublet. This line is particularly noticeable for the AFM doublet. It represents the Stokes Raman line, which is a line shifted below the laser energy by the ground state splitting (Δ). This kind of Raman emission was already observed in the case of resonant excitation of a quantum dot molecule in a cavity by Vora et al. [86].

At the time of this first experiment, we were not able to study the dependence of the resonance linewidth and Raman line on the power of the resonant laser over a wide range. Resonant excitation with very low laser powers posed difficulties due to the low PL signal collected from QD emission. Conversely, high laser powers presented a challenge in terms of laser extinction, even with the dark-field microscope setup. The issue of reflected light from high-power lasers was subsequently resolved during the course of my thesis by operating the double spectrometer in a true Raman mode to more efficiently filter out the stray light from the PL spectrum of interest. This development allowed for the clear observation of dressed states in a different QD sample, which will be discussed in Chapter 4. However, for the experiments done on the current Schottky diode sample, we were not able to evidence AC Stark effect or Autler-Townes effect due to the presented limitations in measurements. Nevertheless, the AC Stark effect is expected to be observed in this type of QDs. Dressed states resulting from the interaction of an exciton state with a single strong resonant laser have been reported in undoped III-V (InGaAs) [87] and Mn-doped II-VI (CdTe) [12] quantum dots.

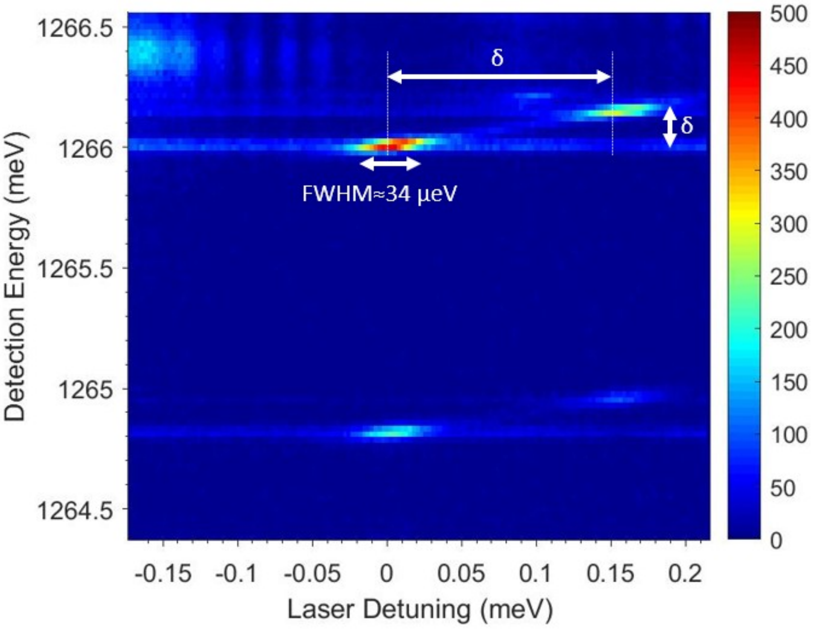

Figure 2.15: Intensity map of µPL emission as a function of laser and detection energy. The doublets presented in this map are AFM and O doublets while the laser is scanning through higher energy FM doublet, which is not shown in this map. Splitting δ between the two peaks of a doublet is indicated, as well as the resonance linewidth ($\approx$ 34 µeV).

2.3.3 Theoretical model and estimation of the anti-ferromagnetic spin relaxation time

As we were unable to measure the Rabi splitting of the X^+ trion when dressed with a strong resonant laser or study its dependence on laser power, this presents a limitation in creating a more comprehensive theoretical model to describe this quantum dot and the measurement depicted in Fig. 2.15. Therefore, we started by implementing a simple theoretical model based on rate equations for a two-level atomic system. Schematic representation of levels used in this model is shown in Fig. 2.16a. AFM and FM levels of ground state are labeled as level $|2\rangle$ and $|4\rangle$, respectively, while the levels of excited state are labeled as level $|1\rangle$ and $|3\rangle$. The level corresponding to the orthogonal spin configuration (level O in Fig. 2.14b) is not considered in this simple theoretical model. Similar to the case of a two-level atom [88], the rate equations describing the change of population of levels $|3\rangle$, $|1\rangle$ and $|4\rangle$ (Fig. 2.16a) in the steady-state regime can be written as:

$$\begin{gathered}
\frac{n_2+n_4}{\tau_{nl}} + \frac{n_2-n_3}{\tau_{res23}} - \frac{n_3}{\eta_{34}\tau_r} - \frac{n_3}{\eta_{23}\tau_r} = 0 \\
\frac{n_2+n_4}{\tau_{nl}} + \frac{n_2-n_1}{\tau_{res21}} - \frac{n_1}{\eta_{12}\tau_r} - \frac{n_1}{\eta_{14}\tau_r} = 0 \\
\frac{n_3}{\eta_{34}\tau_r} + \frac{n_1}{\eta_{14}\tau_r} - \frac{2n_4}{\tau_{nl}} - \frac{n_4}{\tau_s} = 0
\end{gathered} \tag{2.9}$$

In the first equation depicting the contributions to the population of level $|3\rangle$ of excited state, the first term describes the absorption from ground state levels $|2\rangle$ and $|4\rangle$ due to the non-resonant laser excitation, where τ_{nr} is a time related to this process. The same term appears as well in the second equation describing the population change of level $|1\rangle$. The second term corresponds to the stimulated absorption (n_2/τ_{res23}) and emission ($-n_3/\tau_{res23}$) due to the resonant laser excitation of the $|2\rangle \rightarrow |3\rangle$ transition. Similarly, the second term in the second equation describes the resonant excitation of the $|2\rangle \rightarrow |1\rangle$ transition. The times τ_{res23} and τ_{res21} that describe these processes are given by:

$$\begin{aligned}
\tau_{res21} &= \eta_{12}\tau_{res}\left(1+\frac{4(\delta_l-\delta_{21})^2}{\Gamma_{21}^2}\right) \\
\tau_{res23} &= \eta_{23}\tau_{res}\left(1+\frac{4(\delta_l-\delta_{23})^2}{\Gamma_{23}^2}\right)
\end{aligned} \tag{2.10}$$

where the term in the bracket describes the resonant nature of these process described here by a Lorentzian profile. Here δ_l is the detuning of the resonant laser from level $|1\rangle$, and $\delta_{21} = 0$ µeV and $\delta_{23} = 153$ µeV correspond to the situations when transition $|2\rangle \rightarrow |1\rangle$ and $|2\rangle \rightarrow |3\rangle$ are resonantly excited, respectively. Γ_{21} and Γ_{23} are the full width at half maximum (FWHM) of these Lorentzian curves.

The third and fourth terms in the first two equations in Eq. 2.10 correspond to the natural radiative decay from excited state to the ground state levels $|2\rangle$ and $|4\rangle$. The decay time from level $|3\rangle$ to level $|2\rangle$ is τ_r, adjusted to a value around the typical recombination lifetime in InAs quantum dots, namely $\tau_r = 0.7$ ns. Since the peaks corresponding to the transition from excited state to the ground state levels are of different intensity for this quantum dot (Fig. 2.14a), the related decay times are defined with respect to the τ_r time by introducing the parameters η_{ij} ($\eta_{23} = 1$, $\eta_{12} = 1.42$, $\eta_{34} = 2.33$, $\eta_{14} = 1.17$). The parameters η_{12} and η_{23} are used in Eq. 2.10 as well to model the different coupling strengths of resonant laser for the transitions $|2\rangle$ and $|1\rangle$ and $|2\rangle$ and $|3\rangle$.

Lastly, the third equation in Eq. 2.9 describes the change of population for level $|4\rangle$. The first two terms represent the contribution due to the decay from the excited states $|3\rangle$ and $|1\rangle$. The third term corresponds to the reduction in population because of the stimulated absorption and transition to the excited states $|3\rangle$ and $|1\rangle$ due to the non-resonant laser. Finally, the relaxation from level $|4\rangle$ to $|2\rangle$ is described by the last term, where τ_s represents the AFM spin relaxation time.

In addition to these three equations, our closed system model imposes conservation of the total populations which leads to the equation:

$$n_1 + n_2 + n_3 + n_4 = 1 \tag{2.11}$$

This set of equations can now be numerically solved to model the experimental data from the resonant optical pumping experiment (Fig. 2.15).

From the data of this experiment, we have extracted the PL intensity of the $|1\rangle \rightarrow |4\rangle$ transition (pink points in Fig. 2.16b) and the $|3\rangle \rightarrow |4\rangle$ transition (blue points). These PL intensities have been normalized to the maximum value of $|1\rangle \rightarrow |4\rangle$ transition. A closer examination of these integrated intensities reveals that when a level $|1\rangle$ is resonantly excited, an increase in the signal is observed for the transition $|1\rangle \rightarrow |4\rangle$, while simultaneously, a decrease is observed for the transition $|3\rangle \rightarrow |4\rangle$. This occurs because the resonant laser promotes the excitation of electrons to level $|1\rangle$, leading to an increase in the population of this level. Consequently, the number of electrons available for excitation to level $|3\rangle$ is reduced, resulting in a decrease in its population. A similar situation is observed for the resonant excitation of the $|3\rangle \rightarrow |4\rangle$ transition. The dips in the data are particularly pronounced for this QD, which implies, within the present model, a very short relaxation time τ_s. This feature is taken into consideration when attempting to replicate the experimental results using the model.

By fitting the parameters of the model, we obtain curves for normalized population n_1 and n_3 (pink and blue curves in Fig. 2.16b). The parameters were manually adjusted to achieve a good agreement with experimental data. Using this simple rate equation model and the measurement conducted for a single resonant laser power, determining the exact values of the parameters is challenging. The time related to non-resonant laser excitation is set to $\tau_{nr} = 13$ ns. To reproduce the signal intensity and dips, it was necessary to choose relatively small values for resonant excitation and spin relaxation time ($\tau_{res} = 0.75$ ns and $\tau_s = 0.75$ ns). This relaxation time depends on the QD and its splitting Δ, as will be demonstrated in section 4.2.3. The spin relaxation times observed in the samples studied in this thesis are in the nanosecond range, which is in agreement with short spin relaxation time ($\simeq$20 ns) observed for a single Mn atom in II-VI QD, as reported in Ref. [89].

The resonance linewidths in this model are defined by the FWHM of Lorentzians in Eq. 2.10 for resonant excitation. The values taken for these fits are $\Gamma_{21} = 26$ µeV and $\Gamma_{23} = 35$ µeV. However, this simple model does not account for inhomogeneous broadening, which certainly has a significant impact on the resonance linewidth of our QDs. A more detailed discussion of these relative contributions will be provided in Chapter 4 when a model based on optical Bloch equations will be developed.

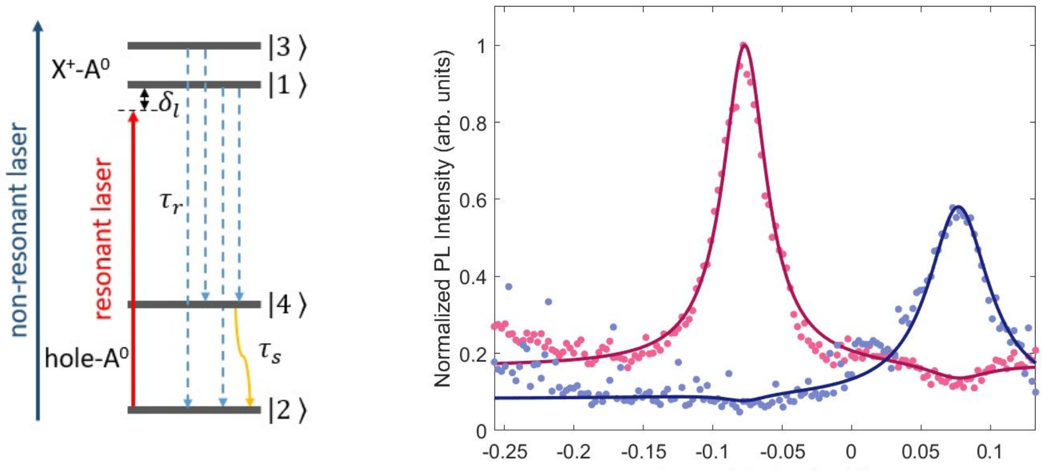

(a)

(b)

Figure 2.16: (a) Schematic representation of the ground state ($|2\rangle$ and $|4\rangle$) and excited state levels ($|1\rangle$ and $|3\rangle$) described with the theoretical model. The non-resonant (blue arrow) and resonant lasers (red arrow) are indicated, as well as the natural decay (dashed arrows) and spin relaxation (yellow arrow) processes. (b) The PL intensity of the $|1\rangle \rightarrow |4\rangle$ transition (pink points) and the $|3\rangle \rightarrow |4\rangle$ transition (blue points) are fitted with the populations n_1 (pink curve) and n_3 (blue curve) obtained from the rate equations. Both transitions have been normalized to the own maximum value of n_1.

2.3.4 Summary

In this chapter, we implemented a dark-field confocal microscope setup. We observed the clover-leaf pattern and discussed its origin in both experiments and simulations. We examined and explained the significance of utilizing optical components such as a polarizer, analyzer, polarizing beam splitter, quarter-wave plate, and collection fiber through both experimental results and a theoretical model. The setup we created efficiently filters out reflected laser light, and we achieved laser extinction levels that were near state-of-the-art (as of 2020) with OD$>$ 7 [29]. Despite the high performance of this setup, measuring resonance fluorescence for Mn-doped QDs in the sample without a solid-immersion lens or cavity structure proved to be challenging. Even with an estimated PL signal around 40 times higher than the residual laser shot noise, it was not resolved, possibly due to the presence of QD blinking or OD instabilities. Nevertheless, the stability of the setup over time and across a range of wavelengths suitable for resonant scanning of QD transitions (typically 100-200 pm) is adequate for conducting resonance Raman scattering measurements on Mn-doped InGaAs QDs, thanks to the Λ-like system of transitions, enabling detection approximately about 1 meV below the excitation energy.

We first tested the setup for QD1 in a Schottky diode sample, which allows the control of QD charge state. This QD is charged with a single hole and the PL signals for the transitions from $X^+ - A^0$ excited states to the hole$-A^0$ ground states are measured. These transitions are also excited with the scanning resonant laser. The observed resonance linewidth is significantly broader than the natural linewidth of

InAs QDs, indicating that spectral diffusion is likely present. This will be analyzed in more details in the Chapter 4, which will help us gain a better understanding of these Mn-doped QDs. In this chapter, we fitted the experimental data with a simple model based on rate equations for the populations. The numerical solutions that best fit the experimental data suggest that the spin relaxation time of the AFM level toward the FM level is very short for this QD ($\tau_s = 0.75$ ns), but consistent with the spin dynamics of Mn atom reported in [89].

To gain a better understanding of the origin of the broad resonance linewidth, we decided to conduct similar measurements on QDs in a sample without Schottky diode where a large dark current was actually present. However, we started this investigation with a particular sample that had previously undergone hydrogenation. This process resulted in bonding of hydrogen with neighboring As atoms of Mn dopant, preventing the formation of the acceptor state A^0 and resulting in the compensated Mn dopant. Consequently, these QDs exhibit a very distinct optical signature, which will be thoroughly investigated in Chapter 3.

Following the annealing of this sample, the neutral acceptor A^0 configuration was restored, leading to a spectrum similar to that of QD1. Due to the limitations of the setup during the measurements for QD1, we did not excite QD1 with a high-power resonant laser to observe the AC Stark and Autler-Townes effects. However, by operating our double spectrometer in true Raman mode for additional filtering of scattered laser light and improving the collected signal from the QD, it became possible to study the resonant excitation of QD transitions over a broad range of laser powers. We conducted such a study on a QD in the annealed sample without Schottky contacts, and we will present it in Chapter 4. With more data for a range of resonant laser powers and through the pump and probe experiment, it was possible to create a more sophisticated model based on the optical Bloch equation. This will provide us with more information about the origin of the broad resonance linewidth and the Autler-Townes effect. Moreover, in Chapter 4, we will revise the rate equations model adopted here and apply the new model to QD1.

Chapter 3

Optical signature of a single H-passivated Mn dopant

In the previous chapter, we observed that the first resonant excitation measurements of the Mn-doped quantum dot showed a resonance linewidth much larger (34 µeV) than the natural linewidth of InGaAs QDs. Initially, we suspected that this behavior could be linked to spectral diffusion due to the large dark current in the contacted diode used in this study. Consequently, we first opted to make contacts on a few other Schottky diodes within the same region of the sample. We specifically selected diodes with smaller reverse leakage currents to minimize their possible impact on spectral diffusion. However, we were unable to locate Mn-doped QDs in these newly contacted diodes to conduct resonant excitation experiment. Since this attempt turned out to be unsuccessful, we decided to investigate the origin of the broad resonance linewidth by conducting the same type of measurements on a sample of Mn-doped InGaAs QDs without a Schottky diode. However, the piece of sample we took had likely been hydrogenated in the past to carry out a study on the possible compensation of the Mn-induced acceptor state. Indeed, hydrogenation had been successfully used as a passivation technique of GaMnAs layers to tune the density of carriers (holes) by forming electrically inactive (Mn,H) complexes, as demonstrated in Ref. [90, 91]. This process allowed control of ferromagnetic properties of GaMnAs layers. Similarly, hydrogenation had been applied to our InGaAs QD sample in an attempt to transform the neutral acceptor state of Mn into an isoelectronic center as in II-VI QDs. At the time, this investigation had not been successful. A few years later, when we started measuring it again, we observed very distinct spectral features compared to those observed so far for Mn-doped InAs QDs. This prompted us to conduct a separate side study of such hydrogenated Mn-dope QD, which is presented in this chapter.

Transition metal atoms, such as Mn, do not incorporate easily into III-V semiconductors. This results in Mn atoms acting as shallow acceptors, consisting of a magnetic center and a highly localized hole. Due to the presence of this hole, the Mn dopant state exhibits strong sensitivity to strain, particularly when compared to Mn-doped II-VI quantum dots. As mentioned above, hydrogen passivation had been performed on this sample in the past with the idea of preventing the formation of this acceptor state by allowing one of the neighboring As atoms to bond with the introduced H atom. The observed optical characteristics of the H-passivated Mn atom are presented in section 3.1. They consists of a complex set of lines that exhibit unconventional evolution in response to a longitudinal magnetic field, distinctly differing from the signature observed in II-VI QDs [1–3, 68]. In section 3.2, we describe the theoretical model utilized to comprehend this finding, relying on a single particle spin Hamiltonian for the H-passivated Mn dopant. This dopant is treated as a 5/2 spin system submitted to a significant crystal field resulting from the symmetry disruption of the As-H bond. The good qualitative agreement between the simulation obtained with this theoretical model and the experimental observations is presented in section 3.3. Furthermore, the validity of the created model is confirmed through resonant optical excitation of different levels of this QD (QD2), with results presented in section 3.4. Lastly, we performed soft annealing of this sample, leading to the dehydrogenation of the quantum dots. The typical optical signature of Mn-doped InAs QDs was restored for QDs found in the area of the sample where the hydrogenated QD2 was observed. These spectral results are presented in section 3.5, along with the theoretical simulations obtained using the model describing the Mn acceptor introduced in section 1.2.3.

3.1 Spectral characteristics of hydrogenated magnetic quantum dot

The sample utilized in these experiments consists of a layer of Mn-doped InGaAs quantum dots, which, unlike the previous case, is not embedded in a Schottky diode. Additionally, this sample has undergone prior hydrogenation. Similar to the diode sample discussed in section 2.3.1, we first utilize non-resonant laser excitation to observe the spectra of single Mn-doped quantum dots. A He-Ne laser ($E = 1.95$ eV) is used to stabilize electrical environment of the QD, notably to positively charge the QD with a resident hole and thus form a postive X^+ trion under excitation with a Ti-Sapphire laser ($E \approx 1.42$ eV). Figure 3.1a illustrates the signature of one of the Mn-doped QDs studied in this sample (QD2). It actually displays two sets of lines corresponding to different charge states. The intensity of one set of lines is stronger depending on the power and focusing of the He-Ne laser. It was also noted that the lines at higher energy exhibit a high degree of polarization when excited by σ^- polarized light and detected with σ^+ or σ^- polarization. This suggests that the lines at higher energy correspond to a charged exciton state. Since the negative trion X^- lies at lower energies than the neutral exciton X^0, which is not the case here, we can conclude that the two observed states correspond to X^0 and X^+. Furthermore, a theoretical model applied to this QD confirms that the excitonic complex showing up at higher energy is most likely X^+. In this sample of Mn-doped QDs, we generally observe a strong signal for X^+ trions, which is the trion state we will focus on in the rest of this thesis.

The PL spectrum of an another hydrogenated Mn-doped QD (QD3) obtained for the same non-resonant laser excitation at zero magnetic field is depicted in Fig. 3.1b. The spectra of QD2 and QD3 exhibit multiple prominent peaks, deviating significantly from the usual spectrum characterized by two doublets observed in Mn-doped InGaAs quantum dots. Moreover, we did not manage to find non-passivated Mn-doped QDs in this sample; instead, we observed only QDs exhibiting quite complex PL characteristics. In the case of both QDs in Fig. 3.1, the observed lines are spatially and spectrally correlated, meaning they appear and disappear all at the same time when the laser spot is moved or the laser energy is changed. To further confirm that these peaks originate from the same Mn-doped quantum dot, we apply a longitudinal magnetic field in the Faraday configuration. For QD2 of Fig. 3.1a, a series of spectra is recorded in both σ^+ and σ^- polarizations, covering a magnetic field range from 0 to 7 T with an incremental step of 50 mT. The resulting spectra form a magneto-PL density plot presented in Fig. 3.4a. This plot demonstrates a nonlinear dependence of the line shifts on the magnetic field (in addition to the usual quadratic dependence due to the diamagnetic shift). It also reveals numerous anticrossings, confirming that these lines very likely originate from the same Mn-doped quantum dot. Given that the previously established theoretical model for Mn-doped InGaAs QDs (section 1.2.3) no longer applies to the scenario of H-passivated Mn dopant, a new theoretical model needs to be developed to comprehend the origin of the observed lines. This side task, which is interesting in its own right, was primary thought of as a complementary validation of the developed setup and its suitability for resonant excitation experiments on usual Mn-doped QDs, the main goal of this thesis. Conversely, the resonant excitation measurements presented in this chapter provide a deeper understanding of the energy levels associated with H-passivated Mn-doped QD. The results of this chapter, although on a sidetrack of main objective, offer valuable insights into the solid-state physics that arises from the hydrogenation of Mn-doped InGaAs QDs.

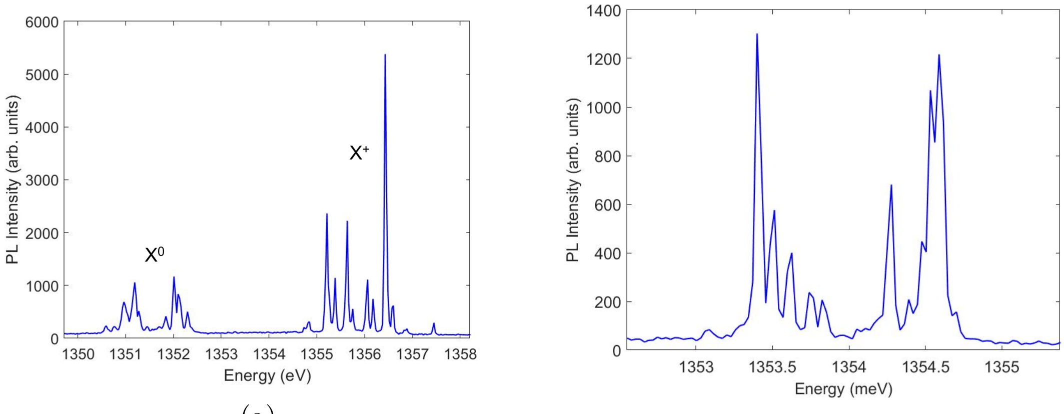

(a)

(b)

Figure 3.1: PL spectrum of the positive trion X^+ state in a H-passivated Mn-doped InGaAs QD at $B_z = 0$ T, obtained under non-resonant optical excitation at 1.42 eV for (a) QD2 and (b) QD3. All the measurements were conducted at T= 2 K.

3.2 Theoretical model of spin Hamiltonian for H-passivated Mn dopant

So far, in the previous two chapters, we have focused solely on single Mn-doped InGaAs QDs. In these QDs, the Mn atom replaces an In or Ga atom in the InGaAs

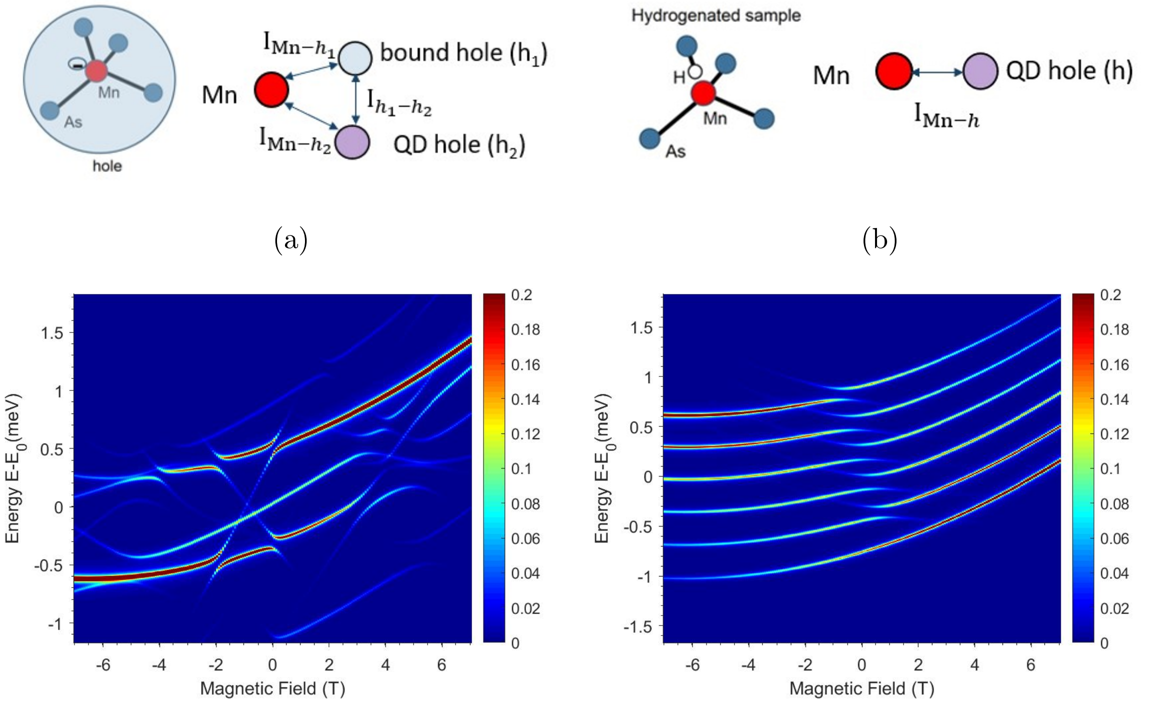

(a) (b)

(c) (d)

Figure 3.2: Schematic representation of an InAs QD doped with a single Mn atom (a) which forms a neutral acceptor state with a bound hole (h_1) and (b) which is passivated with H atom. (c),(d) Theoretical simulation of the PL density plots realized with the model based on A^0 state and a strain-free, symmetrical H-passivated Mn dopant, respectively.

lattice, resulting in the formation of a negatively charged center denoted as A^-. Together with a bound hole (h_1), it forms a neutral acceptor state labelled as A^0. The theoretical model developed for these QDs is based on the spin Hamiltonian describing the involved particles and the exchange interactions between them. When a hole (h_2) is trapped in such QD, forming the $h_2 - A^0$ state, we need to consider the Mn, h_1 and h_2 as particles and account for the exchange interactions among them. This is illustrated in the schematic diagram shown in Fig. 3.2a. The complete model is presented in section 1.2.3, and a typical photoluminescence (PL) density plot obtained using this theoretical model for the positive trion X^+ is displayed in Fig. 3.2c. The features of this plot were extensively discussed in Chapter 1.. However, this model cannot be applied to reproduce the complex characteristics observed in the experimental PL density plot shown in Fig. 3.4a.

To properly model the case where the Mn dopant is passivated by a hydrogen atom, we need to adopt a different description. Upon introducing hydrogen atoms into the semiconductor matrix, a bond between Mn and one of the surrounding As atoms is replaced by an As-H bond, and the negative charge on the Mn site is strongly reduced. Consequently, in this new context, the Mn dopant does not give rise to an acceptor state but instead behaves as an isoelectronic impurity [92]. This is illustrated in Fig. 3.2b. In this case, there is no longer a Mn-bound hole. Our new model for a trion ground state, considers just a single hole (h) trapped in the QD and the Mn atom as particles, still submitted to their exchange interaction. From this new description, we can then employ the same approach for modelling the magneto-PL plots as described in section 1.2.3, by adapting the previous terms in the spin Hamiltonians to the case of the H-passivated Mn dopant.

Since we are considering only Mn and h ($S_{\text{Mn}} = 5/2$, $J_h = 3/2$) for a positively charged QD, we can describe them with the following spin Hamiltonians:

$$\begin{aligned} \hat{H}_{\text{Mn}} &= g_{\text{Mn}}\mu_B \hat{\boldsymbol{S}}_{\text{Mn}} \cdot \boldsymbol{B} + \hat{H}_s \\ \hat{H}_h &= g_h \mu_B \hat{\boldsymbol{J}}_h \cdot \boldsymbol{B} + \hat{H}_{HL} \end{aligned} \tag{3.1}$$

where μ_B is the Bohr magneton and g_{Mn} and g_h are the Landé factors of Mn and trapped hole, respectively. The term $\hat{H}_s$ is still defined in the same way as in the Eq. 1.7, but now it accounts for the anisotropy experienced by the Mn atom (the $3d^5$ electrons) in a strained self-assembled QD. The Hamiltonian $\hat{H}_{HL}$ was also already introduced in the previous model and describes the anisotropy experienced by the QD-trapped hole h, as given in Eq. 1.8. Additionally, we need to consider the exchange interaction between Mn and h, which can be expressed as:

$$\hat{H}_{h-\text{Mn}} = I_{h-\text{Mn}} \hat{\boldsymbol{S}}_{\text{Mn}} \cdot \hat{\boldsymbol{J}}_h + \hat{H}_a \tag{3.2}$$

where $I_{h-\text{Mn}}$ is the exchange energy between these two particles. The anisotropic term $\hat{H}_a$, defined by Eq. 1.10, here also describes the $p-d$ exchange between the off-center Mn and h. It originates from heavy-hole/light-hole band mixing when Mn impurity is off axis, for a cylindrically symmetric QD [75]. This term would vanish for a Mn on the axis of a circularly symmetric QD. It should be noted that, in this model, we consider only the first-order term of this Hamiltonian as defined in [75], which linearly depends on the parameter ρ, while the second-order term ($\sim \rho^2$) is neglected.

When an electron-hole pair is created in the positively charged QD, it results in the formation of positive trion X^+ state. The spin Hamiltonian for an electron ($S_e = 1/2$) can be written as:

$$\hat{H}_e = g_e \mu_B \hat{\boldsymbol{S}}_e \cdot \boldsymbol{B} \tag{3.3}$$

In the X^+-Mn complex, where the two hole spins are antiparallel, the only remaining exchange interaction occurs between Mn and the electron. It can be described as:

$$\hat{H}_{X^+-\text{Mn}} = I_{e-\text{Mn}} \hat{\boldsymbol{S}}_{\text{Mn}} \cdot \hat{\boldsymbol{S}}_e \tag{3.4}$$

where $I_{e-\text{Mn}}$ is the exchange energy between Mn and e.

Similar to the model for non-passivated Mn [6], the theoretical PL emission spectra are obtained by diagonalizing the Hamiltonians of the initial (X^+-Mn) and final (h-Mn) states in the X^+ transition. The PL intensity emitted for the transition from inital $|i\rangle$ to final $|f\rangle$ state is determined by considering the matrix elements $\langle f|\hat{P}_{\sigma^+}|i\rangle$ ($\hat{P}_{\sigma^+}$ is the dipolar operator for σ^+ polarisation) and the population ρ_{ii} of the initial state. Assuming thermalization occurs in the final state of the system to an equilibrium temperature (T_{FS}), the ρ_{ii} can be deduced from the partial trace of the final state density matrix $\rho_{\text{FS}} = e^{-H_{\text{FS}}/\hat{k}_B T_{\text{FS}}}/\text{Tr}[e^{-H_{\text{FS}}/\hat{k}_B T_{\text{FS}}}]$.

Let us consider now the simplest case for the X^+ state when there is no strained-induced anisotropy on Mn ($\hat{H}_s$=0), and when Mn is on the axis of a QD with cylindrical symmetry, causing also the Hamiltonian $\hat{H}_a$ to vanish. In this model, we have not introduced any valence-band mixing. Assuming that the trapped hole h has a pure heavy-hole character, we consider the parameter Δ_{HL} in $\hat{H}_{HL}$ (Eq. 1.8) to be of the order of a few 10 meV [6]. With exchange interactions $I_{h-\text{Mn}} = 0.2$ meV and $I_{e-\text{Mn}} = -0.05$ meV, we obtain the theoretical PL density plot presented in Fig. 3.2d. This plot reflects the situation encountered in a symmetrical II-VI QDs doped with a single Mn atom [93–95]. Namely, in the initial state for this case, the electron-Mn complex consists of two energy levels, as shown in Fig. 3.3b. Here, M represents the quantum number associated with the total spin of the electron and Mn. The exchange interaction between the electron and Mn is an isotropic Heisenberg-type interaction. Consequently, the lower energy level ($M = 3$) exhibits a sevenfold degeneracy, while the higher energy level ($M = 2$) is fivefold degenerate. In the final state, the interaction between the hole and Mn exhibits an Ising-like character since $\Delta_{HL} \gg I_{h-\text{Mn}}$. This results in six energy levels, each of which is twice degenerate. They are formed by associating six Mn spin projection ($S_{\text{Mn},z}$) with each heavy hole spin ($J_{h,z} = \pm 3/2$). Therefore, at zero magnetic field ($B_z = 0$), we would expect to observe 12 distinct peaks. However, since the transition from the initial state $M = 2$ to the highest energy final state is forbidden, only 11 peaks are detected. The PL spectrum is actually a superposition of two substructures: six lines with decreasing intensities as their energy increases (transitions from state $M = 3$) and five lines with increasing intensities as their energy increases (transitions from state $M = 2$) [94]. This is in agreement with the 11 peaks and their intensities identified in Fig. 3.3a, which is extracted from the theoretical density plot (Fig. 3.2d) for $B_z = 0$. Additionally, it should be noted that the chosen sign of exchange energies indeed corresponds to the situation reported for Mn-doped II-VI QDs, where the $h-$Mn interaction has an anti-ferromagnetic character, while the $e-$Mn exchange interaction is ferromagnetic [1, 96]. This theoretical model provides an effective description of Mn-doped II-VI QDs, and should be extended to describe H-passivated Mn dopant in III-V QDs, by including non-vanishing $\hat{H}_s$ and $\hat{H}_a$ terms.

3.3 Modelling experimental results

3.3.1 Choice of parameters

In the theoretical plot of Fig. 3.3a, we initially assumed that the e-Mn exchange interaction was much larger than the strain anisotropy ($\epsilon_{||}$ and $\epsilon_{\perp}$) and the anisotropic exchange (ρ) due to the Mn off-centered position. However, to model the complex set of anticrossings observed in the experimental PL density plot for QD2 (Fig. 3.4a), we need to consider the opposite situation. A similar situation is encountered for positively charged II-VI semiconductor QD doped with a single Cr^+ ion in Ref. [97, 98]. This assumption is indeed justifiable in the case of a H-passivated Mn dopant, since the position of the Mn is no longer centered in the As tetrahedron, which could cause $e-$Mn exchange interaction to vanish. Therefore, we now consider $I_{e-\text{Mn}}$ to be negligible and introduce the parameters describing strain and the Mn non-centered position (as

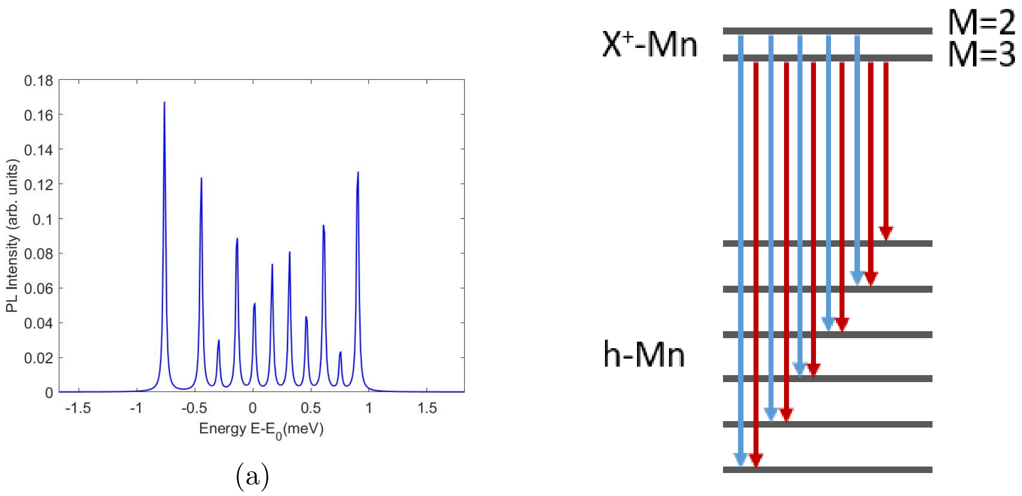

(a)

(b)

Figure 3.3: (a) PL spectrum of the positive trion X^+ state at $B_z = 0$ T generated by the theoretical model assuming that there is no strain and that Mn is in the center of QD. (b) Schematic of the energy levels and excitonic transitions from the initial ($X^+{-}$Mn) to the final (h-Mn) state of the positive trion in such a QD.

presented in Table 3.1).

g_{Mn}	g_h	g_e	$T_{\text{FS}}(K)$	
2	0.8	-0.5	20	
$\epsilon_{\|\|}$	$\epsilon_{\perp}$	θ_s	ϕ_s	ψ_s
0.175	0	80°	0°	0°
$I_{h-\text{Mn}}$	$I_{e-\text{Mn}}$	ρ	θ_a	ϕ_a
-0.275	0	-0.55	90°	0°

Table 3.1: Parameters used for the theoretical model for QD2 presented in Fig. 3.4b. Strains $\epsilon_{||}$, $\epsilon_{\perp}$ and exchange energies $I_{h-\text{Mn}}$, $I_{e-\text{Mn}}$ are given in meV.

The strain anisotropy ($\hat{H}_s$ term) in QD2 is characterized by two main parameters: the biaxial strain $\epsilon_{||}$ and the quite large angle θ_s, whereas the in-plane strain anisotropy $\epsilon_{\perp}$, assumed to be much smaller, is not considered for simplicity. The angle θ_s describes the orientation of the biaxial strain strongly perturbed by the nearby H atom. This strain anisotropy has a significant effect on the initial state ($X^+{-}$Mn), splitting it into three degenerate levels in zero magnetic field. These levels correspond to the Mn spin projections along the strain axis: $\pm 5/2$, $\pm 3/2$ and $\pm 1/2$, each twice degenerate because of the (non-interacting) electron spin up or down. The energy levels of the $X^+{-}$Mn state in the presence of a magnetic field for the electron and Mn spin projections along growth axis z are shown in Fig. 3.5a and Fig. 3.5b, respectively. On the other hand, the effect of biaxial strain on the final state ($h-$Mn) results in the appearance of some anticrossings around $|B_z| \approx 4$ T, but alone it fails to reproduce the experimentally observed spectral features.

To obtain a complex set of lines and anticrossings as observed in the experimental data, it is crucial to combine the strain anisotropy with the anisotropic exchange ($\hat{H}_a$ term) arising from the Mn position with respect to the QD center. This term does not impact the levels of X^+-Mn state, as it is present only in the Hamiltonian of final state (h-Mn). By selecting specific values for the anisotropic exchange parameter ρ and the angle θ_a, in addition to adjusting the biaxial strain and $I_{h-\mathrm{Mn}}$, we were able to reproduce most of the characteristic features of the experimental plot, as shown in the simulation in Fig. 3.4b. The energy levels of hole and Mn spin projections along the growth axis z are depicted in Fig. 3.5c and Fig. 3.5d, respectively. They exhibit an intricate set of anticrossings for different magnetic fields. In addition, some typically forbidden transitions become permitted due to the presence of this strong anisotropic exchange. In a zero magnetic field, the h-Mn state consists of a total of 10 levels, with two of them being twice degenerate. Notably, due to the ρ parameter, there is a strong mixing of Mn spin states at lower magnetic field. The evidence of this is most apparent around $B_z = 0$ T, when the average Mn spin projection along the z-axis is zero (green lines in Fig. 3.5d).

Another important parameter for modelling the experimental results is the $h-$Mn exchange interaction. The value of $I_{h-\mathrm{Mn}}$ is chosen to reproduce the overall splitting of the spectra. Interestingly, to achieve good agreement with the experimental results, we found that a negative sign for the $h-$Mn interaction is necessary. The negative $I_{h-\mathrm{Mn}}$ not only allows us to reproduce the higher PL intensity concentrated on the low-energy side of the spectra in negative B_z and on the high-energy side for positive B_z, as observed in [97], but it is also crucial for reproducing some of the anticrossings and the crosslike pattern observed in the top part of the plot between 0 and 1 T. This is in contrast to the positive $I_{h-\mathrm{Mn}}$ used in the model to reproduce the characteristic spectra of Mn-doped II-VI QDs in Fig. 3.2d, as well as in modelling Mn-dopants forming neutral acceptor state in InGaAs QDs [6]. A positive $I_{h-\mathrm{Mn}}$ is consistent with the antiferromagnetic character of the $p-d$ exchange reported in the literature for Mn atoms in diluted magnetic semiconductors [63, 99]. The present reversed sign of $I_{h-\mathrm{Mn}}$ in modelling H-passivated Mn dopant in InGaAs QDs means that the $h-$Mn exchange interaction in this case is ferromagnetic. This likely indicates a situation where the 3d levels of the Mn atom, due to the modification of its hybridization, would be positioned above the top edge of the valence band [97].

It should be mentioned that our model contains certain inherent redundancy that cannot be eliminated solely through comparison with the available experimental data. Namely, in the diagonal terms of the final state Hamiltonian, the parameter $I_{h-\mathrm{Mn}}$ is multiplied by a factor $A = \frac{15}{4} + \frac{15}{2}\rho\left(\frac{9\cos^2\theta_a}{4} + \frac{3\cos^2\theta_a}{4}\right)$. As a result, in our simulations for Fig. 3.2d and 3.4b, we noticed that by taking the opposite sign for $I_{h-\mathrm{Mn}}$, adjusting its value, and increasing the value of parameter ρ, it was possible to reproduce the same plots. This is because the factor A changes sign, indicating that the sign of the $p-d$ exchange in our model is determined by the term $AI_{h-\mathrm{Mn}}$. To reproduce the experimental results for QD2, it is indeed necessary to have a negative $AI_{h-\mathrm{Mn}}$. For Fig. 3.2d and 3.4b, the value and sign of $I_{h-\mathrm{Mn}}$ is chosen in such a way that we took

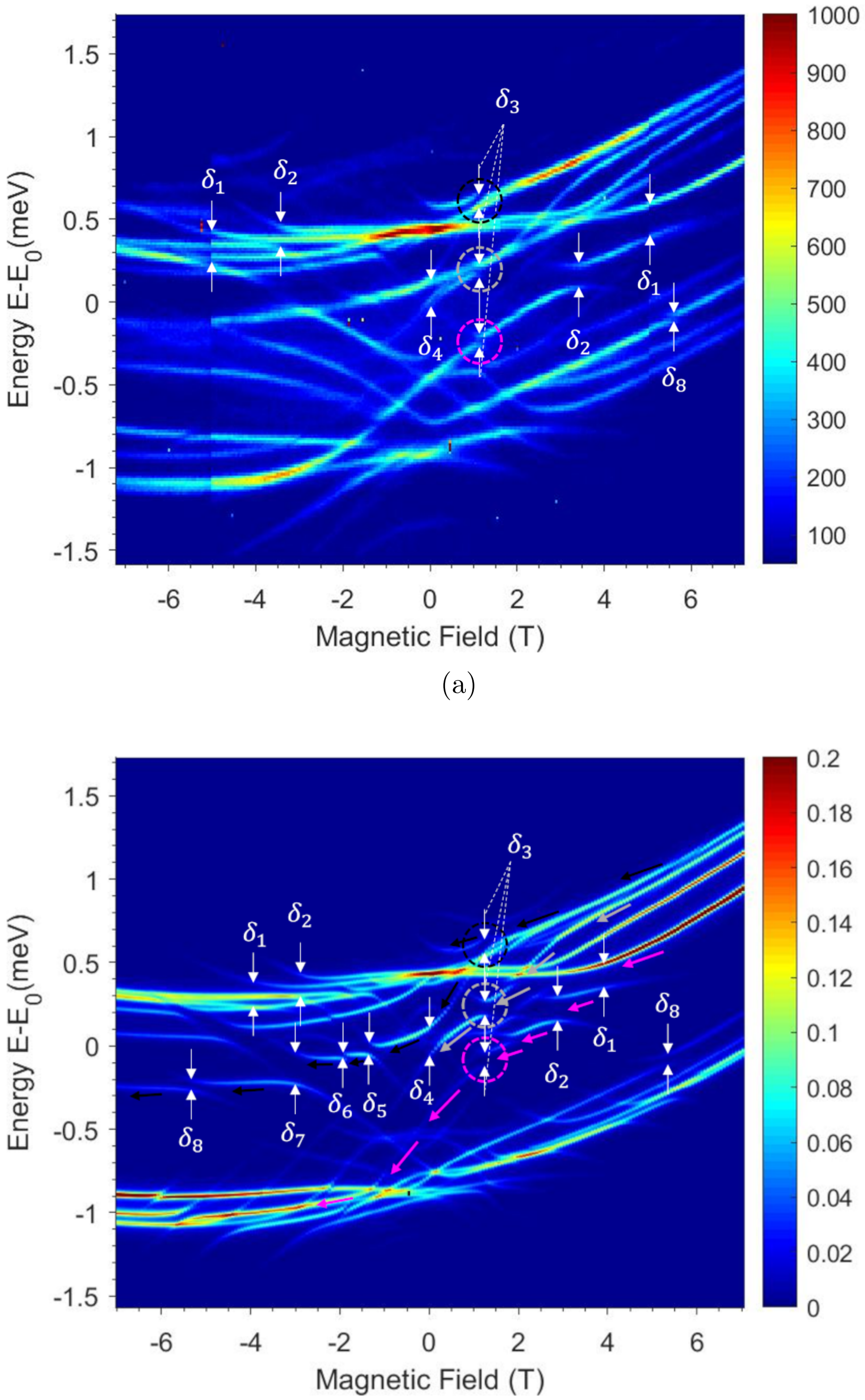

(a)

(b)

Figure 3.4: (a) µPL density plot for the X^+ state in QD2 as a function of the longitudinal magnetic field B_z and the detection energy $E - E_0$ ($E_0 = 1.356$ eV). (b) Corresponding theoretical simulation of the PL density plot. Several significant anticrossings are indicated in both plots.

the smallest ρ and positive A, resulting in the observed plots.

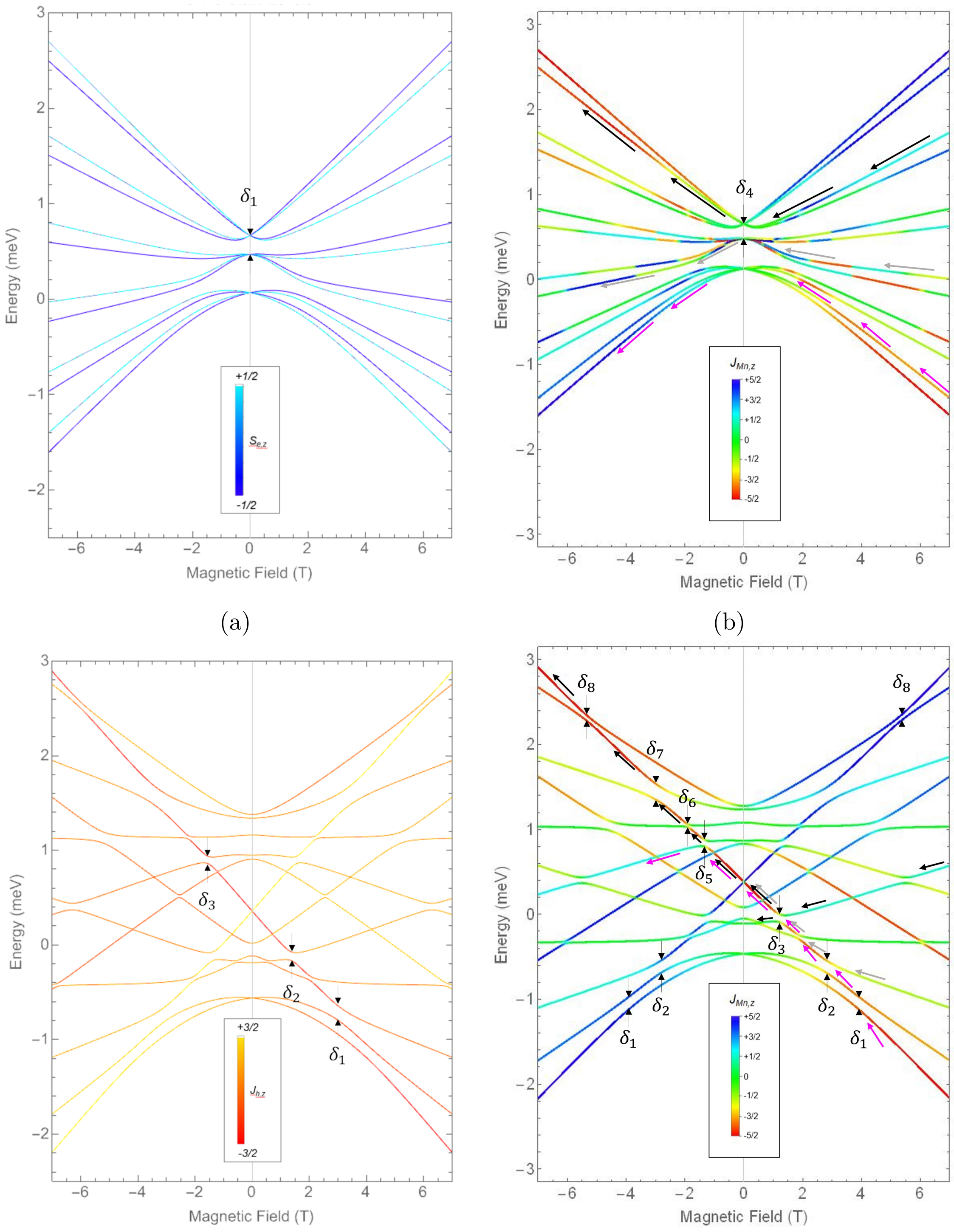

(a) (b) (c) (d)

Figure 3.5: Calculated energy levels of the initial ($X^+{-}$Mn) state for (a) electron and (b) Mn spin projections along growth axis z, as well as the levels of the final ($h{-}$Mn) state for (c) hole and (d) Mn spin projections along growth axis z. The color scale for each particle (electron, hole, and Mn) corresponds to their angular momentum projections along the QD growth axis z.

In Ref. [97, 98], it was demonstrated that to model a similar complex anticrossings pattern in a magnetic field, it was necessary to introduce heavy-hole/light-hole band mixing due to QD in-plane asymmetry and shear strain. However, in our model, hh-lh band mixing is introduced differently through the term $\hat{H}_a$. This introduces spin-flip terms, even for a symmetric QD, when the Mn impurity is off-axis, as reported in Ref. [75]. Therefore, in our model, the combination of the anisotropic exchange term ($\hat{H}_a$) with strain anisotropy ($\hat{H}_S$) was sufficient to explain the observed anticrossings and forbidden transitions (which involve Mn spin flips) in a longitudinal magnetic field.

3.3.2 Energy levels of QD2

To understand the origin of some of the most notable features observed in the PL density plot of QD2 under a magnetic field (Fig. 3.4a), we can analyze the features produced by the model and compare them to the experimental observations. Series of different anticrossings can be observed both in the Fig. 3.4b and in the calculated levels in Fig. 3.5.

We can start by looking at the transitions from the lowest energy level of $X^+{-}\text{Mn}$ to ground state levels of $h{-}\text{Mn}$. The evolution of these transitions as a function of magnetic field is indicated with pink arrows in the energy levels in Fig. 3.5, as well as in the density plot in Fig. 3.4b. Starting from $B_z = 7$ T, a strong intensity line is observed which corresponds to the transition from the lowest energy level of $X^+{-}\text{Mn}$ to $h{-}\text{Mn}$ for Mn spin $J_{\text{Mn},z} = -5/2$. Around $B_z = 4$ T, the first anticrossing δ_1 is observed. A similar feature is seen in the experimental data, but it occurs around $B_z = 5$ T. The same anticrossing is observed at the opposite magnetic field. With further reduction of magnetic field, another set of anticrossings, labeled as δ_2, appears. They are observed in both negative and positive magnetic fields, occurring at approximately $|B_z| \approx 3.5$ T in the experimental data and around $|B_z| \approx 3$ T in the model. In both cases, the value of this crossing is estimated to be $\delta_2 \approx 140$ µeV. After this, another anticrossing that is observed both in the model (around $B_z = 1.4$ T) and experimentally (around $B_z = 1.1$ T) is δ_3 (pink circle in Fig. 3.4). The value of δ_3 is estimated to be around 80 µeV in both cases. After this anticrossing, at ground state $h{-}\text{Mn}$, Mn spin projection along the z-axis is -5/2 (as indicated by the pink arrow in Fig. 3.5d). At negative magnetic fields, the transitions from the lowest energy level of $X^+{-}\text{Mn}$ further evolve (one of the transitions is indicated by a pink arrow) and undergo some anticrossings that will not be analyzed further, as they are not clearly observed in the experimental data.

The same anticrossing δ_3 is observed at higher energies as well, for the transitions from the second level of $X^+{-}\text{Mn}$ (grey circle) and the highest energy level of $X^+{-}\text{Mn}$ (black circle). The levels that participate in these transitions are indicated in energy level diagrams of $X^+{-}\text{Mn}$ and $h{-}\text{Mn}$ with grey and black arrows. Transitions from the highest energy level of $X^+{-}\text{Mn}$ to $h{-}\text{Mn}$ (black arrows) start with the transitions involving Mn spin $J_{\text{Mn},z} = +1/2$ (cyan lines) at $B_z = 7$ T. After this anticrossing δ_3 (black circle), transition toward Mn spin $J_{\text{Mn},z} = -5/2$ state of the $h{-}\text{Mn}$ state (red lines in the diagram) also become allowed, resulting in a crosslike pattern. The anticrossing δ_4 observed at $B_z = 0$ T arises from the lines originating from transitions between the two upper levels of X^+−Mn and the same level of the ground state with Mn spin $J_{\mathrm{Mn},z} = -5/2$ (red line in the middle of the h−Mn diagram). The splitting δ_4 is determined to be approximately $\delta_4 \approx 140$ µeV for the experimental data and $\delta_4 \approx 170$ µeV for the model.

A series of anticrossings, denoted as δ_5 to δ_8, is observed in Fig. 3.4b for magnetic fields between -1 T and -5.5 T. All these anticrossings result from transitions involving the same highest energy level in X^+−Mn. However, these anticrossings are not as clearly resolved in the experimental plot. It is possible that in these experimental plots, there is a small anticrossing around -1.2 T and another one around -2.5 T. However, establishing a direct correspondence with the anticrossings produced by the model is challenging. On the other hand, anticrossing δ_7 is observed around 5.5 T, both in the experimental data and in the model.

As observed from the analysis of the energy levels of X^+ in QD2, our model reproduces reasonably well the experimental magneto-PL density plot. Many of the anticrossings and forbidden transitions are well replicated around similar magnetic fields in both the experimental and theoretical results.

3.4 Resonant optical excitation of Mn spin states

To further validate the structure of energy levels predicted by the model, we conducted resonant optical excitation measurements at zero magnetic field in a cross-polarized configuration as in Chapter 2. By establishing correlations between the excited transitions and observed resonance Raman scattering at lower energy (or possibly higher) transitions, we can gain insights into a common excited level shared by these transitions and compare the model's predictions to experimental observations.

In this resonant excitation measurement, we keep a weak non-resonant He-Ne laser ($E = 1.95$ eV) and Ti:Sapphire laser ($E = 1.42$ eV) (total power ~ 6 µW) to charge QD2 with a hole, allowing us to address the X^+ transitions. The resulting PL spectrum due to this weak non-resonant excitation is represented by the black line in Fig. 3.6a. For resonant excitation, we employed a tunable narrowband cw laser (Toptica DLCPro, $P = 1.4$ µW) which is scanned over the full range of energies where QD2 transitions are observed. The recorded series of µPL spectra is displayed in the form of a density plot in Fig. 3.6b. The diagonal line of strong intensity corresponds to the scanning resonant laser, still quite visible in spite of the cross-polarization configuration. The apparent jumps observed for this line (cut in height by the range chosen for the colorscale) are due to the oscillations in the optical density of the setup as a function of the wavelength, as discussed in Chapter 2. The weaker vertical lines correspond to the PL signal of 9 peaks observed under non-resonant excitation. When certain transitions are resonantly excited by the scanning laser, a clear increase in the signal is detected on some other transitions. This corresponds to resonance Raman scattering, occurring when these transitions share a common excited state whose population is increased by the resonant laser, as depicted by the diagrams in Fig. 3.7b and 3.7c. For a more detailed analysis of these resonances, we label the observed experimental peaks as indicated in Fig. 3.6a. The theoretical spectrum shown in Fig. 3.7a is extracted from Fig. 3.4b for $B_z = 0$ T. By comparing the experimental data and model at $B_z = 0$ T, as well as the evolution of transitions in the magnetic field (Fig. 3.4), we attribute certain

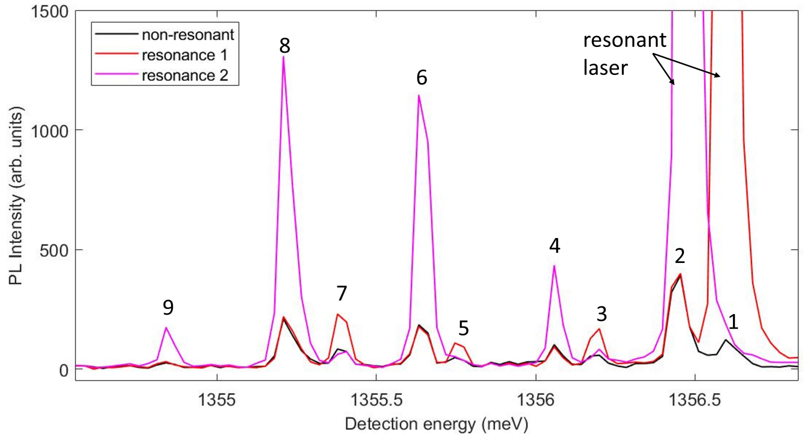

(a)

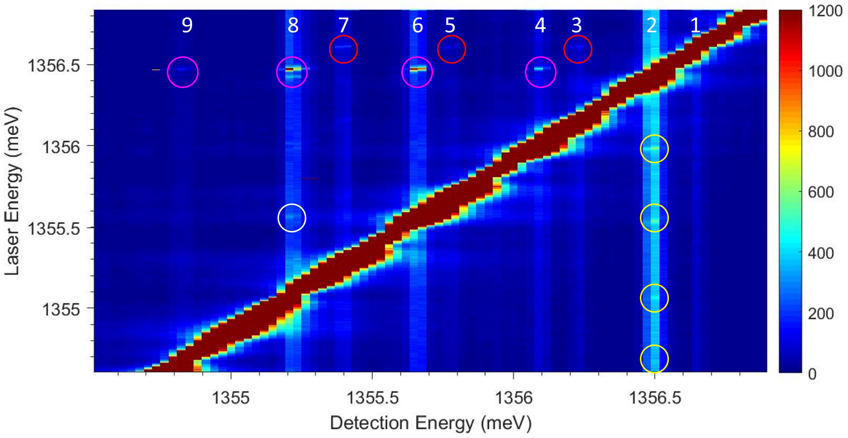

(b)

Figure 3.6: (a) µPL spectra of X^+ state in QD2 at $B_z = 0$ T. The black line represents the non-resonant laser excitation, while the red and purple lines correspond to the resonant excitation of transitions 1 and 2, respectively.(b) Density plot of µPL emission as a function of detection energy and resonant laser energy. The strong intensity diagonal line represents the resonant laser. For laser resonant with transition 1 and 2, corresponding resonances at other transitions are indicated with red and purple circles, respectively.

peaks to their experimental counterparts, as labelled in Fig. 3.7a. In the analysis of this measurement, we particularly focus on the resonant excitation of the two highest energy peaks (1 and 2), as the increase in PL intensity of the other transitions is most evident in those cases. The PL spectra when the laser is resonant with transition 1 and 2 are shown in Fig. 3.6a as red and purple lines, respectively.

When the laser is resonant with the highest energy transition (peak 1), an increase in the signal is observed for peaks 3, 5 and 7. From the theoretical spectrum and structure of levels generated by our model, we can determine the transitions to which these peaks correspond. The simplified scheme of $h-$Mn and X^+-Mn levels at zero magnetic field is shown in Fig. 3.7b. The transition 1, excited by the resonant laser, corresponds to the transition from one of the lowest energy $h-$Mn states to the top

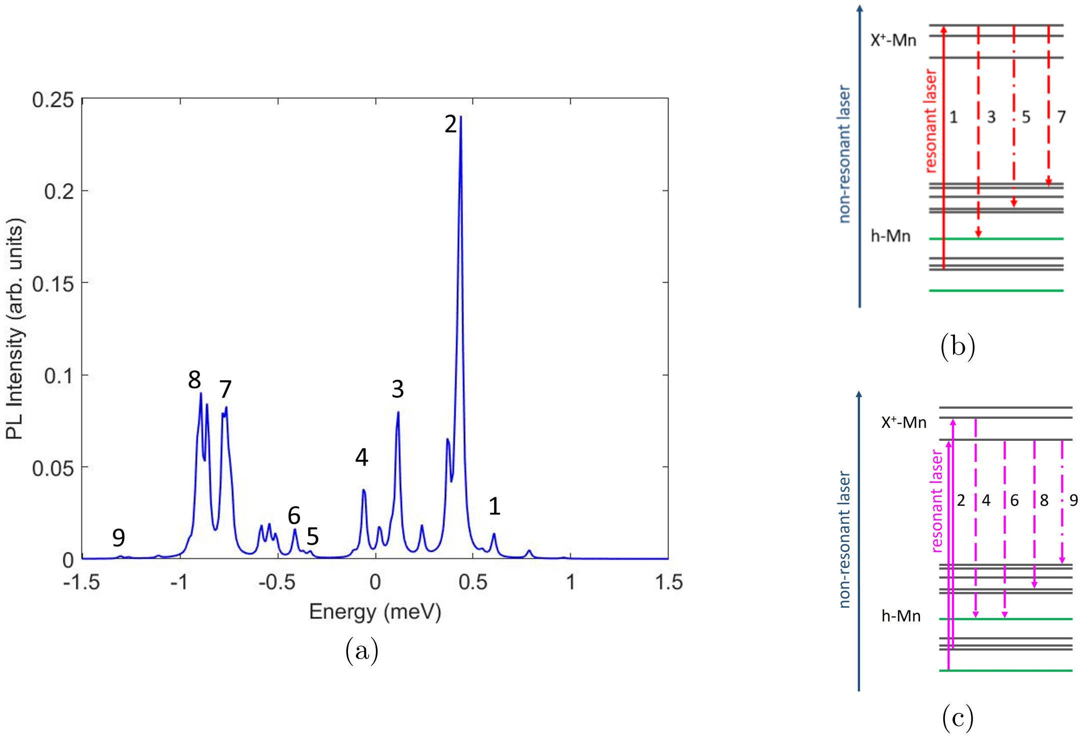

(a)

(b)

(c)

Figure 3.7: (a) PL spectrum at $B_z = 0$ T generated by the theoretical model for QD2. (b), (c) Schematic representation of the energy levels involved in the transitions from $X^+{-}$Mn to $h{-}$Mn state. Two twice degenerate $h{-}$Mn levels are presented with green lines. The non-resonant laser excitation (blue arrow) and the laser used for resonant excitation of peak 1 (red arrow) and peak 2 (purple arrows) are indicated. The corresponding emitted PL signal is indicated with red and purple arrows.

energy level in $X^+{-}$Mn. The increase in the signal is observed for peak 3, which corresponds to the higher energy line at the anticrossing δ_4, which is indicated with black arrow in Fig. 3.4b. As discussed earlier, this line is a result of transition from the highest energy level of $X^+{-}$Mn to the twice degenerate level in the middle of the $h{-}$Mn scheme in Fig. 3.5d. Peak 7 can also be recognized in both the experimental and simulation data as the transition that corresponds to one of the highest energy levels of $h{-}$Mn (line participating in anticrossing δ_7 in Fig. 3.5d). Peak 5 is not very well reproduced by our model. Namely, in Fig. 3.7a at a slightly higher energy than peak 6, we see a very weak signal that potentially could be attributed to peak 5. This peak comes from the transition to the level of $h{-}$Mn represented by the line participating in the anticrossings δ_5 in Fig. 3.5d. As suspected, in this case, all the transitions for which an increase in signal is observed when the resonant laser is at peak 1 are related to the same excited state.

We now consider the resonant excitation of peak 2 and try to perform the same analysis of connected levels. However, in this case, the situation is a little more complex since peak 2 in model likely results from at least two transitions that happen at basically the same energy and that involve two different excited states. These transitions are indicated in Fig. 3.7c. When the laser is around the energy of peak 2, the increase in PL signal is observed for peaks 4, 6, 8, and 9 in Fig. 3.6b. However, when examined more closely with smaller step of scanning resonant laser, as depicted in Fig. 3.8, a few consecutive resonances are observed at the energy of these peaks.

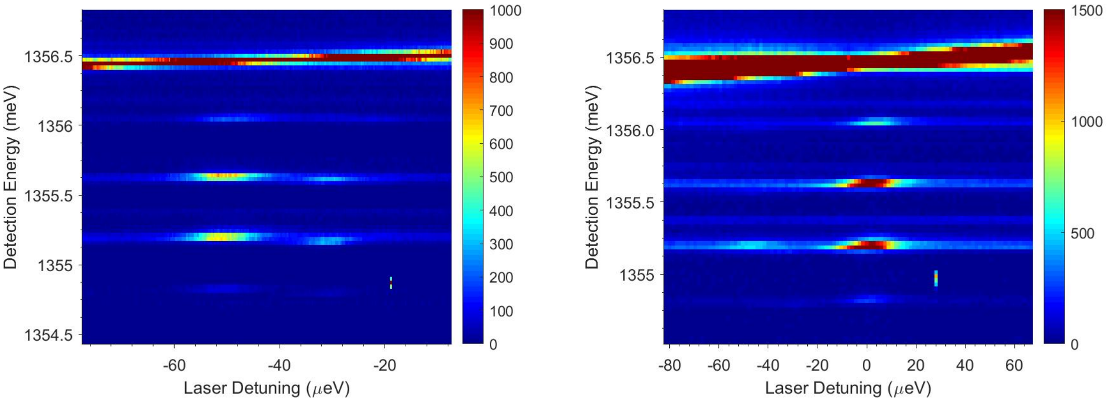

(a) (b)

Figure 3.8: (a) and (b) Density plot of µPL emission as a function of detection energy and resonant laser energy detuning, with a power of 0.4 µW (a) or 1 µW (b), and a scan step of (a) 0.25 pm or (b) 1 pm. The typical linewidths of the resonances amount to about 10 µeV in (a) and 18 µeV in (b).

The transitions that are resonantly excited by the laser at the same time are indicated in Fig. 3.7c. One of the transitions is between the lowest energy levels of the excited and ground state. The other one is related to the transition from the second excited state to one of the lower energy levels in h−Mn. Therefore, we can now observe an increase in signal for the transitions that come from both levels of X^+−Mn excited by the laser. Peak 4 corresponds to the line at the anticrossing δ_1, as seen in Fig. 3.5a, and it is related to the transition from the middle energy excited state. Peak 6 comes from the line seen after the lowest energy anticrossing δ_2 in Fig. 3.4b, which is related to the lowest energy excited state. Peak 8 corresponds to the transition from the lowest level of X^+−Mn to one of the two levels of h−Mn indicated in Fig. 3.7c. These transitions in our model are separated by only about 20-30 µeV. In the experimental data, these transitions are not resolved since the spectral resolution for this measurement was 28 µeV. Peak 9 is not reproduce by our model, but according to the energy distance from peak 8, it could correspond to the transition from the lowest energy excited state to the highest energy ground state.

As a conclusion of this section, it clearly appears that the resonant excitation measurement confirms our model of H-passivated Mn dopant, by reproducing the experimental results reasonably well. The increase in PL signal of certain peaks for the resonant excitation of different levels of X^+−Mn, and notably the number of these resonances, is consistent with the structure of levels created by our model. Conversely, it would be highly inconsistent with the level structure of a Mn dopant in the A^0 configuration.

3.5 Annealing the hydrogenated sample

Following these experiments on H-passivated Mn-doped QDs, the sample was subjected to a soft-annealing process, similar to the one described in Ref. [90], to remove hydrogen atoms and restore the neutral acceptor state of the Mn dopant. The annealing process was carried out for one hour at 400°C in N_2 atmosphere. After this treatment, to investigate the presence of usual Mn-doped InGaAs QDs, we excited the sample with a non-resonant lasers as before (He-Ne $E = 1.95$ eV and Ti:Sapphire $E = 1.42$ eV), and examined the PL spectrum at zero magnetic field. In particular, we scanned the area of the sample around the position where QD2 and QD3 were previously observed. The PL spectra for two of these QDs (QD4 and QD5) are presented in Fig. 3.9. Two more QDs with similar spectral characteristics as QD4 were also found in this part of the sample, indicating that dehydrogenation was indeed successful. However, since the energy of transitions for the X^+ trion in Mn-doped QDs is likely modified with respect to the H-passivated configuration, the average energy of a magnetic QD cannot be used as a reference for finding the same QD. As the sample had no very clear marks on its surface, it is difficult to definitively claim that one of these new magnetic QDs corresponds to the previous hydrogenated QD2, but it is certain we could not find anymore the PL spectrum of QD2 in the inspected area.

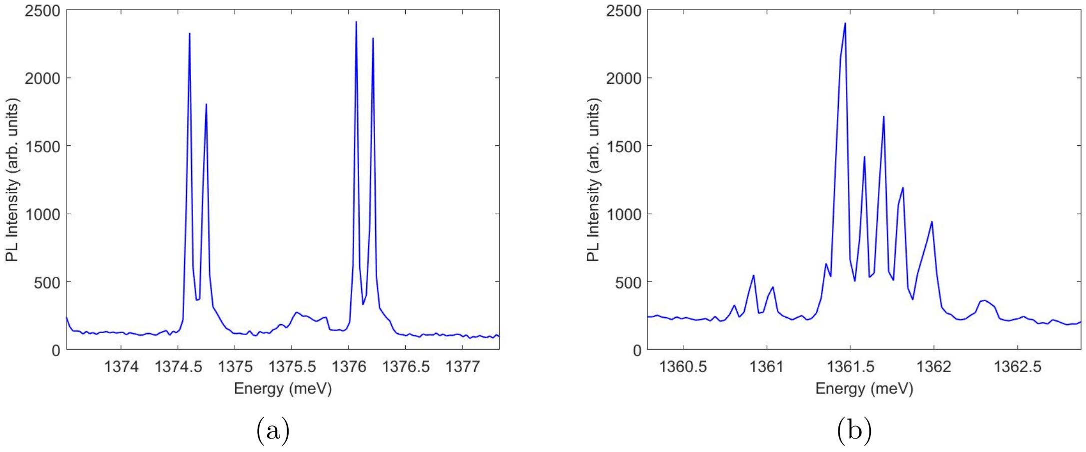

(a) (b)

Figure 3.9: (a) and (b) PL spectra of the positive trion X^+ state at $B_z = 0$ T, obtained under non-resonant optical excitation at 1.42 eV for QD4 and QD5, respectively.

The PL spectrum of QD4 (Fig. 3.9a) exhibits the same features observed in previous chapters for the non-hydrogenated Mn, indicating that the annealing process successfully removed hydrogen and restored the Mn dopant to its original state, where it forms the A^0 state. The second PL spectrum (Fig. 3.9b) corresponding to QD5, is less-obviously a standard Mn-doped QD. To check this, we investigated their behavior under a longitudinal magnetic field up to 5 T and detected both σ^+ and σ^- polarizations, as shown in Fig. 3.10.

For QD4, we observe a characteristic crosslike pattern as discussed previously in Section 1.2.1. The anticrossings occur at $B_z = 0$ T and $B_z = -4.5$ T, confirming that this is indeed a positive trion X^+. To roughly model this density plot, we used the model presented in section 1.2.3. The parameters used to generate the plot in

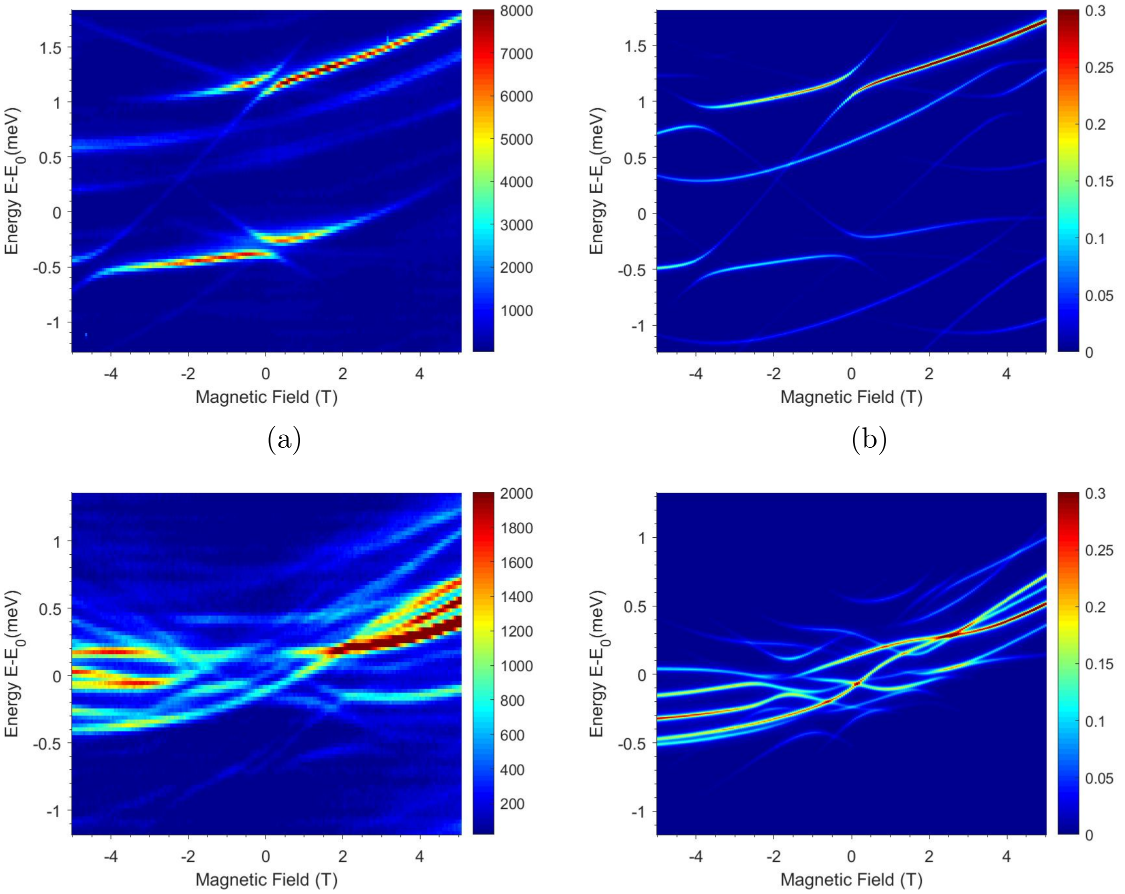

(a) (b)

(c) (d)

Figure 3.10: µPL density plots as a function of longitudinal magnetic field B_z for (a) QD4 centered at $E_0 = 1.375$ eV and (c) QD5 centered at $E_0 = 1.3616$ eV. (b), (d) Theoretical simulation of the PL density plots for QD4 and QD5, respectively.

Fig. 3.10b are summarized in Table 3.2. We used the values of Landé factors similar to those in section 1.2.1 and in Ref. [6]. The other parameters that describe the local anisotropy, exchange interactions, and A^0 position anisotropy were adjusted manually by comparing the simulation with the experimental results. Parameters related to strain anisotropy had similar values as those for first QD in section 1.2.3. However, in order to reproduce almost twice as wide crosslike pattern compared to the one in Fig. 1.13, we had to use a strong anisotropic exchange parameter ρ. It is possible that by adjusting a few parameters, good results could be obtained even for smaller values of the parameter ρ. However, as the purpose here was just to demonstrate that both QD4 and QD5 contain non-hydrogenated Mn dopants and can thus be described by the model from section 1.2.1, we did not spend additional time optimizing the parameters used. The parameters describing exchange interactions between particles were adjusted simultaneously to reproduce the width of the pattern and anticrossings.

As expected from the PL spectrum in zero field, QD5 exhibits a rather complex set of features (Fig. 3.10c). Some of these features are reproduced by the model (Fig. 3.10d). Although the model does not perfectly match the experimental results,

	g_{Mn}	g_{h_1}	g_{h_2}	g_e	$T_{\text{FS}}(K)$	
	2	0.6	0.8	-0.5	20	
	$\epsilon_{\|\|}$	$\epsilon_{\perp}$	θ_s	ϕ_s	ψ_s	
QD4	6.25	2.5	-120°	30°	50°	
QD5	2.1	0.75	10°	75°	10°	
	$I_{h_1-\text{Mn}}$	$I_{h_2-\text{Mn}}$	$I_{h_1-h_2}$	ρ	θ_a	ϕ_a
QD4	2.5	0.36	0.5	-0.65	70°	-90°
QD5	3.75	0.45	1.35	-0.07	100°	100°

Table 3.2: Parameters used for the theoretical model of QD4 and QD5 after annealing. Strains $\epsilon_{||}$, $\epsilon_{\perp}$ and exchange energies $I_{h_1-\text{Mn}}$, $I_{h_2-\text{Mn}}$, $I_{h_1-h_2}$ are given in meV.

it appears that QD5 is compatible with a neutral acceptor state of Mn. To generate this theoretical plot, we used almost three times smaller values for uniaxial and in-plain shear strains and a value of anisotropic exchange parameter ρ closer to the one for second QD (Fig. 1.14) in section 1.2.3. However, being able to model both QDs with the model for Mn dopant in A^0 state confirms that the QDs in this sample are no longer hydrogenated and that their original configuration is restored.

3.6 Summary

In this chapter, we have investigated the properties of H-passivated Mn dopant in InGaAs quantum dots using both experimental and theoretical approaches. The µPL measurements for these QDs reveal a complex set of lines that exhibit an unusual evolution in a longitudinal magnetic field, resulting in an intricate series of anticrossings. To interpret these experimental results, we developed a theoretical model for H-passivated Mn dopant, taking into account parameters such as strain anisotropy, exchange interactions, and the position of the Mn dopant within the QD. The model relatively well reproduces the observed PL density plots and anticrossings. Notably, to achieve this qualitative agreement with the experimental results, we found it necessary to consider a ferromagnetic character for the $h-$Mn exchange interaction. This contrasts with the antiferromagnetic $p-d$ exchange typically reported for Mn-doped II-VI and III-V QDs [1, 6], and therefore could deserve further attention in the future.

Furthermore, a detailed analysis of the energy levels using the theoretical model allows us to attribute specific features in the PL spectra to transitions between excited and ground state levels of the positive trion X^+ in QD with H-passivated Mn dopant. Resonant optical excitation measurements further validate the accuracy of the model.

Lastly, after annealing the sample, the Mn dopant was successfully restored to its original neutral acceptor state, leading to the observation of the usual spectral signature of Mn-doped InGaAs QDs. This restored sample will be utilized in Chapter 4 to study the optical Stark effect and photon dressing induced by a near-resonant strong optical excitation in a 4-level system.

Chapter 4

Coherence spectroscopy of a Mn-doped InGaAs/GaAs quantum dot

After the annealing process for dehydrogenation as described in Chapter 3, the sample has been used to study Mn-doped InGaAs/GaAs QD under (strong) resonant optical excitation. Our initial interest was to compare the resonance linewidths in a simple sample (operated with no dark current) to the very large 34 µeV obtained in the sample with Schottky diode in Chapter 2. Such measurements would help us understand possible influence of the electrical current passing through the diode and shed light on the potential reasons for broad resonance linewidth observed in section 2.3.2. Additionally, thanks to a few improvements of the set-up, exciting the Mn-doped QDs resonantly over a broader range of laser powers than in section 2.3.2 was made possible and lead us to perform two-laser experiments to study the strong coupling regime between QD states and a laser field [100]. The optical Stark effect and Autler-Townes splitting have already been observed for neutral InGaAs QDs [101, 102] and negatively charged InGaAs QDs [103, 104], as well as for exciton in Mn doped II-VI QDs [12]. The results presented in this chapter are the first investigations of these effects on Mn-doped InGaAs QDs.

Section 4.1 starts with a brief theoretical description of dressed states and the Autler-Townes effect, which will be the focus of the following experiments. In section4.2, we introduce the theoretical model based on the optical Bloch equations that will be employed to fit the experimental results presented in this chapter. A first series of measurements, conducted using a single resonant laser, is then presented and discussed with the help of the model. These measurements illustrate the emergence of Autler-Townes splitting under strong resonant excitation and explore its dependence on the detuning and power of the driving laser. The theoretical model offers additional insights into the physics of this QD and allows us to revisit the analysis of the results of section 2.3.2 for the QD1 in the Schottky diode sample. In section 4.3, experiments with two-laser probing are detailed. These experiment are done for V-like three level system. In the first configuration, a strong fixed laser is tuned resonantly with one of the transitions, while a weak laser scans through the other transition of the V-like system. This configuration enables us to investigate the dependence of Autler-Townes splitting on the power and detuning of the stronger driving laser. In the second part, we examine the reverse scenario, where a weak fixed laser is resonant with one of the transitions while a stronger laser scans across the other trnasition. We observe a narrow Lorentzian dip and its analysis provides evidence of quantum interference in addition to a population saturation effect (or spectral hole burning). Both the Autler-Townes effect and quantum interference which are observed despite the presence of strong inhomogeneous broadening demonstrates that the decoherence of the excited spin states is dominated by their radiative lifetime.

4.1 The dressed-atom picture

The Autler-Townes effect, which will be the subject of study in this chapter, arises from the strong coupling of a two-level system resonantly excited by a laser field. The emerging Rabi splitting, formed through this interaction, can be explained using the dressed-atom approach [105], even though in the next section we use a semi-classical description where the optical field is treated classically. We begin by considering two QD levels, denoted as $|a\rangle$ and $|b\rangle$, with an energy splitting of $\hbar\omega_0$ (see Fig. 4.1a). This transition is driven driven by a quasi-resonant laser with a frequency ω_L. The laser detuning is defined as $\delta_L = \omega_L - \omega_0$ and is much smaller than ω_0. In the following, we present the so-called Jaynes-Cummings model to describe this situation.

The first step is to consider the uncoupled system made of the QD levels and the laser field. The non-interacting Hamiltonian is the sum of two terms $H_0 + H_L$, where

$$H_0 = \hbar\omega_0 |b\rangle\langle b| \tag{4.1}$$

is the Hamiltonian describing the QD levels and

$$H_L = \hbar\omega_L (a^+ a + \frac{1}{2}) \tag{4.2}$$

represents the Hamiltonian of the laser mode at the QD position, with a^+ and a the creation and annihilation operators of a photon in this mode. Some eigenstates of $H_0 + H_L$ are depicted in Fig. 4.1b. They are labeled by two quantum numbers: the first corresponds to the quantum dot levels (a, b), and the second to the number N of laser photons. The energy difference between levels $|a, N-1\rangle$ and $|b, N\rangle$ is $\hbar\delta_L$. When the laser is resonant with the quantum dot transition ($\delta_L = 0$), the states $|a, N-1\rangle$ and $|b, N\rangle$ become degenerate.

These two states couple when the interaction between the quantum dot states and the laser mode is considered. In the electric dipole approximation, this interaction is described as $-\boldsymbol{d}\cdot\boldsymbol{E}$, where $\boldsymbol{d}$ is the transition dipole operator, and $\boldsymbol{E}$ is the laser field operator. The total Hamiltonian of the system becomes $H_0 + H_L + H_I$. The interacting Hamiltonian can be expressed as follows:

$$H_I = g\left(|b\rangle\langle a| + |a\rangle\langle b|\right)(a + a^+) \tag{4.3}$$

Here $g \propto \boldsymbol{\epsilon}_L \cdot \boldsymbol{d}_{ab}$ is the coupling constant, where $\boldsymbol{\epsilon}_L$ is the polarization of the laser mode and $\boldsymbol{d}_{ab} = \langle a|\boldsymbol{d}|b\rangle$. Using the usual rotating-wave approximation (valid for $\hbar\delta_L \ll \omega_0$) the above equation can be simplified to:

$$H_I \approx g\left(a^+|b\rangle\langle a| + a|a\rangle\langle b|\right) \tag{4.4}$$

The first term in the brackets describes the transition from level $|a\rangle$ to $|b\rangle$ with the emission of a photon, while the second term corresponds to the transition from level $|b\rangle$ to $|a\rangle$ with the absorption of a photon.

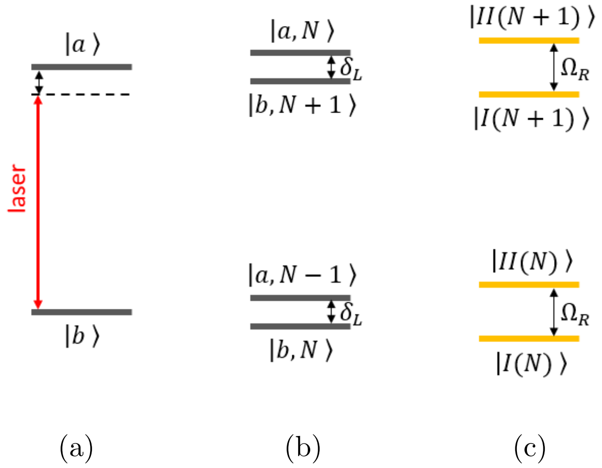

Figure 4.1: (a) Energy level diagram of two quantum dot states driven by a strong laser. (b) Uncoupled states of the quantum dot and laser system. (c) Dressed states of a two-level quantum dot driven by a strong laser field. States with the same photon number are separated by $\hbar\Omega_R$.

Due to the light-matter interaction H_I, the states $|a, N-1\rangle$ and $|b, N\rangle$ are coupled and transformed into two "dressed states", denoted as $|I, N\rangle$ and $|II, N\rangle$. As illustrated in Fig. 4.1c, we end up with a ladder of pairs of dressed states. Each pair of levels is split by an energy gap of $\hbar\Omega_R$, referred to as the generalized Rabi splitting Ω_R, which is defined as:

$$\Omega_R = \sqrt{\Omega^2 + \delta_L^2} \tag{4.5}$$

where Ω represents the Rabi frequency defined as $\Omega = 2g/\hbar\sqrt{N+1}$. The set of dressed states can be written as:

$$|I(N)\rangle = \cos\theta|b, N\rangle - \sin\theta|a, N-1\rangle \tag{4.6}$$

$$|II(N)\rangle = \sin\theta|b, N\rangle + \cos\theta|a, N-1\rangle \tag{4.7}$$

with the mixing angle given by $\tan 2\theta = -\frac{\Omega}{\delta_L}$. For a high intensity laser field, N is very large, so the field fluctuations $\propto 1/\sqrt{N}$ are small. This implies that the Rabi splitting between two successive pairs of dressed states is mostly unchanged. With this model in mind, we can now discuss the typical signatures observed when driving a two-level system with a strong laser.

4.1.1 Observing Rabi splitting of dressed states

Rabi splitting within a pair of dressed states can be observed either through the Mollow or Autler-Townes effect, involving the emission/absorption of a photon to/from a dressed states manifold (i.e., a given N).

For observing the Mollow effect [106], the experimental configuration must allow measuring the PL resulting from the emission between successive dressed state manifolds of the ladder, namely with a decreased number of one photon. As depicted in Fig. 4.2, there are four possible transitions (indicated by blue dashed arrows). Two of these transitions are degenerate with an energy of $\hbar\omega_0$, while the other two have energies of $\hbar\omega_0 \pm \hbar\Omega_R$. This leads to the observation of a triplet in the PL spectrum, known as the Mollow triplet.

On the other hand, the Autler-Townes effect [100] can be observed by measuring the PL signal for the spontaneous emission from the dressed states towards a third, spectator state far detuned from or not coupled to the laser field (red dashed arrows in Fig. 4.2). These spectator states (SS) also form a ladder ($|SS, N\rangle$, $|SS, N+1\rangle$,...), but the emitted photon does not belong to the laser mode, and these states $|SS, N\rangle$ are not split by the laser field. As a result, an Autler-Townes doublet, separated by Rabi splitting, is observed in PL spectrum. For this reason, the Rabi splitting is also referred to as Autler-Townes (AT) splitting , which will be the terminology used throughout this chapter. In addition, we can have another spectator state ($|SS, N\rangle$ on the left) that illustrates the absorption of photons without changing the laser mode photon number. This is indeed the case in our system when probing one of the transitions of the FM doublet while a strong laser drives the other transition of the FM doublet, as discussed in section 4.3.

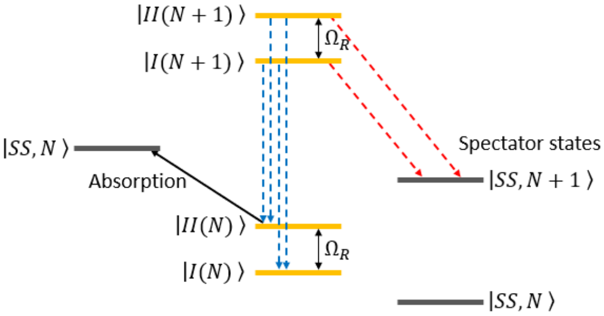

Figure 4.2: Energy level diagram of dressed states generated by strong laser excitation of a quantum dot transition. Blue dashed arrows indicate emissions associated with the Mollow triplet, while the red dashed arrows represent emissions toward a spectator state $|SS, N+1\rangle$, a characteristic feature of the Autler-Townes effect. Spectator states also form a ladder, while an additional spectator state is drawn on the left to depict the possible absorption process (black arrow).

Both of these effects can be observed in experiments where a quantum dot transition is strongly driven by a single laser, and the corresponding PL signal (dashed blue or dashed red arrows), as indicated in Fig. 4.2, is recorded. Such experiments have previously been reported for III-V QDs [79, 87, 107, 108]. Mollow triplet and Autler-Townes splitting can also be measured in two-laser experiments. In this setup, the pump laser drives a quantum dot transition, while a weak probe laser monitors either the same transition in the case of the Mollow effect or another transition that shares a common excited state (in the case of a Λ-type system) or a common ground state (in the case of a V-type system) for the Autler-Townes effect, as demonstrated in absorption measurements in Ref. [101, 103]. In this chapter, we will first report results confirming the emergence of Autler-Townes splitting and study its dependence on laser power in Mn-doped QDs using single-laser excitation. Subsequently, we will present pump-probe experiments conducted to gain a deeper understanding of this effect and to observe the coherence between the excited spin states.

4.2 Autler-Townes effect in single-laser probing experiments

4.2.1 Experimental configuration and single-laser measurements

In this chapter, we study one of the Mn-doped quantum dots in the annealed sample discussed in section 3.5. Fig. 4.3a shows the PL spectrum of the positive trion X^+ state in this QD6, obtained under non-resonant excitation. This QD exhibits the same characteristic spectrum as observed previously, consisting of two doublets in zero magnetic field. The splitting between the antiferromagnetic (AFM) and ferromagnetic (FM) doublets is $\Delta \approx 700$ µeV, while the splitting between the two excited states is $\delta_0 \approx 144$ µeV. For this QD, all four peaks exhibit nearly identical intensities, which means that the $e - A^0$ exchange interaction is negligible [6].

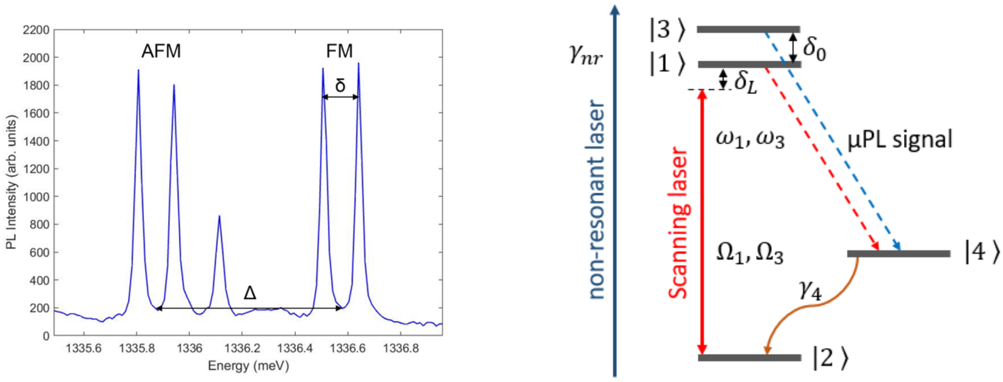

(a)

(b)

Figure 4.3: (a) PL spectrum of the positive trion X^+ state in a Mn-doped InGaAs QD studied in this chapter (QD6) under non-resonant optical excitation at 1.34 eV. (b) Schematic representation of the levels of this positively charged QD6. Resonant laser is scanning the transitions from level $|2\rangle$, while the PL signal is measured for the transitions toward level $|4\rangle$.

Fig. 4.3b illustrates the energy level diagram of this positively charged QD. In this chapter, we address the Autler-Townes effect by focusing on the V-type system consisting of the transitions $|2\rangle \rightarrow |1\rangle$ and $|2\rangle \rightarrow |3\rangle$. In a single-laser experiment, the laser scans through these two transitions, with its detuning from the $|2\rangle \rightarrow |1\rangle$ transition defined as δ_L. We monitor the populations of levels $|1\rangle$ and $|3\rangle$ by observing the PL signal due to the optical recombination to the spectator state (level $|4\rangle$). In this way, for a sufficiently strong resonant laser (with respect to the spectral resolution of the PL setup), we can measure the AT splitting of the dressed states, successively for the $|2\rangle \rightarrow |1\rangle$ and $|2\rangle \rightarrow |3\rangle$ transitions.

In that respect, the significant splitting between levels $|1\rangle$ and $|4\rangle$ provides an advantage for further filtering of reflected laser light. In addition to the effective rejection of reflected laser light achieved by our dark microscope setup, excitation with a high-power resonant laser requires the use of a double spectrometer. Since the resonantly excited transitions (FM doublet) are blueshifted by $\Delta \approx 700$ µeV compared to the measured PL (AFM doublet), the resonant laser can be effectively filtered out from the measured PL spectrum by the intermediate slit of the double spectrometer. This enables us to measure the PL signal for the AFM doublet even at very high laser powers (up to 1 mW).

A series of photoluminescence (PL) spectra for detection energies around the transitions $|1\rangle \rightarrow |4\rangle$ and $|3\rangle \rightarrow |4\rangle$ is recorded as a function of the laser detuning and presented in the form of an intensity map. Several such plots, corresponding to different powers of the resonant laser, are shown in Fig. 4.4. Two lines corresponding to the transitions to level $|4\rangle$ are observed even when the laser is detuned. This is due to the non-resonant excitation with He-Ne laser at 1.95 eV, which is used to keep the QD charged with a single hole. The power of this non-resonant laser is relatively small (a few µW) and is adjusted to maximize the PL signal for positive trion state.

For the lowest power of the resonant laser, which is 0.4 µW (Fig. 4.4a), two small increases in intensities are observed when the laser is resonant with the transition $|1\rangle \rightarrow |4\rangle$ ($\delta_L = 0$) or $|3\rangle \rightarrow |4\rangle$ ($\delta_L = 144$ µeV). The resonance linewidth is approximately 17 µeV. This linewidth is smaller than the one measured in section 2.3 for a resonant laser power of 80 µW, but still significantly broader than the natural linewidth of InGaAs QDs. As the laser power increases, the resonance linewidth also increases, reaching about 40 µeV when the laser power is 110 µW (Fig. 4.4c). A diagonal line corresponding to the Stokes Raman line can also be observed between the two resonances, similar to what was observed in section 2.3. At very high laser powers (> 300 µW), it becomes possible to directly observe the AT effect for both transitions from the levels $|1\rangle$ and $|3\rangle$ to the level $|4\rangle$. As seen in Fig. 4.4d for a resonant laser power of 810 µW, the AT splitting is clearly observed when the laser is resonant with these transition, corresponding to the Rabi frequency Ω_R. The AT splitting is visibly larger when the $|2\rangle \rightarrow |3\rangle$ transition is dressed compared to the splitting observed for the $|2\rangle \rightarrow |1\rangle$ dressed transition. This difference between Ω_3 and Ω_1 arises from different dipole strengths (or couplings g) associated with these two transitions.

4.2.2 Model based on the optical Bloch equations

To gain a better understanding of the evolution of resonance linewidth with laser power and difference in AT splittings Ω_1 and Ω_3, we have developed a model based on the optical Bloch equations (OBE) to describe these experimental observations. Spontaneous emission in optically driven three-level systems with V, Λ, and cascade configurations has already been described in quantum optics textbooks [109–111]. In our experiment, the resonant laser drives the $|2\rangle \rightarrow |1\rangle$ and $|2\rangle \rightarrow |3\rangle$ transitions,

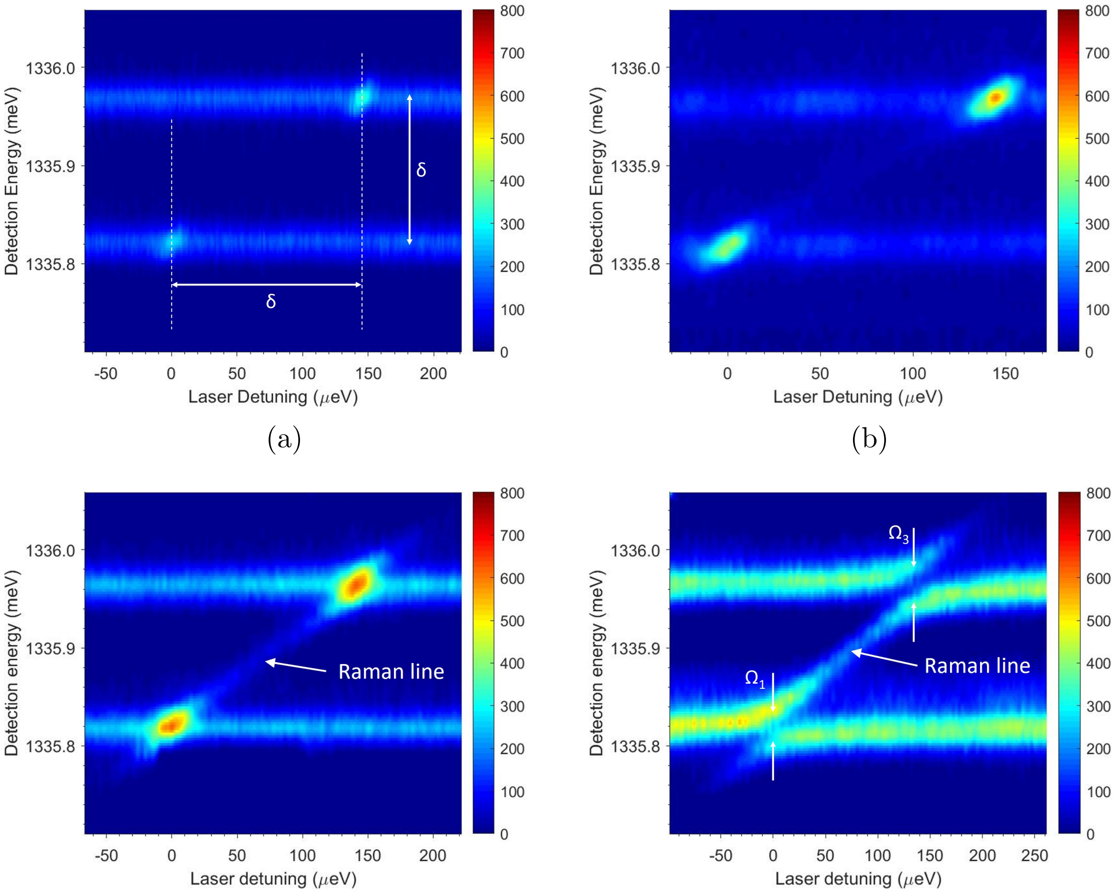

(a) (b)

(c) (d)

Figure 4.4: Intensity maps of μPL emission as a function of resonant laser detuning δ_L and detection energy. Measurements were performed at different laser powers: (a) 0.4 μW, (b) 16 μW, (c) 110 μW and (d) 810 μW. Colorbars indicate PL intensity per pixel while the acquisition times are 15 s, 10 s, 8 s and 10 s, respectively. To improve the quality of these images, an interpolation function was used on the original experimental data.

allowing us to consider a V-type three-level system. The fourth level, $|4\rangle$, is used to observe the PL signal for transitions from the excited state. As it does not coherently interact with other states, we can consider it as an open V-type system [112] and introduce level $|4\rangle$ at the end.

We start by considering more general situation discussed in the quantum optics textbooks [109–111] when the V-like system is driven by two lasers, as presented in Fig. 4.5. The two lasers drive the transitions $|2\rangle \rightarrow |1\rangle$ and $|2\rangle \rightarrow |3\rangle$ with frequencies ω_1 and ω_3 (green and red arrows in Fig. 4.5). The strength with which these transitions are driven depends on the Rabi frequencies Ω_1 and Ω_3, as well as their detunings from these levels, δ_1 and δ_3. Detunings are defined as $\delta_1 = \omega_{12} - \omega_1$ and $\delta_3 = \omega_{32} - \omega_3$, where ω_{12} and ω_{32} are the frequencies of these transitions. In the dipolar and rotating-wave approximations, the semiclassical Hamiltonian of the system in the interaction picture

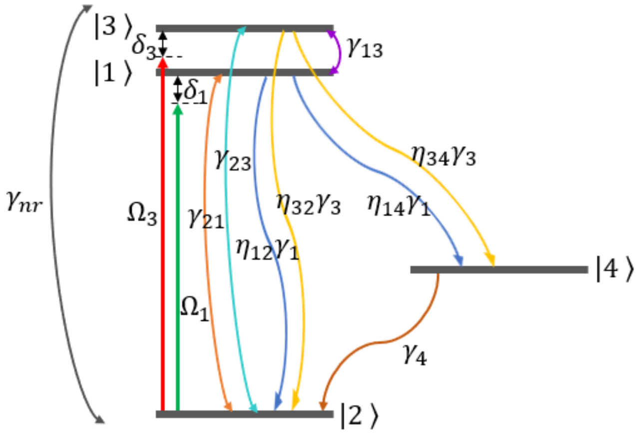

Figure 4.5: Schematic representation of the processes described by OBE model for positively charged QD6.

can be written as follows:

$$H = \hbar\delta_1|1\rangle\langle 1| + \hbar\delta_3|3\rangle\langle 3| + \hbar\Delta|4\rangle\langle 4| + \frac{\hbar}{2}\Omega_1(|1\rangle\langle 2| + |2\rangle\langle 1|) + \frac{\hbar}{2}\Omega_3(|3\rangle\langle 2| + |2\rangle\langle 3|) \tag{4.8}$$

The evolution of the density matrix ρ can then be obtained using a master equation in Lindblad form [109]:

$$\frac{\partial\rho}{\partial t} = -\frac{i}{\hbar}[H,\rho] + i\hbar\sum_k\left(L_k\rho L_k^\dagger - \frac{1}{2}\{L_k^\dagger L_k,\rho\}\right) \tag{4.9}$$

The coherent evolution of the system is described by the Hamiltonian, while the irreversible processes are taken into account by the Lindblad collapse operators for the spontaneous emission ($L_{12} = \sqrt{\eta_{12}\gamma_1}|2\rangle\langle 1|$, $L_{14} = \sqrt{\eta_{14}\gamma_1}|4\rangle\langle 1|$, $L_{32} = \sqrt{\eta_{32}\gamma_3}|2\rangle\langle 3|$, $L_{34} = \sqrt{\eta_{34}\gamma_3}|4\rangle\langle 3|$), the spin relaxation ($L_{42} = \sqrt{\gamma_4}|2\rangle\langle 4|$), the non-resonant laser excitation ($L_{21} = \sqrt{\gamma_{nr/2}}|1\rangle\langle 2|$, $L_{23} = \sqrt{\gamma_{nr/2}}|3\rangle\langle 2|$, $L_{41} = \sqrt{\gamma_{nr/2}}|1\rangle\langle 4|$, and $L_{43} = \sqrt{\gamma_{nr/2}}|3\rangle\langle 4|$), and the pure dephasing ($L_{11} = \sqrt{\Gamma_{31}}|1\rangle\langle 1|$ and $L_{33} = \sqrt{\Gamma_{31}}|3\rangle\langle 3|$).

The set of density matrix equations can then be written as:

$$\dot\rho_{11} = -\gamma_1\rho_{11} - i\frac{\Omega_1}{2}(\rho_{21} - \rho_{12}) + \frac{\gamma_{nr}}{2}(\rho_{22} + \rho_{44}) \tag{4.10}$$

$$\dot\rho_{33} = -\gamma_3\rho_{33} - i\frac{\Omega_3}{2}(\rho_{23} - \rho_{32}) + \frac{\gamma_{nr}}{2}(\rho_{22} + \rho_{44}) \tag{4.11}$$

$$\dot\rho_{32} = -(\gamma_{23} - i\delta_3)\rho_{32} - i\frac{\Omega_3}{2}(\rho_{22} - \rho_{33}) + i\frac{\Omega_1}{2}\rho_{31} \tag{4.12}$$

$$\dot\rho_{21} = -(\gamma_{21} + i\delta_1)\rho_{21} - i\frac{\Omega_1}{2}(\rho_{11} - \rho_{22}) - i\frac{\Omega_3}{2}\rho_{31} \tag{4.13}$$

$$\dot\rho_{31} = -(\gamma_{31} + i(\delta_1 - \delta_3))\rho_{31} - i\frac{\Omega_3}{2}\rho_{21} + i\frac{\Omega_1}{2}\rho_{32} \tag{4.14}$$

$$\dot\rho_{23} = \dot\rho_{32}^* \tag{4.15}$$

$$\dot{\rho}_{12} = \dot{\rho}_{21}^{*} \tag{4.16}$$

$$\dot{\rho}_{13} = \dot{\rho}_{31}^{*} \tag{4.17}$$

$$\rho_{11} + \rho_{22} + \rho_{33} + \rho_{44} = 1 \tag{4.18}$$

$$\rho_{44} = \frac{\gamma_1}{\gamma_4 + \gamma_{nr}}\eta_{14}\rho_{11} + \frac{\gamma_3}{\gamma_4 + \gamma_{nr}}\eta_{34}\rho_{33} \tag{4.19}$$

The diagonal elements ρ_{ii} represent the probabilities of being in the $|i\rangle$ state, while the off-diagonal elements ρ_{ij} describe the coherence between $|i\rangle$ and $|j\rangle$ levels. Non-resonant laser excitation is introduced through the term $\frac{\gamma_{nr}}{2}(\rho_{22} + \rho_{44})$, describing the excitation of the electron from the ground state levels $|2\rangle$ and $|4\rangle$ to the excited state. The coherence dampings γ_{ij} are given by:

$$\gamma_{21} = \frac{\gamma_1}{2} + \frac{\gamma_{nr}}{2} + \frac{\Gamma_{31}}{2} \tag{4.20}$$

$$\gamma_{23} = \frac{\gamma_3}{2} + \frac{\gamma_{nr}}{2} + \frac{\Gamma_{31}}{2} \tag{4.21}$$

$$\gamma_{31} = \frac{\gamma_1}{2} + \frac{\gamma_3}{2} + \Gamma_{31} \tag{4.22}$$

where γ_i represents the population decay rate for state $|i\rangle$, and Γ_{31} is a pure dephasing rate.

Parameters η_{12}, $\eta_{14} = 1 - \eta_{12}$, η_{32} and $\eta_{34} = 1 - \eta_{32}$ describe possible different branching ratios of the emission toward level $|4\rangle$ with respect to the emission toward level $|2\rangle$. Since all four lines in the PL spectrum of this QD (Fig. 4.3a) have nearly the same intensity, one would expect these parameters to be 0.5. However, to accurately model the measurements, it is useful to introduce theses parameters which will be slightly adjusted to fit the experimental data.

As shown in Fig. 4.5, this model describes the case when two lasers excite resonantly 2 transitions of V-like system. To use this model when a single laser scans through these transitions, we just have to consider that $\omega_1 = \omega_3$ or equivalently that $(\delta_3 = \delta_L - \delta_0)$ and that the Rabi frequencies are given by the same laser power P differing thus only by the strength of the interband dipoles, namely $\Omega_1 = k_1\sqrt{P}$ and $\Omega_3 = k_3\sqrt{P}$. Solving together the equations for both driven transitions is necessary to properly simulate the Raman line in the region between the two transitions in Fig. 4.4d when the laser is out of resonance for both transitions. The coefficients k_1 and k_3 can be determined from the AT splittings measured at high laser powers (Fig. 4.4d) as shown in the detailed analysis presented in section 4.2.4. The values used in all the simulations are $k_1 = 41$ µeV/$\sqrt{\text{mW}}$ and $k_3 = 49$ µeV/$\sqrt{\text{mW}}$. Additionally, in the case of single resonant laser excitation, we can neglect the coherence between levels $|1\rangle$ and $|3\rangle$ $(\rho_{13} = \rho_{13} = 0)$. The equations (4.10-4.19) are then solved in steady state $(\dot{\rho} = 0)$.

The PL intensity coming from the $|1\rangle \rightarrow |4\rangle$ ($|3\rangle \rightarrow |4\rangle$) transition is proportional to the spontaneous emission rate from the level ρ_{11} (ρ_{33}) given by $PL_{14} = \eta_{14}\gamma_1\rho_{11}$ ($PL_{34} = \eta_{34}\gamma_3\rho_{33}$) obtained by solving the density matrix equations. To reproduce the resonance linewidth dependence on laser power (characterized by a moderate power broadening), it is also essential to introduce inhomogeneous broadening to this model. This is done by performing the convolution of the function $PL_{14}(\delta_L)$ and $PL_{34}(\delta_L)$ with a Gaussian distribution with FWHM= 16 µeV. The origin of this inhomogeneous broadening is ascribed to spectral diffusion, likely due to DC Stark effect originating from the fluctuating local electric fields produces by trapped charges around a QD [113, 114]. In our case, we consider that it results in a rigid shift of levels $|1\rangle$ and $|3\rangle$ with respect to levels $|2\rangle$ and $|4\rangle$, which is reflected in the same shift in emission. As a noticeable result, the Stokes Raman line observed in our measurements is not affected by spectral diffusion since it depends only on the splitting Δ between levels $|2\rangle$ and $|4\rangle$, which is considered constant.

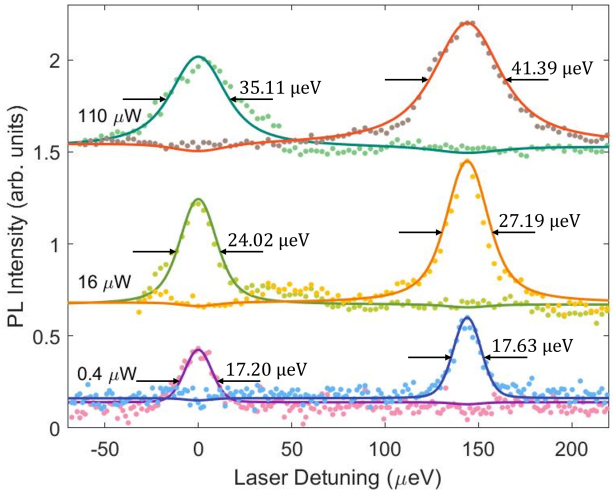

Figure 4.6: Integrated PL intensities for transitions $|1\rangle \rightarrow |4\rangle$ and $|3\rangle \rightarrow |4\rangle$ as function of laser detuning. Points represent experimental data, while solid lines are fits generated by the model. Resonant laser powers and FWHM of model peaks are also indicated.

To apply this model to the first three measurements presented in Fig. 4.4, we first extract the integrated intensities of $|1\rangle \rightarrow |4\rangle$ and $|3\rangle \rightarrow |4\rangle$ transitions from these data. Then, we numerically solve the density matrix equations to obtain the best fit of the experimental points (Fig. 4.6) by taking as free parameters γ_1, γ_3, γ_4, Γ_{31} and γ_{nr}. The decay rate from level $|3\rangle$ is set close to the characteristic radiative lifetime of InGaAs QDs of ≈ 0.8 ns ($\gamma_3 = 0.8$ µeV [1]). The decay rate from level $|1\rangle$ is taken proportional to γ_3 with a factor given by $(k_1/k_3)^2$ which represents the ratio of oscillator strengths, so that $\gamma_1 = 0.54$ µeV. The decay rate from level $|4\rangle$ that provides a good fit of experimental data is $\gamma_4 = 0.04$ µeV. The parameter that describes the non-resonant laser excitation rate γ_{nr} is adjusted for each of the three measurements since the power of He-Ne laser was different in these measurements and since at high power the resonant laser is also susceptible to generate some non-resonant excitation (through processes like 2-photon absorption and Auger effect). The linewidth evolution as a function of the power is predominantly determined by the dephasing mechanisms described by the rates γ_{21} and γ_{23} which include the homogeneous pure dephasing term Γ_{31}. If we take Γ_{31} larger than a few 100 neV, the resonance linewidths increase too rapidly with the laser power. For this reason, this parameter, which has no other impact on the single-laser resonance spectra, is set here to $\Gamma_{31} = 0.2$ µeV. Finally, the branching

---

[1] All rates γ are given in units of their corresponding energy width $\hbar\gamma$.

ratios η_{14} and η_{34}, which have to remain close to 0.5, are finely adjusted to improve the fitting. The retained values are $\eta_{14} = 0.49$ and $\eta_{34} = 0.51$. As seen in Fig. 4.6, the model matches the experimental data quite well for all three measurements. The resonance linewidth increases moderately with the laser power, in agreement with the experimental observations. At low power, the linewidth is about 17 µeV, meaning it is almost completely determined by the inhomogeneous broadening (16 µeV). Noticeably, the linewidth for the $|3\rangle \rightarrow |4\rangle$ transition is also larger than that of the $|1\rangle \rightarrow |4\rangle$ transition, which is predominantly the effect of larger coefficient k_3 in Rabi frequency for the $|3\rangle \rightarrow |4\rangle$ transition.

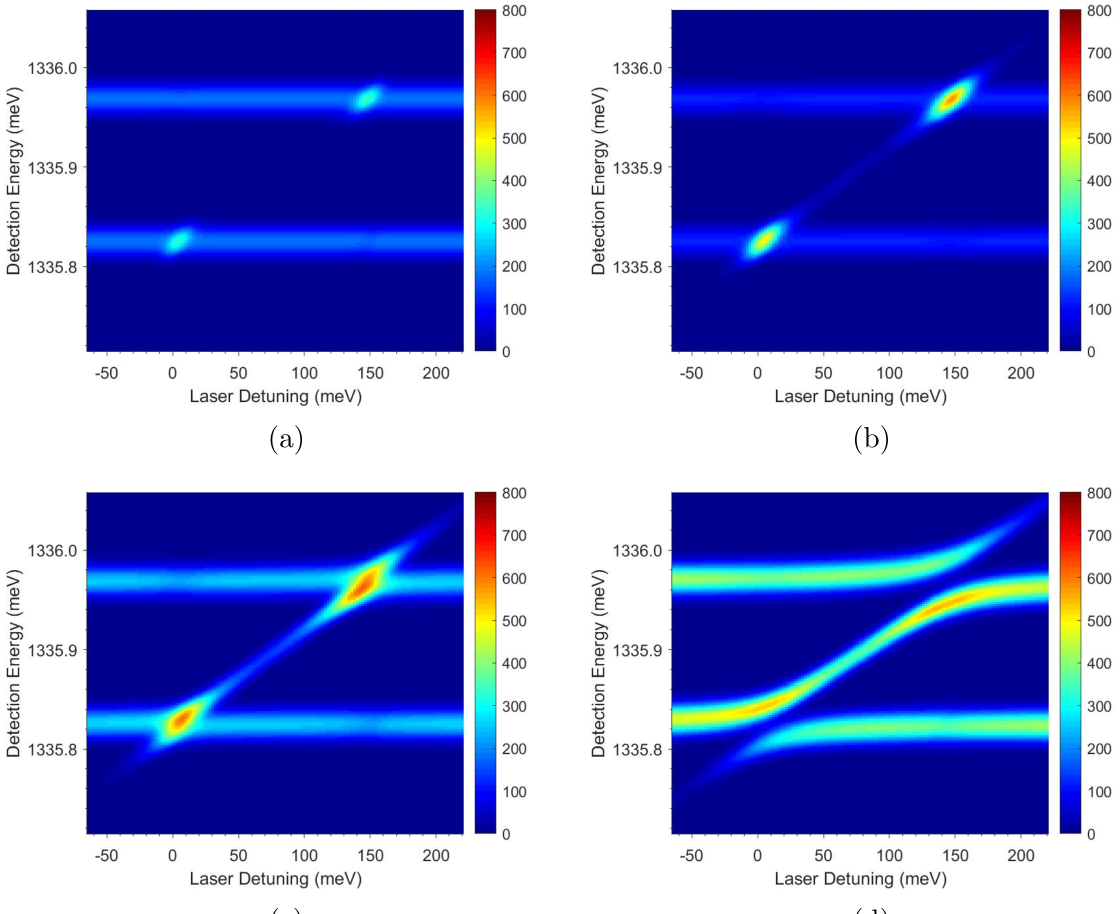

(a)

(b)

(c)

(d)

Figure 4.7: Intensity maps of simulated µPL spectra as a function of resonant laser detuning δ_L and detection energy. Calculations were performed using the previously determined parameters and for the same laser powers as in the experiment: (a) 0.4 µW, (b) 16 µW, (c) 110 µW and (d) 810 µW. The simulation data have been multiplied by constants to roughly adjust the intensity to match the experimental data.

Solutions of the OBE, can be used not only to calculate the total intensity but also to determine the PL spectrum, employing the Wiener-Khintchine theorem. Using the same parameters as determined above, the goal was to calculate the PL intensity maps corresponding to the conditions from the measurements in Fig. 4.4, notably to reproduce the emergence of the Autler-Townes splitting at high excitation power. For the specific part of the PL spectrum around the transitions $|1\rangle \to |4\rangle$ and $|3\rangle \to |4\rangle$, the Wiener-Khintchine theorem gives:

$$\begin{aligned} I_{PL}(\omega) \propto Re \int_0^\infty & [\gamma_1\langle\hat{\sigma}_{14}(0)\hat{\sigma}_{41}(\tau)\rangle + \gamma_3\langle\hat{\sigma}_{34}(0)\hat{\sigma}_{43}(\tau)\rangle \\ & - \sqrt{\gamma_1\gamma_3}\langle\hat{\sigma}_{14}(0)\hat{\sigma}_{43}(\tau)\rangle - \sqrt{\gamma_1\gamma_3}\langle\hat{\sigma}_{34}(0)\hat{\sigma}_{41}(\tau)\rangle]e^{i\omega\tau}d\tau \end{aligned} \tag{4.23}$$

where we use the notations $\hat{\sigma}_{ij} \equiv |i\rangle\langle j|$. Subsequently, the quantum regression theorem is invoked to carry out the calculation of the averaged time-dependent correlations in the sum, as explained in Appendix A. Finally, to simulate the experimental results, it is necessary to include spectral diffusion and spectral resolution of the setup. This was done by performing two convolutions of I_{PL} with appropriate Gaussian distributions. All these steps are explained in more details in Appendix A, a work performed in close collaboration with the group of Prof. Shilpi Gupta from the Indian Institute of Technology of Kanpur, India. These simulated spectra are presented in Fig. 4.7. They show very good agreement with the experimental plots, confirming the validity of the model and of the chosen parameters. Notably, this model describes very well the observed Stokes Raman line which somehow anti-crosses with the PL lines resulting from the non-resonant excitation. Similar to the experimental data, the simulated spectra reveal that the AT splitting is observable only at high laser powers due to the finite spectral resolution of the setup. Additionally, the Raman line intensity which is maximum in between the resonances is well reproduced thanks to a proper definition of the four involved dipolar matrix elements as discussed in Appendix A.

4.2.3 Modelling QD1 from Section 2.3.2

Having developed a model that explains the experimental data well for a range of resonant laser powers, we can revisit the results presented in section 2.3.2. In that section, we presented measurements for a positively charged Mn-doped QD1 in the sample with a Schottky diode. At that time, we did not perform a comprehensive set of measurements for different laser powers due to less counts collected at low power and the considerable amount of stray light because a simple spectrometer was used. This made the development of a rigorous model unnecessary and less beneficial at that point. Using the successful model presented in this chapter and starting with the values of parameters determined above, we attempt to find a good fit for the integrated intensities of transitions $|1\rangle \to |4\rangle$ and $|3\rangle \to |4\rangle$ presented in Fig. 2.16b.

Firstly, this QD1 exhibits significant differences in the intensities of its four peaks. The branching ratios calculated from the PL intensities in Fig. 2.14a are $\eta_{14} = 0.68$ and $\eta_{34} = 0.32$. The decay rate γ_3 is adjusted to be close to the previous value $\gamma_3 = 0.9$ µeV, while $\gamma_1 = 0.74$ µeV is taken to be proportional to γ_3 with a factor given by the ratio of oscillator strengths ($(k_1/k_3)^2$). In addition to the inhomogeneous broadening defined by a Gaussian with FWHM= 16 µeV, a small pure dephasing is introduced, $\Gamma_{31} = 0.4$ µeV.

The crucial parameters for reproducing the resonance linewidths and observed dips are Rabi frequencies Ω_1 and Ω_3 and decay rate γ_4. Since we do not have a strong laser measurement where AT splittings are resolved, we determine the values of coefficients k_1 and k_3 by looking for the best fit of linewidths for laser power $P = 80$ µW. We find that $k_1 = 59$ µeV/$\sqrt{\text{mW}}$ and $k_3 = 70$ µeV/$\sqrt{\text{mW}}$ give the best results. These values are significantly larger than those observed for QD6. This is likely attributed to the lower emission wavelength of QD1, suggesting a larger quantum dot size and a higher electron-hole dipole. An important feature of this measurement is the decrease in PL signal from level $|1\rangle$ ($|3\rangle$) when the laser is resonant with the transition $|2\rangle \rightarrow |3\rangle$ ($|2\rangle \rightarrow |1\rangle$). To reproduce these two dips, it is necessary to manually choose a much larger γ_4 parameter than for the QD6. The value used here is $\gamma_4 = 0.9$ µeV. The obtained model fits the experimental data quite well, as illustrated in Fig. 4.8.

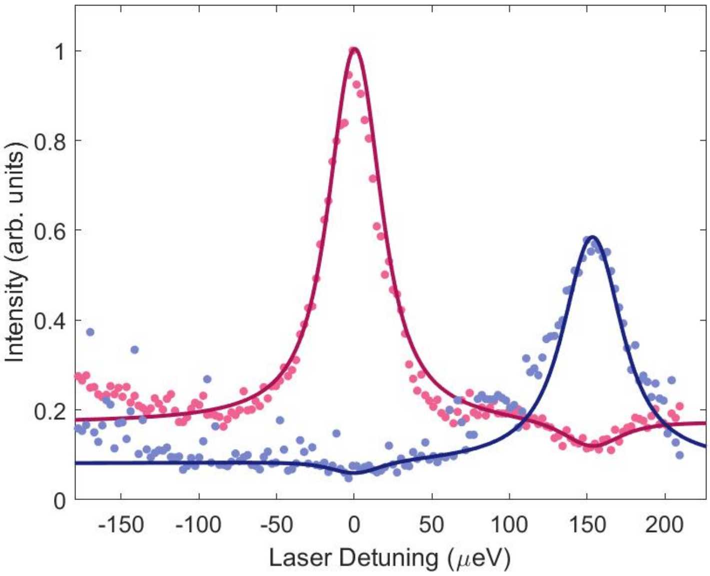

Figure 4.8: Integrated PL intensities for transitions $|1\rangle \rightarrow |4\rangle$ and $|3\rangle \rightarrow |4\rangle$ as function of laser detuning for the QD1 described in section 2.3.2 for laser power of 80 µeV. Points represent experimental data, while solid lines are fits generated by the model.

For fitting the measurements in Fig. 4.6 for that quantum dot (QD6), we have used $\gamma_4 = 0.04$ µeV. This corresponds to a spin relaxation time of T_1^{QD6} =16.4 ns. The value obtained for the QD in the Schottky diode sample (QD1) is T_1^{QD1} =0.73 ns. This indicates much quicker spin relaxation from level $|4\rangle$ to level $|2\rangle$. These two QDs also have different splittings between the levels $|4\rangle$ and $|2\rangle$. Therefore, the relation between their spin relaxation times and splittings can be described as:

$$\frac{T_1^{QD6}}{T_1^{QD1}} = \left(\frac{\Delta^{QD6}}{\Delta^{QD1}}\right)^{\alpha} \tag{4.24}$$

where the splittings are $\Delta^{QD6} = 0.7$ meV and $\Delta^{QD1} = 1.3$ meV. The calculated value of the exponent is $\alpha = -5.03$.

It has been reported in Ref. [115] that the spin-flip transitions between Zeeman levels in QDs can be mediated by one-phonon scattering processes at low temperatures ($k_B T < g_e \mu_B B$). The characteristic dependence of spin relaxation time for such processes is $T_1 \propto B^{-5}$. For our Mn-doped QD, there is an intrinsic splitting of FM and AFM levels. This splitting is proportional to the Zeeman splitting produced by the magnetic field B. Therefore, the relation $T_1 \propto \Delta^{\alpha}$ with the exponent $\alpha = -5.03$ is consistent with the behaviour reported in the literature. With the increase of splitting Δ between levels $|4\rangle$ and $|2\rangle$ for QD1, the spin relaxation time is decreasing compared to the on observed for QD6. The short time related to the relaxation from AFM to FM level of $h - A^0$ is probably a result of fast relaxation of neutral acceptor A^0 spin.

4.2.4 Autler-Townes splitting

We have observed that as the resonant laser power increases, the resonance linewidth also increases. With sufficiently strong resonant excitation, it becomes possible to resolve the AT splitting. In this section, we focus on the analysis of measurement performed with a strong laser power of $P = 810$ µeV. From the measurement in Fig. 4.4d, we have extracted the energy positions of the three spectrally resolved transitions, namely the $|1\rangle \rightarrow |4\rangle$ and $|3\rangle \rightarrow |4\rangle$ transitions as well as the Raman line. Using the eigenvalues obtained in Appendix A, we can calculate the corresponding energies as a function of laser detuning, and determine the values of Ω_1 and Ω_3 necessary to reproduce the experimental anticrossings. These results (solid lines) are presented in Fig. 4.9a and show an excellent agreement with the experimental data (dots). Two AT splittings are clearly observed when the laser is resonant with the $|2\rangle \rightarrow |1\rangle$ transition ($\delta_L = 0$ µeV) and with the $|2\rangle \rightarrow |3\rangle$ transition ($\delta_L = 144$ µeV).

Fig. 4.9b provides a closer view of the resonance observed in the PL signal of the $|3\rangle \rightarrow |4\rangle$ transition, corresponding to the marked square in Fig. 4.9a. This behavior is typical for AT splitting [105]. The experimental points and model curves correspond to dressed states $|I, N\rangle$ and $|II, N\rangle$, as defined in Fig. 4.1. They form a hyperbola-like traces with asymptotes representing the uncoupled states $|a, N\rangle$ and $|b, N+1\rangle$. When the light-matter interaction is neglected, these uncoupled states cross at a laser detuning $\delta_L = \delta_0$ (resonance with the $|2\rangle \rightarrow |3\rangle$ transition). However, taking light-matter interaction into account results in the dressed states and their anticrossing, i.e., the AT splitting, at $\delta_L = \delta_0$. For large laser detunings ($|\delta_L - \delta_0| \gg \Omega_1$), dressed states asymptotically approach the uncoupled states. The distance between the dressed states and the corresponding asymptote results in the energy shift of the transition, also known as the AC Stark shift or optical Stark shift.

From the data presented in Fig. 4.9a, we can extract the splitting of these dressed states and plot it for both transitions to level $|4\rangle$ as a function of laser detuning. These results are presented in Fig. 4.9c, and they show good agreement with the model. From Fig. 4.9c, we can extract values of Rabi frequencies Ω_1 and Ω_3 at the resonances, $\Omega_1 = 36.5$ µeV and $\Omega_3 = 43.7$ µeV. The splitting corresponding to the $|3\rangle \rightarrow |4\rangle$ transition is larger, as expected from Fig. 4.4d. The parameters k_1 and k_3 are then deduced from these experimental values of Ω_1 and Ω_3. In this way, we obtain $k_1 = 41$ µeV/$\sqrt{\text{mW}}$ and $k_3 = 49$ µeV/$\sqrt{\text{mW}}$. This measurement with strong laser excitation allows us to precisely determine the values of these coefficients k_1 and k_3, which are then used in all calculations for this QD.

It can also be noticed that the minimum splitting for level $|3\rangle$ is observed at $\delta_L = 137$ µeV. This corresponds to the detuning when the laser is actually in resonance with the transition $|2\rangle \rightarrow |3\rangle$. According to the energy diagram of levels for this QD, one would expect resonance to occur when $\delta_L = \delta_0 = 144$ µeV. This redshift of resonance

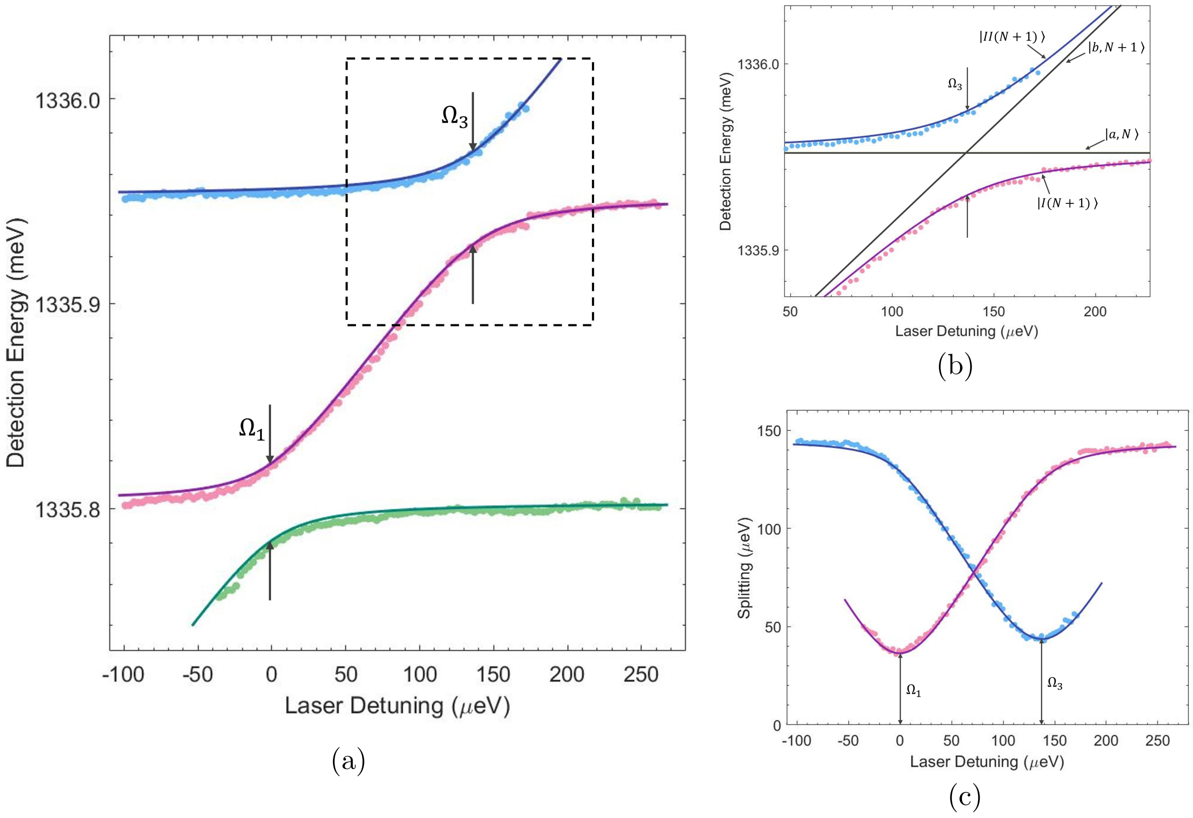

(a)

(b)

(c)

Figure 4.9: (a)Spectral position of two Autler-Townes doublets as a function of laser detuning. Experimental data (dots) are fitted with a theoretical model (solid lines). (b) Magnified view of the spectral position of Autler-Townes doublet related to $|3\rangle \rightarrow |4\rangle$ transition. Black lines represent uncoupled states. (c) Splitting for two observed Autler-Townes doublets as a function of laser detuning.

is not observed for lower powers in Fig. 4.4a-4.4c, and it could be due to the AC Stark shift induced by the strong laser as it scans energies before reaching level $|3\rangle$.

4.2.5 Power dependance of Autler-Townes splitting

The AT effect observed at high laser power was examined in more detail in a separate measurement. In this experiment, we fixed the resonant laser at the transition $|2\rangle \rightarrow |3\rangle$ and measured a series of spectra for a range of resonant laser powers, ranging from 15 µW to 1.15 mW. For that purpose in the software control of the Toptica DLC laser, we use the option to set a geometric progression for defining the series of powers. Additionally, the good stability of this laser makes it possible to change its power while the wavelength stays fixed.

The AT splitting is known to be proportional to the square root of laser power [109]. Therefore, the measured spectra are presented in Fig. 4.10a in the form of an intensity map as a function of $\sqrt{P}$. With sufficiently strong laser excitation, it becomes possible to resolve the AT splitting. The AT splittings extracted for these powers are plotted in Fig. 4.10b. The line with a slope of $k_3 = 48.86$ µeV/$\sqrt{\text{mW}}$ provides an excellent fit to the experimental data, confirming the linear dependence of Ω_3 on $\sqrt{P}$. The

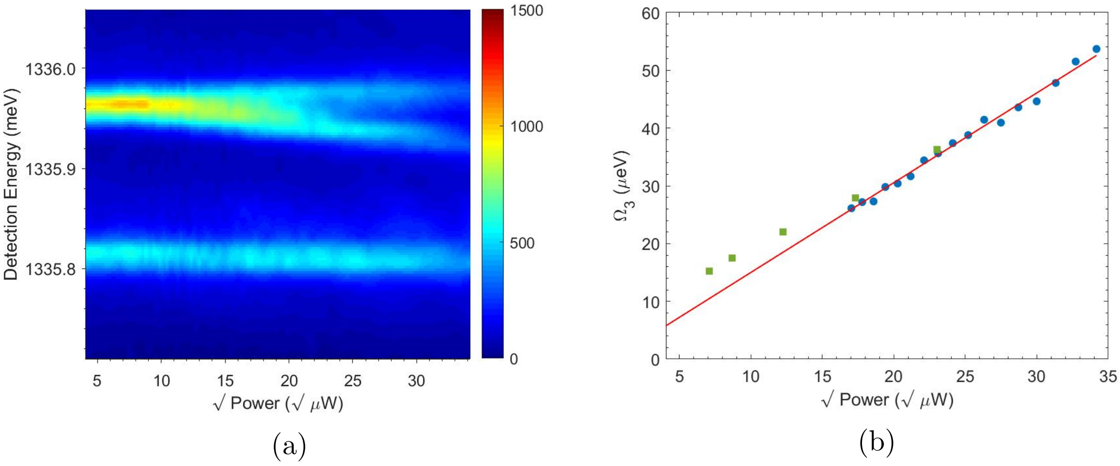

Figure 4.10: (a) Intensity map of μPL emission as a function of $\sqrt{P}$ with the laser fixed at $|2\rangle \rightarrow |3\rangle$ transition. To improve the quality of the image, the interpolation function was used. (b) Dependence of AT splitting Ω_3 on $\sqrt{P}$. The blue points are extracted from the measured spectra, while the green squares represent values that will be extracted from the two-laser measurement in the following section.

extracted coefficient k_3 is in good agreement with the value determined previously from the model in the measurement at a single power ($P = 810$ μeV).

As observed, direct measurement of AT splitting is not possible at powers lower than $\approx$ 290 μW, when the splitting is comparable to the spectral resolution plus spectral diffusion. Therefore, we developed a different approach to investigate this AT splitting in lower power regime.

4.3 Two-laser probing of Autler-Townes and quantum interference effects

4.3.1 Two-Laser Autler-Townes splitting analysis

Conducting the two-laser experiment enables the investigation of AT splitting at lower laser powers. For that purpose, a fixed, strong power laser (pump) resonantly excites the transition $|2\rangle \rightarrow |3\rangle$. The Rabi frequency induced by this laser is $\Omega_3 \sim \sqrt{P_3}$. The corresponding dressed states are separated by the AT splitting defined by this Rabi frequency Ω_3. The second laser (probe) scans the transition $|2\rangle \rightarrow |1\rangle$. Its detuning from this transition is δ_L, and its Rabi frequency is $\Omega_1 \sim \sqrt{P_1}$. The power of this laser is typically one order of magnitude lower than that of the fixed laser. Using this second laser allows us to probe the AT splitting of the ground state $|2\rangle$.

For the powers of the fixed and scanning lasers $P_3 = 50$ μeV and $P_1 = 5$ μeV, a series of PL spectra is recorded for different probe detunings δ_L and presented in Fig. 4.11b. The line at a higher energy (stronger intensity) corresponds to the PL signal from transition $|3\rangle \rightarrow |4\rangle$. Despite the broadening observed in this line, the AT splitting is not spectrally resolved in the PL spectra at this power. The other line corresponds

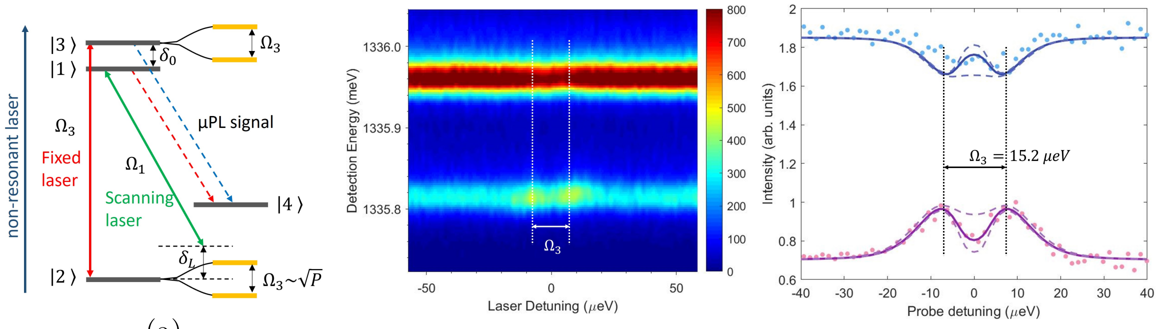

(a) (b) (c)

Figure 4.11: (a) Schematic representation of two-laser experiment, where strong laser (pump) resonantly excites transition $|2\rangle \to |3\rangle$ and weaker laser (probe) is scanning through $|2\rangle \to |1\rangle$ transition. PL signal is measured for the transitions toward level $|4\rangle$. (b) Intensity map of PL emission as a function of probe detuning measured in two-laser experiment where the fixed and scanning laser powers are $P_3 = 50$ µW and $P_1 = 5$ µW, respectively. (c) Integrated PL intensity for the same measurement of transition $|1\rangle \to |4\rangle$ (purple dots) and $|3\rangle \to |4\rangle$ (blue dots). Solid lines represent model fit when $\Gamma_{31} = 0.4$ µeV, while dashed lines correspond to the case when $\Gamma_{31} = 0$ µeV or $\Gamma_{31} = 3$ µeV.

to PL signal measured for the transition $|1\rangle \to |4\rangle$. The excitation spectrum of this transition shows a doublet centered around $\delta_L = 0$ (probe resonant with transition $|2\rangle \to |1\rangle$). The distance between the two peaks of the doublet corresponds to AT splitting Ω_3. At the same position of this doublet, a small decrease in intensity can be observed for the PL of the transition $|3\rangle \to |4\rangle$.

To analyze the generated AT effect more closely, the integrated PL intensities for transitions $|1\rangle \to |4\rangle$ and $|3\rangle \to |4\rangle$ are extracted and shown in Fig. 4.11c. We use the model defined by Eq. 4.10-4.22 to analyse quantitatively these experimental data. In contrast to the case of single-laser excitation, here we neglect the effect of the laser which is not close in energy to a given transition. This approximation is justified by the fact that $\delta_0 >> \Omega_i$. Rabi frequencies Ω_1 and Ω_3 now refer to different lasers driving two different transition. The detunings in these equations are then defined as $\delta_3 = 0$ and $\delta_1 = \delta_L$. We also keep the coherence between levels $|1\rangle$ and $|3\rangle$ induced by the two-laser probing ($\rho_{13} = \rho_{31} \neq 0$). The other used parameters are similar to previously: $\gamma_1 = 0.58$ µeV, $\gamma_3 = 0.8$ µeV and $\gamma_4 = 0.04$ µeV. The branching ratios are adjusted to reproduce the correct difference in signal between the two transitions $|1\rangle \to |4\rangle$ and $|3\rangle \to |4\rangle$. The values taken here are $\eta_{14} = 0.52$ and $\eta_{34} = 0.48$. These values are slightly different from the ones used for the single-laser experiment. The difference might arise due to small variations in the collection efficiencies of each particular transitions when precise focusing conditions are changed. This can result in somewhat larger branching rations for certain QD transitions. This is indeed the case here, as the measurements with two-laser excitation were performed a few months after the initial experiments with single-laser. In addition, for the set of measurements taken under the same focusing conditions, we can in fact use the same constant parameters.

For the pure dephasing we use $\Gamma_{31} = 0.4$ µeV. The generated curves fit the experimental data well. The choice of the pure dephasing parameter Γ_{31} is important to reproduce the dip between the two peaks. If Γ_{31} is set to zero, the dip is very pronounced, while when Γ_{31} is set to 3 µeV, the dip is barely observable. Both cases are included in Fig. 4.11c as dashed lines. When Γ_{31} is large, it destroys the coherence between states $|1\rangle$ and $|3\rangle$. On the other hand, for $\Gamma_{31} = 0$ µeV, there is coherence between states $|1\rangle$ and $|3\rangle$. A deeper dip indicates that in this case, only a part of its depth is due to the incoherent effects, while the coherent processes play a significant role in its depth [112]. The fact that we are able to observe the AT effect when probing with a scanning laser tells us that there is significant spin coherence between the excited states.

In the integrated PL intensity, the AT doublet is clearly resolved in the signal of the $|1\rangle \rightarrow |4\rangle$ transition. When an increase in the signal is observed for the transition from level $|1\rangle$, a simultaneous decrease is observed in the signal related to the transition from level $|3\rangle$. This is due to the fact that the resonant excitation of dressed states by the probe laser excites electrons to level $|1\rangle$, thereby increasing the population of this level. As a result, there is a reduction in the possibility of electrons being excited to level $|3\rangle$, leading to a decrease in its population.

Discussion: AT splitting vs spectral hole burning

The observed splitting of the excitation doublet corresponds to the AT splitting of level $|2\rangle$. From the model fit in Fig. 4.11c, we extract the value of this splitting as the distance between two maxima. The extracted AT splitting is $\Omega_3 = 15$ µeV. This value is larger than the one predicted by the AT splitting power dependence depicted in Fig. 4.10b, where the linear dependence predicts $\Omega_3 = 10.96$ µeV. We can also extract the AT splitting Ω_3 from measurements done with stronger fixed laser. These points are presented in Fig. 4.10b as green squares. As it can be seen, for strong fixed laser powers (300 µeV and 530 µeV), the points calculated from two-laser probing are close to the one obtained by single-laser excitation. However, for lower fixed laser powers, the extracted Ω_3 is larger than the one expected from Fig. 4.10b.

The reason for this discrepancy can be better understood with the help of Fig. 4.12, which represents theoretical simulations in two limit cases. Here, excitation spectra, clearly showing AT splitting, are plotted as a function of the power of the fixed laser and the detuning of the scanning laser. This dependence is illustrated in Fig. 4.12a when inhomogeneous broadening is negligible (Gaussian FWHM= 0.1 µeV). However, when the inhomogeneous broadening observed in the measurements (Gaussian FWHM= 16 µeV) is introduced, it results in significantly different behavior, as depicted in Fig. 4.12b. This phenomenon represents spectral hole burning observed in inhomogeneously broadened systems, caused by the depletion of population in the common ground state driven by the strong laser. From Fig. 4.12b, it can be observed that the AT splitting is more affected for lower powers of the fixed laser, consistent with experimental observations. For higher laser powers, the AT doublet approaches the situation depicted in Fig. 4.12a, which explains the improved agreement of AT splittings presented in Fig. 4.10b.

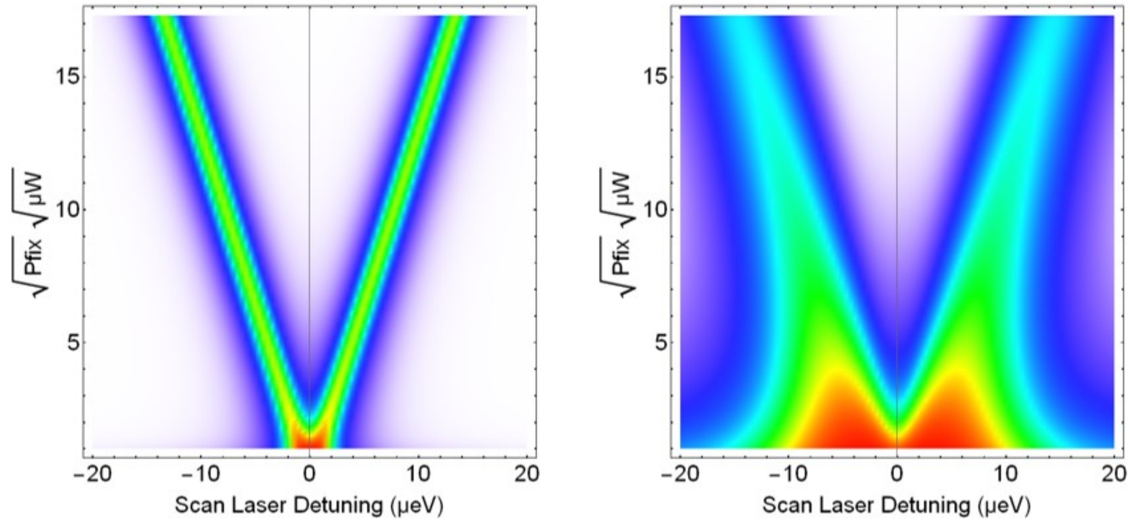

(a) (b)

Figure 4.12: Intensity maps generated by the model for AT splitting as a function of the power of the fixed laser and the detuning of the scanning laser when inhomogeneous broadening is (a) 0.1 μeV and (b) 16 μeV. The other important parameters are $\Gamma_{31} = 0$ μeV and power of scanning laser $P_1 = 1$ μW.

AT splitting dependence on fixed laser power and laser detuning

The same type of measurement as shown in Fig. 4.11 was conducted for different fixed laser powers. The integrated PL intensities from these measurements for the transition $|1\rangle \rightarrow |4\rangle$ are fitted with the model and presented in Fig. 4.13a. The parameters used in the model are the same as stated above, except for the non-resonant laser excitation rate γ_{nr}, which is adjusted for each measurement, and the Rabi frequencies Ω_1 and Ω_3, which are determined by the power of the fixed and scanning lasers. The curves generated by the model fit the experimental data well. As expected, it can be observed that with an increase in fixed laser power, the splitting of the AT doublet increases. Additionally, the intensity of the signal decreases with an increase in fixed laser power, which is also consistent with the model. Furthermore, despite the presence of spectral diffusion, the AT splitting is resolved even for fixed laser powers as low as $P_3 = 10$ μW.

A separate set of measurements was carried out for a constant fixed laser power of $P_3 = 150$ μW and different detunings δ_3 of the fixed laser with respect to the transition $|2\rangle \rightarrow |3\rangle$. These results are shown in Fig. 4.13b. When the fixed laser is resonant with the transition $|2\rangle \rightarrow |3\rangle$ ($\delta_3 = 0$), the peaks of the AT doublet have equal strength and are centered at the scanning laser detuning $\delta_1 = 0$. When the fixed laser is detuned, an energy shift is observed for both peaks, along with an increase in intensity for one of them. For larger detunings, only one peak should be observed, shifted by the AC Stark shift.

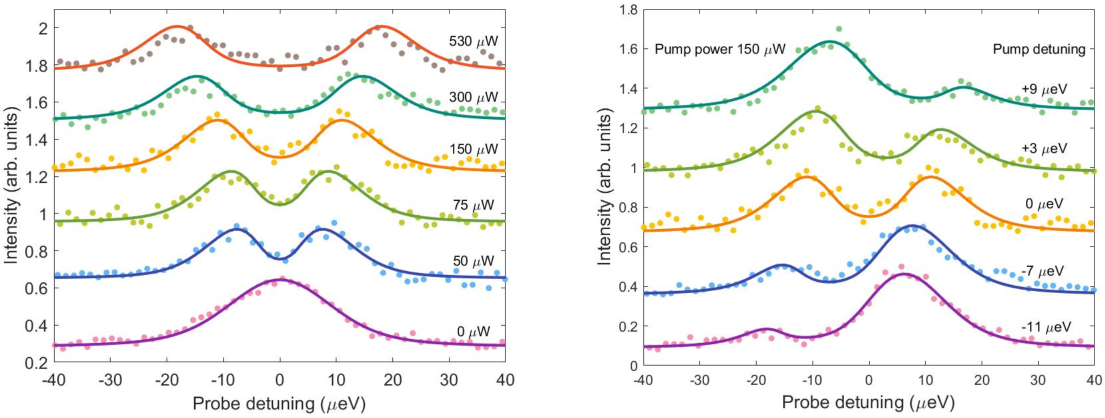

(a) (b)

Figure 4.13: Integrated PL intensities of transition $|1\rangle \rightarrow |4\rangle$ as a function of probe detuning for (a) different powers and (b) different detunings of fixed laser. The data are shifted vertically for clarity. Experimental points are fitted with model (solid lines).

4.3.2 Two-laser study of quantum interference effect

As discussed in section 4.3.1, probing the AT splitting with a second weak laser in the regime where the splitting is of the same order of magnitude as the inhomogeneous broadening results in a dip in a broad resonance line. The contrast of this dip depends on the coherence ρ_{31} generated by both lasers, representing a quantum interference between the optically induced coherences ρ_{21} and ρ_{23}. To investigate further this effect at lower excitation power, we performed a complementary study where the fixed laser exciting the transition $|2\rangle \rightarrow |3\rangle$ has weaker power, while the laser scanning the transition $|2\rangle \rightarrow |1\rangle$ is stronger. This situation is shown in Fig. 4.14. Similarly to the previous experiment, for laser powers of $P_3 = 1$ µW and $P_1 = 11$ µW, a series of PL spectra is recorded for different scanning laser detunings δ_L. As seen in Fig. 4.14b, when the scanning laser is resonant with transition $|2\rangle \rightarrow |1\rangle$, an increase in PL signal is observed for transition $|1\rangle \rightarrow |4\rangle$, while simultaneously, a well contrasted dip is observed for transition $|3\rangle \rightarrow |4\rangle$.

From this measurement, we can extract the integrated PL intensities for transitions $|1\rangle \rightarrow |4\rangle$ and $|3\rangle \rightarrow |4\rangle$. This experimental data are then fitted with the model, providing a good agreement as illustrated in Fig. 4.14c. The Rabi frequencies Ω_1 and Ω_3 are calculated from the power of the two lasers. The decay rates are the same as previously ($\gamma_3 = 0.8$ µeV and $\gamma_4 = 0.04$ µeV), while the non-resonant laser rate γ_{nr} is adjusted for this measurement. The branching ratios are also readjusted ($\eta_{14} = 0.55$ and $\eta_{34} = 0.45$). Inhomogeneous broadening is introduced as before (16 µeV), and for the best reproduction of the dip the pure dephasing Γ_{31} is set to zero.

It can also be noticed that the minimum of the signal for transition $|3\rangle \rightarrow |4\rangle$ and the maximum for transition $|1\rangle \rightarrow |4\rangle$ do not occur at the same scanning laser detuning. The minimum of intensity for $|3\rangle \rightarrow |4\rangle$ is redshifted by about 2 µeV, which is likely due to a small shift of the fixed laser energy with respect to the perfect resonance condition. Such a shift is indeed introduced in the model by defining the fixed laser detuning as $\delta_3 = -2$ µeV, to improve the fit to the experimental data. The

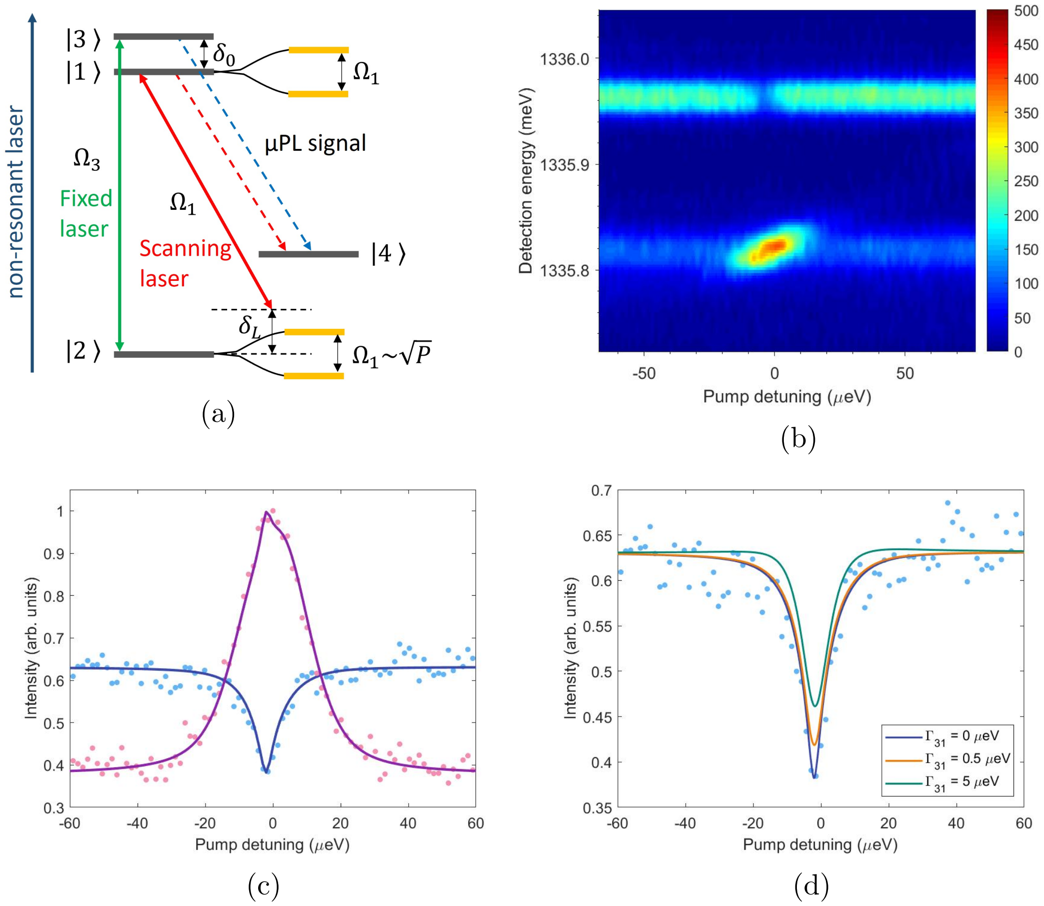

(a)

(b)

(c)

(d)

Figure 4.14: (a) Schematic representation of two-laser experiment, where weaker, fixed laser resonantly excites transition $|2\rangle \rightarrow |3\rangle$ and stronger laser is scanning through $|2\rangle \rightarrow |1\rangle$ transition. PL signal is measured for the transitions toward level $|4\rangle$. (b) Intensity map of PL emission as function of scanning laser detuning, where the fixed and scanning laser powers are $P_3 = 1$ µW and $P_1 = 11$ µW, respectively. (c) Integrated PL intensity for the same measurement of transition $|1\rangle \rightarrow |4\rangle$ (purple dots) and $|3\rangle \rightarrow |4\rangle$ (blue dots). Solid lines represent model fit when $\Gamma_{31} = 0$ µeV. (d) Model fit of the intensity of transition $|3\rangle \rightarrow |4\rangle$ for different, indicated values of $\Gamma_{31} = 0$.

dip is remarkably well resolved in the measurement, with a width of about 10 µeV. This is not surprising since it results from the double resonance conditions where the energy difference of both lasers verifies $\omega_1 - \omega_3 = \delta_0$, so that the dip formation does not suffer from the 16 µeV spectral diffusion of the QD. To some extent, this dip is similar to the dip observed in the well-known phenomenon of electromagnetically induced transparency (EIT) [112], indicating a kind of destructive interference between the laser field driving the $|2\rangle \rightarrow |3\rangle$ transition and the generated ρ_{31} coherence.

To again evidence the influence of the coherence ρ_{31}, theoretical fits of the dip are generated for a few different values of pure dephasing Γ_{31} (0 µeV, 0.5 µeV, 5 µeV), as illustrated in Fig. 4.14d. The best agreement is produced for very small Γ_{31}, while as Γ_{31} increases, the dip becomes less pronounced. However, the dip does not vanish even for large values of Γ_{31}. This is attributed to the strong laser, which continues to saturate the transition $|2\rangle \rightarrow |1\rangle$, causing some spectral hole burning.

The results of this section are perfectly consistent with the observations made for AT splitting probing, even though the best fitted values for Γ_{31} slightly differ. The coherence between levels $|1\rangle$ and $|3\rangle$ (small Γ_{31}) is definitely necessary for the contrast observed in both effects. In this respect, one can remark that in general both the regime of AT splitting and the EIT phenomenon can be observed when coherence effects are included [112], since both of these effects are described by the same set of OBE and therefore can exist simultaneously in V-type systems. Quantum interference effects, such as EIT, manifest at lower intensities of the pump laser. On the other hand, for stronger pump lasers, dressed states are clearly created resulting in the observation of AT splitting. However, there is a continuous transition between these two regimes [116].

4.4 Summary

In this chapter, our study is focused on coherence spectroscopy of Mn-doped InGaAs QD system, with the main objective of exploring the coherence ρ_{31} between the spin states of the trion.

In the first part, we concentrate on the single-laser excitation within the context of a V-type system of transitions. Here, a scanning laser is employed to resonantly excite one of the two transitions within the V-system, while the PL spectra are measured for transitions to the spectator state. Measurements were done for a range of resonant laser powers, providing us with a better understanding of this particular QD system. To achieve this, we employ a theoretical model based on the optical Bloch equations, specifically in the semi-classical approximation of the light-matter interaction. Several crucial parameters defining this QD are evaluated and discussed within the framework of this model. Some of these parameters, such as decay rates and oscillator strengths for different transitions, are carefully adjusted to match the experimental data. Moreover, the role of inhomogeneous broadening and pure dephasing in shaping the spectra is explored. The Autler-Townes splittings were resolved for high power excitation, enabling us to determine the Rabi frequencies, which represent the strength of the interband dipolar matrix element used in the model. Additionally, we investigate the dependence of Autler-Townes splitting on laser power. The comprehensive model developed in this chapter also allowed us to revisit a measurement recorded for a QD1 in a Schottky diode sample, previously described in section 2.3.2. The insights gained into the behavior of the critical parameters of this model facilitated the generation of a good fit for this QD as well. Furthermore, we were able to determine the spin relaxation time (T_1) from AFM to FM level and compare it for both QDs, as well as with the T_1 dependence reported in the literature. The spin relaxation time in our QDs is of the order of ns, depending on the splitting Δ for a particular QD. This timescale is comparable to the spin relaxation time reported for a single Mn atom in II-VI QDs in Ref. [89]. This single-laser experiment serves as the foundation for understanding the subsequent two-laser experiments, presented in the second part of the chapter. The use of two lasers is instrumental in generating coherence between the excited spin states, which is essential for probing of the Autler-Townes effect and EIT-like effect. In the first two-laser experiment, a strong fixed laser is employed to excite one transition, while a weaker laser scans the second transition within the V-system. This arrangement allows us to observe the AT effect, characterized by the splitting of dressed states. The experimental results are analyzed using the theoretical model, shedding light on the significance of both coherent and incoherent effects, particularly spectral hole burning.

In a subsequent experiment, the powers of the fixed and scanning lasers are reversed, resulting in different excitation conditions. This configuration results in the observation of EIT-like effect, stemming from the coherence between energy levels. We investigate the influence of coherence by varying the pure dephasing parameter, revealing that small values of dephasing are crucial for observing both the AT effect and quantum interference.

These experiments collectively contribute to a comprehensive understanding of Mn-doped InGaAs QD behavior under resonant excitation, shedding light on the intricate interplay of coherence, inhomogeneous broadening, and laser power in this system.

Conclusion

The initial objective of this thesis was to study Mn-doped InGaAs QDs under resonant excitation to achieve spin manipulation and study the spin coherence properties of the neutral acceptor A^0 and FM complex hole-A^0. The initial idea was to perform coherent population trapping of A^0 spin states at a specific magnetic field when the transitions form a W-like system, as in Ref. [13]. This would allow us to determine the spin coherence time T_2^*.

In the first part of this work, a dark-field confocal microscope setup was constructed to enable the resonant excitation of Mn-doped QDs. The significance of optical components and origin of observed clover-leaf patter were examined through both experimental results and a theoretical models. The resulting setup demonstrated high efficiency in filtering out reflected laser light, achieving an optical density exceeding 7, which is close to state-of-the-art laser extinction levels [29]. However, despite this remarkable laser extinction performance, measuring resonance fluorescence for Mn-doped QDs without a solid-immersion lens or cavity structure posed challenges. Despite estimating that the PL signal was approximately 40 times higher than the residual laser shot noise, it was not possible to resolve it. This could be due to the presence of QD blinking or OD instabilities. Nonetheless, the Λ-like system of transitions in these QDs proved valuable for conducting resonance Raman scattering measurements. This involved resonantly exciting one of the transitions of the Λ-like system and measuring the PL signal for the other transition, located approximately 1 meV below the excitation energy. The setup demonstrated stability over time and across a range of wavelengths (typically a few hundred picometers), sufficient for conducting such measurements. This setup was initially tested on a QD in a Schottky diode sample, specifically for the case of a positively charged QD. A simple theoretical model based on rate equations was developed to fit the experimental data and provided an estimation of the spin relaxation time from the AFM level to the FM level. The observed resonance linewidth in these measurements was notably broader than the natural linewidth of InAs QD, suggesting a possible presence of spectral diffusion.

To examine closer the origin of this broad resonance linewidth, we conducted a similar experiment in a sample without a Schottky diode to eliminate potential effects of a large dark current on this linewidth. This particular sample had undergone hydrogenation, resulting in the bonding of hydrogen with neighboring As atoms of the Mn dopant. This process prevented the formation of a neutral acceptor state, leading to compensated Mn dopants. These QDs exhibited a distinctive optical signature, characterized by a complex set of lines showing an unusual evolution in a longitudinal magnetic field. To better understand these results, we developed a theoretical model for H-passivated Mn dopants. This model demonstrated a relatively good qualitative agreement with the experimental results, successfully reproducing the most significant anticrossings. However, achieving this qualitative agreement required considering a ferromagnetic character for the h-Mn exchange interaction. This finding contrasts with previously reported antiferromagnetic p-d exchange in II-VI and III-V QDs [1, 6], and could warrant further examination in future studies. Additionally, resonant optical excitation measurements were conducted on this QD, further validating the theoretical model and its predictions of energy levels. Subsequently, the sample underwent an annealing process, leading to the restoration of the standard neutral acceptor state of the Mn dopant.

In the subsequent section of the thesis, this sample was used for coherence spectroscopy of Mn-doped InGaAs QD system. Initially, a single laser was employed to resonantly excite one of the transitions of the V-like system, while simultaneously measuring the PL for transitions toward a spectator state. The measurements for different powers of resonant lasers were performed. A theoretical model based on the optical Bloch equations was formulated to interpret these experimental results. A good agreement was achieved between the experimental data and the theoretical fits, leading to discussions on the crucial parameters of the model. It was deemed essential to introduce inhomogeneous broadening to replicate the experimental results, confirming the presence of significant spectral diffusion in these samples. At high laser powers, Autler-Townes splitting was resolved, and its dependence on laser power was examined. Utilizing this model, we were able to determine the spin relaxation time from the AFM to FM level, which was found to be on the order of nanoseconds. Notably, this falls within the same order of magnitude as the spin relaxation time observed for a single Mn atom in II-VI QD, as reported in Ref. [89].

Following this, a two-laser experiment was conducted for the same QD. In the first part of this experiment, a strong laser was fixed, resonantly exciting one of the transitions of the V-type system, while a weaker second laser scanned the second transition. In this configuration, the Autler-Townes effect was observed, and the corresponding splitting was resolved. The theoretical model was employed to discuss coherent and incoherent effects, focusing on the presence of spectral hole burning. In the second part of the two-laser experiment, the powers of the lasers were reversed, leading to the observation of an EIT-like effect. For observation of both AT and EIT-like effect it was crucial to use two lasers to generate coherence between the excited spin states. The influence of coherence was investigated theoretically by varying the pure dephasing parameter. It was demonstrated that small values of dephasing are essential for the observation of both Autler-Townes and EIT-like effects. These experiments contribute to a deeper understanding of coherence and inhomogeneous broadening in this system.

In the future, the next step could involve producing samples with the QD layer embedded in a planar cavity and/or using a solid-immersion lens (SIL). Here, there is however an inherent difficulty related to the rarity of the effectively Mn-doped QDs and to their multi-line nature spread over ~1 meV. Only relatively low Q-factor (of the order of 100, namely with typical 1 meV resonance width) could be employed to detect and access to Mn-doped QD, thus with a probability typically reduced by 10 (as usual spectral range on our CCD is 10 meV). Similarly, finding a Mn-doped QD in the limited field of view of a SIL might also be very challenging. Nevertheless, if successful, such enhancement could significantly increase the collected PL signal and enable the direct measurement of resonance fluorescence, particularly in a lower regime of excitation than explored in this thesis. For the neutral exciton state in these QDs, the presence of a W-like system could then be exploited. At a specific magnetic field, when these transitions form a W-like system, it would be feasible to conduct coherent population trapping experiments in order to measure through two-laser experiments, the coherence of magnetic spin in the QD ground state. In this regard, the relatively short lifetime of the AFM level estimated in this thesis might be very specific to the case of a positively charged QD and therefore does not compromise such investigations. This W-like system, as outlined in Ref. [13], holds potential for spin manipulation by exciting inner transitions, while driving non-destructive (cycling) outer transitions enable spin read-out. Such a configuration would be relevant for application to the generation of photonic cluster states, following the protocol proposed in Ref. [76]. The actual development of this subject remains however drastically conditioned to the possibility of reducing the large inhomogeneous broadening, observed so far in three different samples. This is most likely an issue of material science requiring a significant investment in growth, fabrication and characterization, with the risk that this property could be inherent to Mn doping.

Appendix A

Quantum regression model

In this section, we will focus on simulating PL spectra obtained through single-laser probing. As illustrated in Fig. 4.3b, a single laser scans through the transitions $|2\rangle \rightarrow |1\rangle$ and $|2\rangle \rightarrow |3\rangle$, while the PL signal is recorded for transitions $|1\rangle \rightarrow |4\rangle$ and $|3\rangle \rightarrow |4\rangle$. Despite these transitions being separated by a splitting of $\delta_0 = 144$ µeV, it is necessary to consider them together in the autocorrelation function to reproduce the Raman line.

The Wiener-Khintchine theorem states that the spectrum of a stationary process can be determined by the two-time correlation function of the radiated field [109, 111]:

$$S(\omega) = \frac{1}{2\pi} \lim_{x\to\infty} \frac{1}{T} \int_0^T dt \int_0^T dt' \langle \boldsymbol{E}^-(t) \boldsymbol{E}^+(t') \rangle e^{(-i\omega(t-t'))} \tag{A.1}$$

where $\boldsymbol{E}^+(t)$ represents the positive frequency component of the electric field. Assuming the field, in a steady state, is statistically stationary, the correlation $\langle \boldsymbol{E}^-(t)\boldsymbol{E}^+(t')\rangle$ depends solely on the time difference, denoted as $\tau = t - t'$. This allows us to rewrite the previous equation as follows:

$$\begin{aligned} S(\omega) &= \frac{1}{2\pi} \lim_{x\to\infty} \frac{1}{T} \int_0^T dt \left[\int_0^t dt' + \int_t^T dt' \right] \langle \boldsymbol{E}^-(t) \boldsymbol{E}^+(t') \rangle e^{(-i\omega(t-t'))} \\ &= \frac{1}{2\pi} \lim_{x\to\infty} \frac{1}{T} \int_0^T dt \left[\int_0^t d\tau \langle \boldsymbol{E}^-(\tau) \boldsymbol{E}^+(0) \rangle e^{-i\omega\tau} + \int_0^{T-t} d\tau \langle \boldsymbol{E}^-(0) \boldsymbol{E}^+(\tau) \rangle e^{i\omega\tau} \right] \end{aligned} \tag{A.2}$$

When the field operators are correlated over a short period of time, we can extend the upper limit of the τ integrations to infinity with negligible changes. Additionally, considering that $\langle \boldsymbol{E}^-(\tau)\boldsymbol{E}^+(0)\rangle = \langle \boldsymbol{E}^-(0)\boldsymbol{E}^+(\tau)\rangle^*$, Eq. A.2 can be expressed as:

$$S(\omega) = \frac{1}{\pi} Re \int_0^\infty d\tau \langle \boldsymbol{E}^-(0) \boldsymbol{E}^+(\tau) \rangle e^{i\omega\tau} \tag{A.3}$$

In this context, the autocorrelation function can be described as $\langle (\boldsymbol{\epsilon_V^*} \cdot \boldsymbol{E}^-(0))(\boldsymbol{\epsilon_V} \cdot \boldsymbol{E}^+(\tau))\rangle$, where $\boldsymbol{\epsilon_V}$ is the polarization vector (vertical) used in the detection arm. The electric field can be defined as a sum of two fields, namely, $\boldsymbol{E}^+ = \boldsymbol{E}^+_{41} + \boldsymbol{E}^+_{43}$.

To proceed, we must define the dipoles for the four transitions of the system:

$$\boldsymbol{d_{ij}} = -e\langle i|\boldsymbol{\hat{r}}|j\rangle \qquad\qquad i \in \{2,4\},\ j \in \{1,3\} \tag{A.4}$$

The Rabi frequencies Ω_j and field operators $\boldsymbol{E}^{+}_{4j}$ can be written as:

$$\hbar\Omega_j = -\boldsymbol{d_{2j}} \cdot \boldsymbol{E_0} \qquad j \in \{1,3\} \tag{A.5}$$

$$\boldsymbol{E}^{+}_{4j} \propto \sqrt{\gamma_j}\frac{\boldsymbol{d_{4j}}}{||\boldsymbol{d_{4j}}||}\hat{\sigma}_{4j} \qquad j \in \{1,3\} \tag{A.6}$$

The next step is to determine the basis for calculating the dipolar matrix elements $\boldsymbol{d}_{ij}$. The four states of the system are all double degenerate. For example, the state $|2\rangle$ corresponds to the ferromagnetic configuration and can be defined as $|\pm 3/2, \pm 1\rangle$. However, in these calculations we can consider only one spin sub-space since the product of creation and annihilation operators of different spin sub-spaces is zero and electron and hole are assumed to be pure spin state in zero field. Thus, the degeneracy results only in a factor of 2 in the calculated PL intensity. We can choose to work in the spin-up space, where the basis can be defined as follows:

$$|1\rangle = |+1/2\rangle \otimes \left(|+1\rangle + |-1\rangle\right)/\sqrt{2} \tag{A.7}$$

$$|3\rangle = |+1/2\rangle \otimes \left(|+1\rangle - |-1\rangle\right)/\sqrt{2} \tag{A.8}$$

$$|2\rangle = |+3/2, +1\rangle \tag{A.9}$$

$$|4\rangle = |+3/2, -1\rangle \tag{A.10}$$

Here, we assume that the electron-A^0 interaction can be neglected, and there is no mixing with other A^0 states. The dipolar matrix elements are then represented as:

$$\boldsymbol{d_{21}} = \boldsymbol{d_0}/\sqrt{2} \tag{A.11}$$

$$\boldsymbol{d_{23}} = \boldsymbol{d_0}/\sqrt{2} \tag{A.12}$$

$$\boldsymbol{d_{41}} = \boldsymbol{d_0}/\sqrt{2} \tag{A.13}$$

$$\boldsymbol{d_{43}} = -\boldsymbol{d_0}/\sqrt{2} \tag{A.14}$$

where $\boldsymbol{d_0} = -e\langle +3/2|\hat{\boldsymbol{r}}| + 1/2\rangle$. Consequently, the Rabi frequencies defined by Eq. A.5 have the same sign, while the field operators in Eq. A.6 are of the opposite sign. Taking into account the definitions of these operators, Eq. A.3, which defines the PL intensity, can be written as:

$$I_{PL}(\omega) \propto \gamma Re\int_0^{\infty}[\langle\hat{\sigma}_{14}(0)\hat{\sigma}_{41}(\tau)\rangle + \langle\hat{\sigma}_{34}(0)\hat{\sigma}_{43}(\tau)\rangle - \langle\hat{\sigma}_{14}(0)\hat{\sigma}_{43}(\tau)\rangle - \langle\hat{\sigma}_{34}(0)\hat{\sigma}_{41}(\tau)\rangle]e^{i\omega\tau}d\tau \tag{A.15}$$

To calculate this intensity, we must first define the atomic operators σ_{ij}. As previously described in Chapter 4, the system is described with a Lindblad master equation:

$$\frac{\partial\rho}{\partial t} = -\frac{i}{\hbar}[\boldsymbol{H}_0, \rho] + i\hbar\sum_i\left(L_i\rho L_i^{\dagger} - \frac{1}{2}\{L_i^{\dagger}L_i, \rho\}\right) \tag{A.16}$$

The second term in this equation corresponds to Linblad superoperators, and $\boldsymbol{H}_0$ is the Hamiltonian in the rotating frame, as given by:

$$\boldsymbol{H}_0 = \begin{bmatrix} \delta_1 & \Omega_1 & 0 & 0 \\ \Omega_1 & 0 & \Omega_3 e^{i\phi} & 0 \\ 0 & \Omega_3 e^{-i\phi} & \delta_1 + \delta_0 & 0 \\ 0 & 0 & 0 & \Delta \end{bmatrix} \tag{A.17}$$

where δ_1 represents the laser detuning from transition $|2\rangle \rightarrow |1\rangle$, and δ_0 (Δ) represents the splitting between levels $|1\rangle$ and $|3\rangle$ ($|2\rangle$ and $|4\rangle$). Note that in Eq. A.17, we introduced an additional phase factor $e^{i\phi}$ to reveal the important role of the respective signs of the dipoles in Eq. A.13 and Eq. A.14. From the master equation, taking into account off-diagonal elements, we can write:

$$\frac{d}{dt} \begin{bmatrix} \rho_{14} \\ \rho_{24} \\ \rho_{34} \end{bmatrix} = \boldsymbol{M} \begin{bmatrix} \rho_{14} \\ \rho_{24} \\ \rho_{34} \end{bmatrix} \tag{A.18}$$

where the matrix $\boldsymbol{M}$ is defined as:

$$\boldsymbol{M} = \begin{bmatrix} -\frac{\gamma_1}{2} - \frac{\gamma_4}{2} - \frac{\Gamma_{31}}{2} - \frac{\gamma_{nr}}{2} + i(\Delta - \delta_1) & -i\Omega_1 & 0 \\ -i\Omega_1 & -\frac{\gamma_4}{2} - \gamma_{nr} + i\Delta & -i\Omega_3 e^{i\phi} \\ 0 & -i\Omega_3 e^{-i\phi} & -\frac{\gamma_3}{2} - \frac{\gamma_4}{2} - \frac{\Gamma_{31}}{2} - \frac{\gamma_{nr}}{2} + i(\Delta - \delta_1 - \delta_0) \end{bmatrix} \tag{A.19}$$

In this context, the splitting Δ can be considered zero, as it does not enter into the subsequent calculation steps. Thanks to the relationship between the Schrödinger and Heisenberg pictures [109], the connection between density matrix elements and the expected value of atomic operators can be expressed as $\rho_{ij} = \langle \sigma_{ji} \rangle$. Plugging this relation into Eq. A.18, we can write:

$$\frac{d}{dt} \begin{bmatrix} \langle \sigma_{41} \rangle \\ \langle \sigma_{42} \rangle \\ \langle \sigma_{43} \rangle \end{bmatrix} = \boldsymbol{M} \begin{bmatrix} \langle \sigma_{41} \rangle \\ \langle \sigma_{42} \rangle \\ \langle \sigma_{43} \rangle \end{bmatrix} \tag{A.20}$$

To calculate the expectation values of two-time correlation functions of atomic operators, which appear in the integral in Eq. A.15, we can use the quantum regression theorem:

$$\frac{d}{d\tau} \langle \hat{A}(0) \hat{A}_j(\tau) \rangle = \sum_k L_{j,k} \langle \hat{A}(0) \hat{A}_k(\tau) \rangle \tag{A.21}$$

By employing this theorem and Eq. A.20, we can then write:

$$\frac{d}{dt} \begin{bmatrix} \langle \sigma 14(0) \sigma 41(\tau) \rangle \\ \langle \sigma 14(0) \sigma 42(\tau) \rangle \\ \langle \sigma 14(0) \sigma 43(\tau) \rangle \end{bmatrix} = \boldsymbol{M} \begin{bmatrix} \langle \sigma 14(0) \sigma 41(\tau) \rangle \\ \langle \sigma 14(0) \sigma 42(\tau) \rangle \\ \langle \sigma 14(0) \sigma 43(\tau) \rangle \end{bmatrix} \tag{A.22}$$

which means that we need to solve a differential equation of the form:

$$\frac{d}{dt} \boldsymbol{V} = \boldsymbol{M} \boldsymbol{V} \tag{A.23}$$

To solve this equation, we can first determine the Jordan normal form of the matrix $\boldsymbol{M}$:

$$\boldsymbol{D} = \boldsymbol{P}^{-1}\boldsymbol{M}\boldsymbol{P} \tag{A.24}$$

where $\boldsymbol{D} = diag(\lambda_1, \lambda_2, \lambda_3)$ with λ_i representing the eigenvalues and $\boldsymbol{P}$ the eigenvectors of the matrix $\boldsymbol{M}$. Eq. A.23 can now be rewritten as:

$$\frac{d}{dt}\boldsymbol{V} = \boldsymbol{P}[\boldsymbol{P}^{-1}\boldsymbol{M}\boldsymbol{P}]\boldsymbol{P}^{-1}\boldsymbol{V} \tag{A.25}$$

The solution of this differential equation is:

$$\boldsymbol{V}(\tau) = \boldsymbol{P}e^{\boldsymbol{D}\tau}\boldsymbol{P}^{-1}\boldsymbol{V}(0) \tag{A.26}$$

Therefore, the solution of Eq. A.22 can be expressed as:

$$\begin{bmatrix} \langle\sigma 14(0)\sigma 41(\tau)\rangle \\ \langle\sigma 14(0)\sigma 42(\tau)\rangle \\ \langle\sigma 14(0)\sigma 43(\tau)\rangle \end{bmatrix} = \boldsymbol{P}\begin{bmatrix} e^{\lambda_1\tau} & 0 & 0 \\ 0 & e^{\lambda_2\tau} & 0 \\ 0 & 0 & e^{\lambda_3\tau} \end{bmatrix}\boldsymbol{P}^{-1}\begin{bmatrix} \langle\sigma 11\rangle \\ \langle\sigma 12\rangle \\ \langle\sigma 13\rangle \end{bmatrix} \tag{A.27}$$

This can be written in a more concise form as:

$$\langle\sigma 14(0)\sigma 4j(\tau)\rangle = \sum_{j=1,2,3} a_j e^{\lambda_j\tau} \tag{A.28}$$

where a_j represents the coefficients calculated from the right-hand side of Eq. A.22.

Similar calculations for $\langle\sigma 34(0)\sigma 4j(\tau)\rangle$ lead to:

$$\langle\sigma 34(0)\sigma 4j(\tau)\rangle = \sum_{j=1,2,3} b_j e^{\lambda_j\tau} \tag{A.29}$$

The four terms in the integral in Eq. A.15 can be expressed as the sum of Eq. A.28 and Eq. A.29: $\sum\limits_{j=1,2,3} c_j e^{\lambda_j\tau}$, where $c_j = a_j + b_j$. Finally, by taking $\lambda_j = -(y_j + ix_j)$, the PL intensity can be calculated as:

$$\begin{aligned} I_{PL}(\omega) &\propto Re\int_0^\infty \left(\sum_{j=1,2,3} c_j e^{-(y_j+ix_j)\tau}\right) e^{i\omega\tau}d\tau \\ &\propto Re\left\{\sum_{j=1,2,3} c_j \frac{y_j + i(\omega - x_j)}{y_j^2 - (\omega - x_j)^2}\right\} \end{aligned} \tag{A.30}$$

In addition to this calculated PL intensity I_{PL}, to simulate the measurements in Fig. 4.4, we need to include inhomogeneous broadening and the finite spectral resolution of our measurements. Similar to the model in section 4.2.2, inhomogeneous broadening is incorporated by performing a discrete convolution of I_{PL} with a Gaussian of FWHM= 16 µeV. Following that, to replicate the spectral resolution of the measurement, we perform another discrete convolution of the PL spectrum with a Gaussian of FWHM= 18 µeV. The final results of these calculations are displayed in Fig. 4.7.

To reproduce the Stokes Raman line between the two resonances, it is essential to include a phase shift $\phi = \pi$ in Eq. A.7 and A.8. Fig. A.1b shows the simulation for a zero shift $\phi = 0$, in which case the Raman line is not present around the middle of the spectra, contrary to the experimental results.

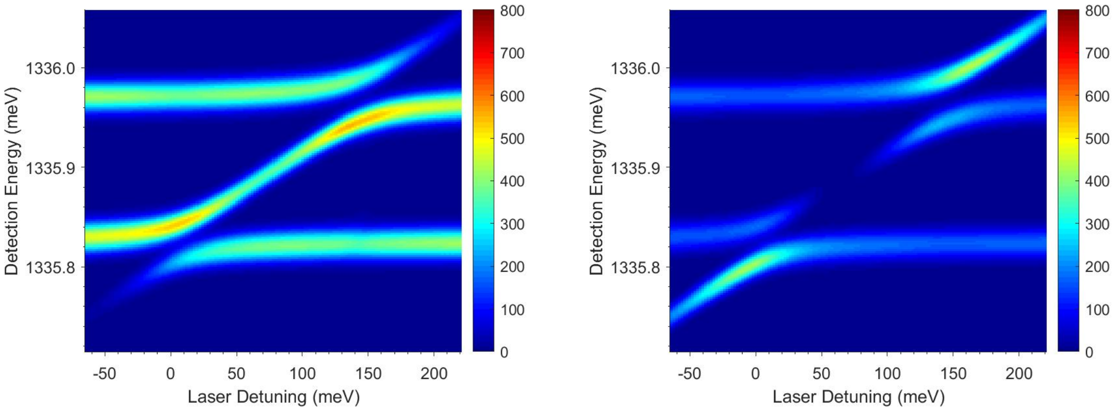

(a) (b)

Figure A.1: Intensity maps of simulated µPL spectra as a function of resonant laser detuning δ_L and detection energy for the laser power of 810 µW, when phase shift is: (a) $\phi = \pi$ in agreement with Eqs. A.13 A.14, and (b) $\phi = 0$ if orthogonality of the eigenstates is not respected.

Bibliography

[1] L. Besombes, Y. Léger, L. Maingault, D. Ferrand, H. Mariette, and J. Cibert. Probing the spin state of a single magnetic ion in an individual quantum dot. *Physical review letters*, 93(20):207403, 2004.

[2] Y. Léger, L. Besombes, L. Maingault, D. Ferrand, and H. Mariette. Geometrical effects on the optical properties of quantum dots doped with a single magnetic atom. *Physical review letters*, 95(4):047403, 2005.

[3] Y. Léger, L. Besombes, J. Fernández-Rossier, L. Maingault, and H. Mariette. Electrical control of a single Mn atom in a quantum dot. *Physical review letters*, 97(10):107401, 2006.

[4] Y. Léger, L. Besombes, L. Maingault, and H. Mariette. Valence-band mixing in neutral, charged, and Mn-doped self-assembled quantum dots. *Physical Review B*, 76(4):045331, 2007.

[5] A. Kudelski, A. Lemaitre, A. Miard, P. Voisin, T. C. M. Graham, R. J. Warburton, and O. Krebs. Optically probing the fine structure of a single Mn atom in an InAs quantum dot. *Physical review letters*, 99(24):247209, 2007.

[6] O. Krebs, E. Benjamin, and A. Lemaître. Magnetic anisotropy of singly Mn-doped InAs/GaAs quantum dots. *Physical Review B*, 80(16):165315, 2009.

[7] A. H. Trojnar, M. Korkusiński, E. S. Kadantsev, P. Hawrylak, M. Goryca, T. Kazimierczuk, P. Kossacki, P. Wojnar, and M. Potemski. Quantum interference in exciton-Mn spin interactions in a CdTe semiconductor quantum dot. *Physical Review Letters*, 107(20):207403, 2011.

[8] A. H. Trojnar, M. Korkusinski, U. C. Mendes, M. Goryca, M. Koperski, T. Smolenski, P. Kossacki, P. Wojnar, and P. Hawrylak. Fine structure of a biexciton in a single quantum dot with a magnetic impurity. *Physical Review B*, 87(20):205311, 2013.

[9] U. C. Mendes, M. Korkusinski, A. H. Trojnar, and P. Hawrylak. Optical properties of charged quantum dots doped with a single magnetic impurity. *Physical Review B*, 88(11):115306, 2013.

[10] C. Le Gall, L. Besombes, H. Boukari, R. Kolodka, J. Cibert, and H. Mariette. Optical spin orientation of a single manganese atom in a semiconductor quantum dot using quasiresonant photoexcitation. *Physical Review Letters*, 102(12):127402, 2009.

[11] C. Le Gall, R. S. Kolodka, C. L. Cao, H. Boukari, H. Mariette, J. Fernández-Rossier, and L. Besombes. Optical initialization, readout, and dynamics of a Mn spin in a quantum dot. *Physical Review B*, 81(24):245315, 2010.

[12] C. Le Gall, A. Brunetti, H. Boukari, and L. Besombes. Optical stark effect and dressed exciton states in a Mn-doped CdTe quantum dot. *Physical Review Letters*, 107(5):057401, 2011.

[13] E. Baudin, E. Benjamin, A. Lemaître, and O. Krebs. Optical pumping and a nondestructive readout of a single magnetic impurity spin in an InAs/GaAs quantum dot. *Physical review letters*, 107(19):197402, 2011.

[14] M. Goryca, T. Kazimierczuk, M. Nawrocki, A. Golnik, J. A. Gaj, P. Kossacki, P. Wojnar, and G. Karczewski. Optical manipulation of a single Mn spin in a CdTe-based quantum dot. *Physical review letters*, 103(8):087401, 2009.

[15] D. E. Reiter, T. Kuhn, and V. M. Axt. All-optical spin manipulation of a single manganese atom in a quantum dot. *Physical review letters*, 102(17):177403, 2009.

[16] D. E. Reiter, T. Kuhn, and V. M. Axt. Coherent control of a single Mn spin in a quantum dot via optical manipulation of the light hole exciton. *Physical Review B*, 83(15):155322, 2011.

[17] L. Besombes, C. L. Cao, S. Jamet, H. Boukari, and J. Fernandez-Rossier. Optical control of the spin state of two Mn atoms in a quantum dot. *Physical Review B*, 86(16):165306, 2012.

[18] O. Krebs and A. Lemaître. Optically induced coupling of two magnetic dopant spins by a photoexcited hole in a Mn-doped InAs/GaAs quantum dot. *Physical Review Letters*, 111(18):187401, 2013.

[19] J. Kobak, T. Smoleński, M. Goryca, M. Papaj, K. Gietka, A. Bogucki, M. Koperski, J. G. Rousset, J. Suffczyński, E. Janik, et al. Designing quantum dots for solotronics. *Nature communications*, 5(1):3191, 2014.

[20] N. Somaschi, V. Giesz, L. De Santis, J. C. Loredo, M. P. Almeida, G. Hornecker, S. L. Portalupi, T. Grange, C. Anton, J. Demory, et al. Near-optimal single-photon sources in the solid state. *Nature Photonics*, 10(5):340–345, 2016.

[21] L. Zhai, M. C. Löbl, G. N. Nguyen, J. Ritzmann, A. Javadi, C. Spinnler, A. D. Wieck, A. Ludwig, and R. J. Warburton. Low-noise GaAs quantum dots for quantum photonics. *Nature communications*, 11(1):4745, 2020.

[22] N. Tomm, A. Javadi, N. O. Antoniadis, D. Najer, M. C. Löbl, A. R. Korsch, R. Schott, S. R. Valentin, A. D. Wieck, A. Ludwig, et al. A bright and fast source of coherent single photons. *Nature Nanotechnology*, 16(4):399–403, 2021.

[23] N. H. Lindner and T. Rudolph. Proposal for pulsed on-demand sources of photonic cluster state strings. *Physical review letters*, 103(11):113602, 2009.

[24] N. Coste, D. A. Fioretto, N. Belabas, S. C. Wein, P. Hilaire, R. Frantzeskakis, M. Gundin, B. Goes, N. Somaschi, M. Morassi, et al. High-rate entanglement between a semiconductor spin and indistinguishable photons. *Nature Photonics*, pages 1–6, 2023.

[25] D. Cogan, Z. E. Su, O. Kenneth, and D. Gershoni. Deterministic generation of indistinguishable photons in a cluster state. *Nature Photonics*, 17(4):324–329, 2023.

[26] I. Schwartz, D. Cogan, E. R. Schmidgall, Y. Don, L. Gantz, O. Kenneth, N. H. Lindner, and D. Gershoni. Deterministic generation of a cluster state of entangled photons. *Science*, 354(6311):434–437, 2016.

[27] K. Tiurev, P. L. Mirambell, M. B. Lauritzen, M. H. Appel, A. Tiranov, P. Lodahl, and A. S. Sørensen. Fidelity of time-bin-entangled multiphoton states from a quantum emitter. *Physical Review A*, 104(5):052604, 2021.

[28] A. Vezvaee, P. Hilaire, M. F. Doty, and S. E. Economou. Deterministic generation of entangled photonic cluster states from quantum dot molecules. *Physical Review Applied*, 18(6):L061003, 2022.

[29] A. V. Kuhlmann, J. Houel, D. Brunner, A. Ludwig, D. Reuter, A. D. Wieck, and R. J. Warburton. A dark-field microscope for background-free detection of resonance fluorescence from single semiconductor quantum dots operating in a set-and-forget mode. *Review of scientific instruments*, 84(7):073905, 2013.

[30] I. N. Stranski and L. Krastanow. Zur theorie der orientierten ausscheidung von ionenkristallen aufeinander. *Monatshefte für Chemie und verwandte Teile anderer Wissenschaften*, 71(1):351–364, 1937.

[31] L. Goldstein, F. Glas, J. Y. Marzin, M. N. Charasse, and G. Le Roux. Growth by molecular beam epitaxy and characterization of an InAs/GaAs strained-layer superlattices. *Appl. Phys. Lett.*, 47(10):1099–1101, 1985.

[32] A. Lemaître, G. Patriarche, and F. Glas. Composition profiling of InAs/ GaAs quantum dots. *Appl. Phys. Lett.*, 85(17):3717–3719, 2004.

[33] P. Senellart, V. Giesz, and L. Lanco. Ultrabright single-photon sources. *Photoniques*, pages 23–26, 2017.

[34] R. C. Ashoori. Electrons in artificial atoms. *Nature*, 379(6564):413–419, 1996.

[35] F. B. Pedersen and Y. C. Chang. Energy levels of one and two holes in parabolic quantum dots. *Phys. Rev. B*, 53(3):1507, 1996.

[36] L. W. Wang, J. Kim, and A. Zunger. Electronic structures of [110]-faceted self-assembled pyramidal InAs/ GaAs quantum dots. *Phys. Rev. B*, 59(8):5678, 1999.

[37] A.J. Williamson, L. W. Wang, and A. Zunger. Theoretical interpretation of the experimental electronic structure of lens-shaped self-assembled InAs/ GaAs quantum dots. *Phys. Rev. B*, 62(19):12963, 2000.

[38] O. Stier, M. Grundmann, and D. Bimberg. Electronic and optical properties of strained quantum dots modeled by 8-band k.p theory. *Phys. Rev. B*, 59(8):5688, 1999.

[39] K. F. Brennan. *The physics of semiconductors: with applications to optoelectronic devices.* Cambridge university press, 1999.

[40] J. Y. Marzin and G Bastard. Calculation of the energy levels in InAs/ GaAs quantum dots. *Solid state communications*, 92(5):437–442, 1994.

[41] R. Heitz, M. Veit, N. N. Ledentsov, A. Hoffmann, D. Bimberg, V. M. Ustinov, P. S. Kopâ€™ev, and Zh. I. Alferov. Energy relaxation by multiphonon processes in InAs/GaAs quantum dots. *Phys. Rev. B*, 56(16):10435, 1997.

[42] Y. Toda, O. Moriwaki, M. Nishioka, and Y. Arakawa. Efficient carrier relaxation mechanism in InGaAs/GaAs self-assembled quantum dots based on the existence of continuum states. *Phys. Rev. Lett.*, 82(20):4114, 1999.

[43] G. Medeiros-Ribeiro, F. G. Pikus, P. M. Petroff, and A. L. Efros. Single-electron charging and Coulomb interaction in InAs self-assembled quantum dot arrays. *Physical Review B*, 55(3):1568, 1997.

[44] U. Banin, Y. W. Cao, D. Katz, and O. Millo. Identification of atomic-like electronic states in indium arsenide nanocrystal quantum dots. *Nature*, 400(6744):542–544, 1999.

[45] D. Bimberg, M. Grundmann, and N. N. Ledentsov. *Quantum dot heterostructures.* John Wiley & Sons, 1999.

[46] J. Suffczyński, T. Kazimierczuk, M. Goryca, B. Piechal, A. Trajnerowicz, K. Kowalik, P. Kossacki, A. Golnik, K. P. Korona, M. Nawrocki, et al. Excitation mechanisms of individual CdTe/ZnTe quantum dots studied by photon correlation spectroscopy. *Physical Review B*, 74(8):085319, 2006.

[47] C. Santori, M. Pelton, G. Solomon, Y. Dale, and Y. Yamamoto. Triggered single photons from a quantum dot. *Physical Review Letters*, 86(8):1502, 2001.

[48] E. Moreau, I. Robert, J. M. Gérard, I. Abram, L. Manin, and V. Thierry-Mieg. Single-mode solid-state single photon source based on isolated quantum dots in pillar microcavities. *Applied Physics Letters*, 79(18):2865–2867, 2001.

[49] D. N. Krizhanovskii, A. Ebbens, A. I. Tartakovskii, F. Pulizzi, T. Wright, M. S. Skolnick, and M. Hopkinson. Individual neutral and charged $\mathrm{In}_x\mathrm{Ga}_{1-x}\mathrm{As}$-GaAs quantum dots with strong in-plane optical anisotropy. *Physical Review B*, 72(16):161312, 2005.

[50] Marie Billard. *Practical and efficient solid-state sources of single and indistinguishable photons for quantum applications.* PhD thesis, 2021. Thèse de doctorat, Physique université Paris-Saclay 2021.

[51] B. Eble. *Interaction hyperfine dans les boîtes quantiques InGaAs sous pompage optique orienté.* Université Pierre et Marie Curie, Paris VI: PhD Thesis, 2007.

[52] J. J. Finley, P. W. Fry, A. D. Ashmore, A. Lemaître, A. I. Tartakovskii, R. Oulton, D. J. Mowbray, M. S. Skolnick, M. Hopkinson, P. D. Buckle, and P. A. Maksym. Observation of multicharged excitons and biexcitons in a single InGaAs quantum dot. *Physical Review B*, 63(16):161305, 2001.

[53] S. Laurent, B. Eble, O. Krebs, A. Lemaître, B. Urbaszek, X. Marie, T. Amand, and P. Voisin. Electrical control of hole spin relaxation in charge tunable InAs/GaAs quantum dots. *Physical review letters*, 94(14):147401, 2005.

[54] M. Kroutvar, Y. Ducommun, J. J. Finley, M. Bichler, G. Abstreiter, and A. Zrenner. Wavelength selective charge storage in self-assembled InGaAs/GaAs quantum dots. *Applied physics letters*, 83(3):443–445, 2003.

[55] B. Eble, O. Krebs, A. Lemaître, K. Kowalik, A. Kudelski, P. Voisin, B. Urbaszek, X. Marie, and T. Amand. Dynamic nuclear polarization of a single charge-tunable InAs/GaAs quantum dot. *Physical Review B*, 74(8):081306, 2006.

[56] O. Krebs. *Physique du spin dans les boîtes quantiques InGaAs/GaAs: Investigations optiques et modélisations.* Université Pierre et Marie Curie, Paris VI: HDR, 2012.

[57] O. Gywat, H. J. Krenner, and J. Berezovsky. *Spins in optically active quantum dots: concepts and methods*, page 52. John Wiley & Sons, 2009.

[58] M.I. Dyakonov and V.I. Perel. *Modern Problems in Condensed Matter Sciences*, chapter Theory of Optical Spin Orientation of Electrons and Nuclei in Semiconductors. North Holland Amsterdam, 1984.

[59] R. Winkler, S. Papadakis, E. De Poortere, and M. Shayegan. *Spin-Orbit Coupling in Two-Dimensional Electron and Hole Systems*, volume 41. Springer, 2003.

[60] G. Bastard. Wave mechanics applied to semiconductor heterostructures. 1990.

[61] J. Y. Marzin and J. M. Gerard. Optical properties of some III-V strained-layer superlattices. *Superlattices and Microstructures*, 5(1):51–58, 1989.

[62] E. L. Ivchenko. *Optical spectroscopy of semiconductor nanostructures.* Alpha Science Int'l Ltd., 2005.

[63] J. K. Furdyna. Diluted magnetic semiconductors. *Journal of Applied Physics*, 64(4):R29–R64, 1988.

[64] A. V. Komarov, S. M. Ryabchenko, O. V. Terletski, I. I. Zheru, and R. D. Ivanchuk. Magneto-optical investigations of the exciton band in CdTe: Mn^{2+}. *Soviet Journal of Experimental and Theoretical Physics*, 46:318, 1977.

[65] X. Liu and J. K. Furdyna. Ferromagnetic resonance in $Ga_{1-x}Mn_xAs$ dilute magnetic semiconductors. *Journal of Physics: Condensed Matter*, 18(13):R245, 2006.

[66] A. A. Maksimov, G. Bacher, A. McDonald, V. D. Kulakovskii, A. Forchel, C. R. Becker, G. Landwehr, and L. W. Molenkamp. Magnetic polarons in a single diluted magnetic semiconductor quantum dot. *Physical Review B*, 62(12):R7767, 2000.

[67] A. Gruber, A. Drabenstedt, C. Tietz, L. Fleury, J. Wrachtrup, and C. von Borczyskowski. Scanning confocal optical microscopy and magnetic resonance on single defect centers. *Science*, 276(5321):2012–2014, 1997.

[68] L. Besombes, Y. Léger, L. Maingault, D. Ferrand, H. Mariette, and J. Cibert. Carrier-induced spin splitting of an individual magnetic atom embedded in a quantum dot. *Physical Review B*, 71(16):161307, 2005.

[69] J. Schneider, U. Kaufmann, W. Wilkening, M. Baeumler, and F. Köhl. Electronic structure of the neutral manganese acceptor in gallium arsenide. *Physical Review Letters*, 59(2):240, 1987.

[70] A. K. Bhattacharjee and C. B. à la Guillaume. Model for the Mn acceptor in GaAs. *Solid state communications*, 113(1):17–21, 1999.

[71] S. Chutia and A. K. Bhattacharjee. Electronic structure of Mn-doped III-V semiconductor quantum dots. *Physical Review B*, 78(19):195311, 2008.

[72] A. O. Govorov. Optical probing of the spin state of a single magnetic impurity in a self-assembled quantum dot. *Physical Review B*, 70(3):035321, 2004.

[73] A. M. Yakunin, A. Y. Silov, P. M. Koenraad, J. M. Tang, M. E. Flatté, J. L. Primus, W. Van Roy, J. De Boeck, A. M. Monakhov, K. S. Romanov, et al. Warping a single Mn acceptor wavefunction by straining the GaAs host. *Nature materials*, 6(7):512–515, 2007.

[74] M. Goryca, P. Plochocka, T. Kazimierczuk, P. Wojnar, G. Karczewski, J. A. Gaj, M. Potemski, and P. Kossacki. Brightening of dark excitons in a single CdTe quantum dot containing a single Mn^{2+} ion. *Physical Review B*, 82(16):165323, 2010.

[75] A. K. Bhattacharjee. Exciton fine structure and coherent spin precession in transition-metal-doped semiconductor quantum dots. *Physical Review B*, 76(7):075305, 2007.

[76] Arian Vezvaee, Paul Hilaire, Matthew F Doty, and Sophia E Economou. Deterministic generation of entangled photonic cluster states from quantum dot molecules. *Physical Review Applied*, 18(6):L061003, 2022.

[77] A. V. Kuhlmann, J. Houel, A. Ludwig, L. Greuter, D. Reuter, A. D. Wieck, M. Poggio, and R. J. Warburton. Charge noise and spin noise in a semiconductor quantum device. *Nature Physics*, 9(9):570–575, 2013.

[78] B. Alén, F. Bickel, K. Karrai, R. J. Warburton, and P. M. Petroff. Stark-shift modulation absorption spectroscopy of single quantum dots. *Applied Physics Letters*, 83(11):2235–2237, 2003.

[79] A. N. Vamivakas, Y. Zhao, C. Y. Lu, and M. Atatüre. Spin-resolved quantum-dot resonance fluorescence. *Nature Physics*, 5(3):198–202, 2009.

[80] A. N. Vamivakas, C. Y. Lu, C. Matthiesen, Y. Zhao, S. Fält, A. Badolato, and M. Atatüre. Observation of spin-dependent quantum jumps via quantum dot resonance fluorescence. *Nature*, 467(7313):297–300, 2010.

[81] W. B. Gao, P. Fallahi, E. Togan, J. Miguel-Sánchez, and A. Imamoglu. Observation of entanglement between a quantum dot spin and a single photon. *Nature*, 491(7424):426–430, 2012.

[82] T. Kaldewey, A. V. Kuhlmann, S. R. Valentin, A. Ludwig, A. D. Wieck, and R. J. Warburton. Far-field nanoscopy on a semiconductor quantum dot via a rapid-adiabatic-passage-based switch. *Nature Photonics*, 12(2):68–72, 2018.

[83] L. Novotny, R. D. Grober, and K. Karrai. Reflected image of a strongly focused spot. *Optics letters*, 26(11):789–791, 2001.

[84] P. C. D. Hobbs. *Building electro-optical systems: making it all work*. John Wiley & Sons, 2022.

[85] M. Benelajla, E. Kammann, B. Urbaszek, and K. Karrai. Physical origins of extreme cross-polarization extinction in confocal microscopy. *Physical Review X*, 11(2):021007, 2021.

[86] P. M. Vora, A. S. Bracker, S. G. Carter, T. M. Sweeney, M. Kim, C. S. Kim, L. Yang, P. G. Brereton, S. E. Economou, and D. Gammon. Spin-cavity interactions between a quantum dot molecule and a photonic crystal cavity. *Nature communications*, 6(1):7665, 2015.

[87] H. Kamada, H. Gotoh, J. Temmyo, T.e Takagahara, and H. Ando. Exciton Rabi oscillation in a single quantum dot. *Physical Review Letters*, 87(24):246401, 2001.

[88] L. Allen and J. H. Eberly. *Optical resonance and two-level atoms*, volume 28. Courier Corporation, 1987.

[89] L. Besombes, Y. Léger, J. Bernos, H. Boukari, H. Mariette, J. P. Poizat, T. Clément, J. Fernández-Rossier, and R. Aguado. Optical probing of spin fluctuations of a single paramagnetic Mn atom in a semiconductor quantum dot. *Physical Review B*, 78(12):125324, 2008.

[90] L. Thevenard, L. Largeau, O. Mauguin, A. Lemaître, and B. Theys. Tuning the ferromagnetic properties of hydrogenated GaMnAs. *Applied Physics Letters*, 87(18), 2005.

[91] L. Thevenard, L. Largeau, O. Mauguin, A. Lemaître, K. Khazen, and H. J. Von Bardeleben. Evolution of the magnetic anisotropy with carrier density in hydrogenated $\mathrm{Ga}_{1-x}\mathrm{Mn}_x\mathrm{As}$. *Physical Review B*, 75(19):195218, 2007.

[92] A. O. Govorov. Optical and electronic properties of quantum dots with magnetic impurities. *Comptes Rendus Physique*, 9(8):857–873, 2008.

[93] L. Besombes, Y. Léger, L. Maingault, and H. Mariette. Spin properties of charged Mn-doped quantum dot. *Journal of applied physics*, 101(8), 2007.

[94] B. Varghese, H. Boukari, and L. Besombes. Dynamics of a Mn spin coupled to a single hole confined in a quantum dot. *Physical Review B*, 90(11):115307, 2014.

[95] A. Lafuente-Sampietro, H. Boukari, and L. Besombes. Resonant photoluminescence and dynamics of a hybrid Mn hole spin in a positively charged magnetic quantum dot. *Physical Review B*, 95(24):245308, 2017.

[96] A. Lafuente-Sampietro, H. Boukari, and L. Besombes. Strain-induced coherent dynamics of coupled carriers and Mn spins in a quantum dot. *Physical Review B*, 92(8):081305, 2015.

[97] V. Tiwari, M. Arino, S. Gupta, M. Morita, T. Inoue, D. Caliste, P. Pochet, H. Boukari, S. Kuroda, and L. Besombes. A hole-Cr^+ nanomagnet in a semiconductor quantum dot. *Physical Review B*, 104(4):L041301, 2021.

[98] V. Tiwari, M. Morita, T. Inoue, S. Ando, S. Kuroda, H. Boukari, and L. Besombes. Spin dynamics of positively charged excitons in Cr^+-doped quantum dots probed by resonant photoluminescence. *Physical Review B*, 106(4):045308, 2022.

[99] P. Kacman. Spin interactions in diluted magnetic semiconductors and magnetic semiconductor structures. *Semiconductor Science and Technology*, 16(4):R25, 2001.

[100] S. H. Autler and C. H. Townes. Stark effect in rapidly varying fields. *Physical Review*, 100(2):703, 1955.

[101] X. Xu, B. Sun, P. R. Berman, D. G. Steel, A. S. Bracker, D. Gammon, and L. J. Sham. Coherent optical spectroscopy of a strongly driven quantum dot. *Science*, 317(5840):929–932, 2007.

[102] G. Jundt, L. Robledo, A. Högele, S. Fält, and A. Imamoğlu. Observation of dressed excitonic states in a single quantum dot. *Physical review letters*, 100(17):177401, 2008.

[103] X. Xu, B. Sun, E. D. Kim, K. Smirl, P. R. Berman, D. G. Steel, A. S. Bracker, D. Gammon, and L. J. Sham. Single charged quantum dot in a strong optical field: absorption, gain, and the ac-Stark effect. *Physical review letters*, 101(22):227401, 2008.

[104] M. Kroner, C. Lux, S. Seidl, A. W. Holleitner, K. Karrai, A. Badolato, P. M. Petroff, and R. J. Warburton. Rabi splitting and ac-Stark shift of a charged exciton. *Applied Physics Letters*, 92(3):031108, 2008.

[105] C. Cohen-Tannoudji, J. Dupont-Roc, and G. Grynberg. *Atom-photon interactions: basic processes and applications.* John Wiley & Sons, 1998.

[106] B. R. Mollow. Stimulated emission and absorption near resonance for driven systems. *Physical Review A*, 5(5):2217, 1972.

[107] E. B. Flagg, A. Muller, J. W. Robertson, S. Founta, D. G. Deppe, M. Xiao, W. Ma, G. J. Salamo, and C. K. Shih. Resonantly driven coherent oscillations in a solid-state quantum emitter. *Nature Physics*, 5(3):203–207, 2009.

[108] C. Spinnler, L. Zhai, G. N. Nguyen, J. Ritzmann, A. D. Wieck, A. Ludwig, A. Javadi, D. E. Reiter, P. Machnikowski, R. J. Warburton, et al. Optically driving the radiative Auger transition. *Nature communications*, 12(1):6575, 2021.

[109] P. Meystre and M. Sargent. *Elements of quantum optics.* Springer Science & Business Media, 2007.

[110] L. M. Narducci, M. O. Scully, G. L. Oppo, P. Ru, and J. R. Tredicce. Spontaneous emission and absorption properties of a driven three-level system. *Physical Review A*, 42(3):1630, 1990.

[111] M. O. Scully and M. S. Zubairy. *Quantum optics.* American Association of Physics Teachers, 1999.

[112] A. Lazoudis, T. Kirova, E. H. Ahmed, P. Qi, J. Huennekens, and A. M. Lyyra. Electromagnetically induced transparency in an open V-type molecular system. *Physical Review A*, 83(6):063419, 2011.

[113] S. A. Empedocles and M. G. Bawendi. Influence of spectral diffusion on the line shapes of single CdSe nanocrystallite quantum dots. *The Journal of Physical Chemistry B*, 103(11):1826–1830, 1999.

[114] A. Reigue, R. Hostein, and V. Voliotis. Resonance fluorescence of a single semiconductor quantum dot: The impact of a fluctuating electrostatic environment. *Semiconductor Science and Technology*, 34(11):113001, 2019.

[115] M. Kroutvar, Y. Ducommun, D. Heiss, M. Bichler, D. Schuh, G. Abstreiter, and J. J. Finley. Optically programmable electron spin memory using semiconductor quantum dots. *Nature*, 432(7013):81–84, 2004.

[116] L. Giner, L. Veissier, B. Sparkes, A. S. Sheremet, A. Nicolas, O. S. Mishina, M. Scherman, S. Burks, I. Shomroni, D. V. Kupriyanov, et al. Experimental investigation of the transition between Autler-Townes splitting and electromagnetically-induced-transparency models. *Physical Review A*, 87(1):013823, 2013.

Résumé substantiel en français

Au cours des deux dernières décennies, des recherches approfondies ont été consacrées à l'exploration des boîtes quantiques de semi-conducteurs dopées avec une seule impureté magnétique. Celle-ci leur confère un spin électronique localisé qui peut se coupler aux états électroniques des boîtes. La plupart de ces études était destinée à mieux comprendre l'interaction d'échange entre le spin magnétique et le spin des charges (électron ou trou) confinées au sein d'une boîte quantique. Mais au-delà de cette exploration assez académique, il existe un intérêt croissant pour utiliser un tel système de spin localisé comme possible bit quantique (ou qubit) d'information à l'état solide, pour des applications telles que des mémoires quantiques couplées aux qubits volants que peuvent être les photons. Une telle possibilité est particulièrement attrayante dans le cas des boîtes quantiques III-V en micro-cavité optique, qui constituent actuellement les sources les plus avancées de photons uniques indiscernables et potentiellement de "clusters" de photons multi-intriqués.

En particulier, le protocole Lindner-Rudolph qui a récemment été mis en œuvre avec succès pour la génération de ces états clusters (toutefois avec seulement quelques photons) fait face aux imperfections de l'interface spin-photon des boîtes quantiques non dopées. Une nouvelle voie d'exploration est souhaitable et pourrait émerger avec l'utilisation des boîtes quantiques InGaAs/GaAs dopées avec un seul atome de Manganèse. Sous certaines conditions, elles présentent des règles de sélection optique compatibles avec un protocole proposé pour la génération d'états clusters à partir d'une molécule artificielle formée de deux boîtes quantiques, à savoir des transitions en Λ pour la manipulation du spin et des transitions cycliques pour l'émission de photons.

Dans cette perspective, le travail présenté dans ce manuscrit franchit une étape préliminaire en effectuant la spectroscopie cohérente avec un laser continue de certains états excités de boîtes quantiques dopées. Cette approche est appliquée à une boîte quantique InGaAs/GaAs dopée avec un seul atome de Manganèse (Mn), dans le but spécifique d'évaluer la cohérence entre différents états de spin associés à ce dopant magnétique.

Jusque-là, les boîtes quantiques InGaAs dopées au Mn dans un état de charge bien défini n'avaient été étudiées que sous excitation non résonnante par micro-photoluminescence (µ-PL). Pour exciter ces boîtes quantiques de manière résonante, nous avons d'abord mis au point un microscope confocal à champ sombre basé sur le rejet du laser résonant réfléchi dans une configuration à polarisation croisée. Bien que nous ayons obtenu une extinction proche de l'état de l'art, la réalisation d'une véritable expérience de fluorescence par résonance s'est avérée difficile. En raison de diffusion spectrale élevée dans notre échantillon, le signal PL s'est avéré bien trop faible par rapport bruit de grenaille du laser réfléchi. Pour contourner ce problème, nous avons

mis en œuvre une expérience de diffusion Raman résonante basée sur des transitions spécifiques de type Λ, ce qui nous a permis d'enregistrer le signal PL à une longueur d'onde différente de celle du laser résonnant, tout en donnant accès à l'étude de la cohérence des états de spin excités.

Nous avons d'abord appliqué cette technique pour étudier le cas d'un dopant Mn passivé par un atome d'hydrogène H. Dans les matériaux III-V, le Mn agit comme un accepteur peu profond. La passivation à l'hydrogène vise à empêcher la formation de cet état accepteur en liant l'un des atomes d'As voisins du Mn à un atome d'H. La signature optique résultante observée dans le spectre PL standard a révélé des motifs complexes notamment en champ magnétique. Pour interpréter ces résultats, nous avons développé un modèle théorique traitant le dopant Mn compensé comme un système de spin 5/2 sous forte contrainte uni-axiale, donnant lieu à une structure de niveaux qui a pu être confirmée par nos mesures de spectroscopie résonante. Incidemment, l'accord de notre modèle avec les résultats expérimentaux a nécessité de considérer une interaction d'échange ferromagnétique trou-Mn, contrairement à l'échange anti-ferromagnétique typique dans les boîtes quantiques II-VI et III-V.

Nous nous sommes ensuite concentrés sur la spectroscopie de cohérence de boîtes quantiques InGaAs dopées avec un Mn non passivé, afin d'étudier la cohérence entre différents états de spin. Nous avons d'abord utilisé un seul laser accordable pour scanner de manière résonnante les transitions d'un système en V, tout en mesurant la fluorescence due à la diffusion Raman résonnante vers un état spectateur. Les doublets d'Autler-Townes ont été résolues avec succès à puissance laser élevée, malgré l'élargissement inhomogène considérable des transitions optiques, ce qui a permis de mesurer les dipôles optiques. Pour décrire ce système, nous avons utilisé un modèle théorique basé sur les équations de Bloch optiques, qui a montré un excellent accord avec les résultats expérimentaux. Il nous a également permis d'estimer le temps de relaxation du spin entre les états fondamentaux ferromagnétique et antiferromagnétique.

Par la suite, nous avons réalisé une expérience à deux lasers, l'un fixé sur l'une des transitions du système V tandis que l'autre balaie la transition restante. L'utilisation de deux lasers a permis de créer une cohérence entre les états de spin excités, ce qui détermine le contraste du doublet Autler-Townes mesuré par cette méthode. En modélisant ces résultats, nous avons pu démontrer que le temps de cohérence du spin des états excités est principalement déterminé par leur durée de vie radiative.